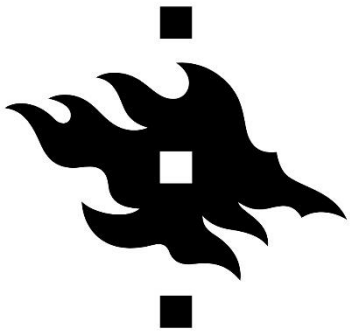

HELSINGIN YLIOPISTO
HELSINGFORS UNIVERSITET
UNIVERSITY OF HELSINKI

Conversion Reactions of Atomic Layer Deposited Thin Films

Paloma Ruiz

M.Sc. Thesis

University of Helsinki

Department of Chemistry

Inorganic Materials Chemistry

October 2020

Supervisors
Prof. Mikko Ritala
Dr. Jani Holopainen

Examiners
Prof. Mikko Ritala
Prof. Matti Putkonen

HELSINGIN YLIOPISTO
HELSINGFORS UNIVERSITET
UNIVERSITY OF HELSINKI
MATEMAATTIS-LUONNONTIETEELLINEN TIEDEKUNTA
MATEMATISK-NATURVETENSKAPLIGA FAKULTETEN
FACULTY OF SCIENCE

Tiedekunta – Fakultet – Faculty	Laitos – Institution – Department
Faculty of Science	Department of Chemistry

Opintosuunta – Studieinrikting – Study track

Inorganic Chemistry

Tekijä – Författare – Author

Paloma Ruiz

Työn nimi – Arbetets titel – Title

Conversion Reactions of Atomic Layer Deposited Thin Films

Työn laji – Arbetets art – Level	Aika – Datum – Month and year	Sivumäärä – Sidoantal – Number of pages
M.Sc. Thesis	10/2020	116

Tiivistelmä – Referat – Abstract

High-quality thin films deposited by Atomic layer deposition (ALD) are key components in numerous modern technological applications. The technique is extensively used in the semiconductor and photovoltaic industry, for example. ALD is an excellent technique for thin film deposition due to its characteristic self-limiting surface reactions that allow a reproducible, conformal, and precisely controlled coating on a substrate. Numerous new ALD materials are developed each year to advance technological innovations to new levels. However, occasionally a desired material cannot be produced directly by ALD. To still obtain the impressive features of ALD, an ALD thin film can be transformed chemically or physically in a manner that preserves the film-like structure of the original layer. This thesis explores these types of ALD film transformations, or conversions, by attempting the conversions of atomic layer deposited Al_2O_3 from a two-dimensional film to a tree-dimensional film structure, Ru to RuO_2, Re to ReO_3, ZnO to ZIF-8, and ZrO_x to UiO-66 films.

Current preparation methods, common applications, and general properties of these five materials are explored in the literature review. This provides an insight on some of the key features of the fabrication of these materials and what value the thin film structure brings them. It also highlights the challenges that are encountered regarding these processes. If the material has been obtained through conversion of an ALD thin film, the process is reviewed with detail. Additionally, the literature review explains the basics of conversion reactions as well as fundamentals of ALD.

The experimental section focuses on studying and optimizing the distinct challenges as well as explores new methods for fabricating the materials through the conversion of ALD thin films. Conversion of zirconium oxide thin films to UiO-66 under terephthalic acid vapor was attempted with modest results. Ru thin films were converted into crystalline RuO_2 under ambient and O2 atmospheres successfully and the processes seem promising for further research. Re and ReN_x films were partially converted to ReO_3 under O_2, O_3 and humid environments. The continuity of these films proved to be problematic. Factors affecting the formation of ZIF-8 and Al_2O_3 “grass" in the conversions of ZnO under 2-methylimidazole vapor and Al_2O_3 under heated water, respectively, were assessed, and the optimization of these processes was studied.

Avainsanat – Nyckelord – Keywords

Conversion reaction, Atomic Layer Deposition, ALD, Noble metal oxide, Metal-organic framework, Aluminum oxide

Säilytyspaikka – Förvaringställe – Where deposited

Kumpula Campus Library / E-thesis

Muita tietoja – Övriga uppgifter – Additional information

Table of Contents

Abbreviations

AFM	atomic force microscopy
ALD	atomic layer deposition
ALE	atomic layer etching
A-ZnO	a ZnO thin film with an Al_2O_3 thin film underneath
BDC	1,4-benzenedicarboxylic acid
CVD	chemical vapor deposition
DEZ	diethyl zinc
DIW	deionized water
DMF	dimethylformamide
DRAM	dynamic random access memory
EBBDRu	(ethylbenzene)(1,3-butadiene)ruthenium(0)
EBCHDRu	(ethylbenzyl)(1,3-cyclohexadienyl)ruthenium(0)
EDS	energy dispersive X-ray spectroscopy
FA	fluid assisted
FTIR	fourier-transform infrared
FTO	fluorine-doped tin oxide
GPC	growth per cycle
(HD)^{i}PrMePhRu	(1,5-hexadiene)(1-isopropyl-4-methylbenzene)ruthenium(0)
MBE	molecular beam epitaxy
McOH	methacrylic acid
(MeCp)Ru(Py)	(methylcyclopentadienyl)(pyrrolyl)Ruthenium(II)
MEMS	micro-electro-mechanical systems
mIM	2-methylimidazolate
ML	monolayer
MLD	molecular layer deposition
MOCVD	metal organic chemical vapor deposition
MOF	metal-organic framework

NL	nanolaminate
OMS	open metal sites
PEALD	plasma enhanced atomic layer deposition
PLE	pulsed laser evaporation
P-MOF	polycrystalline metal-organic framework
PVD	physical vapor deposition
$RuCp_2$	bis(cyclopentadienyl)ruthenium(II)
$Ru(DMBD)(CO)_3$	η^4-2,3-dimethylbutadiene tricarbonyl ruthenium(0)
$Ru(DMPD)_2$	bis(2,4-dimethylpentadienyl)ruthenium(II)
$Ru(EtCp)_2$	bis(ethylcyclopentadienyl)ruthenium(II)
$Ru(MeMe_2CHD)_2$	bis(2,6,6-trimethyl-cyclohexadienyl)ruthenium(II)
$Ru(thd)_2(cod)$	bis(2,2,6,6-tetramethyl-3,5-heptanedionato)(1,5-cyclooctadiene)ruthenium(II)
SEM	scanning electron microscopy
SFM	scanning force microscopy
SURMOF	nearly perfectly oriented surface metal-organic framework thin films
T-ALD	thermal ALD
TEM	transmission electron microscopy
TMA	trimethylaluminum
T-ZnO	a ZnO thin film with a TiO_2 thin film underneath
UiO-66	Universitetet I Oslo 66
XRD	X-ray diffraction
XRR	X-ray reflection
ZIF-8	zeolite imidazole framework 8
$Zr(Cp)(^tB\ uDAD)(O^iPr)$	cyclopentadienylN,N-bis(tertbutyl)ethene-1,2-diaminato Isopropylalkoxozirconium
Zr(MeCp)(TMEA)	methylcyclopentanyl tris[2(methylamino)ethyl]aminate zirconium
$Zr(Me_5Cp)(TEA)$	pentamethylcyclopentadienyl triethanolaminate zirconium

1 Introduction

Atomic layer deposition (ALD) is a Chemical Vapor Deposition (CVD)-based technique for high-quality thin film deposition. CVD is a method in which gaseous precursors are simultaneously fed into a reaction chamber. Typically, heat or plasma is utilized to activate a chemical reaction on a substrate surface, and a thin film is deposited.[1] In ALD, precursors are alternately pulsed on a substrate surface. In between the pulses, the precursor gases are purged away with an inert gas.[2] This way the precursors are chemisorbed on the substrate surface and react with the second precursor on that surface, enabling saturative steps. This means that the same amount of film is deposited on the substrate during each pulse. When the steps are saturated, the growth mechanism becomes self-limiting and film thickness can be determined with the number of repetitions of the pulse-purge sequence.[3] The saturative nature of the technique also allows for exceptional conformality and uniformity over large areas. The main limitation of ALD is its low deposition rate, and batch processing is employed to ensure larger throughput.[4]

In addition to chemical processes, physical deposition processes can used as thin film deposition methods for some materials. In Physical Vapor Deposition (PVD), solid or liquid material is vaporized and transported through a low pressure environment onto the substrate, where it condenses. Examples of PVD are vacuum evaporation and sputtering, for example. These techniques, however, deposit material in a line-of-sight fashion, which leads to poor step coverage.

Conformality, pinhole-freeness and reproducibility are both key attributes of ALD and essential features for thin films for numerous applications. Unfortunately, ALD processes for certain materials could not have been developed. For example, the fabrication of smooth 2D thin films, metal-organic framework films, and some first-row transition metal films has been problematic. ALD thin films can, however, be converted, after their deposition. Upon conversion the state, appearance, or composition of an ALD film changes from the original material and structure. This can occur when a film is stored under ambient air and oxidises or when it encounters high temperatures and its crystallinity changes from amorphous to crystalline, for example. Conversion of ALD thin films is often perceived as a

undesired incident, and films are even developed to prevent other materials from converting.[5–7] On the contrary, conversion can also be a tool for modifying an existing film to a different, desired material, while keeping the superior features of an ALD thin film.

This thesis studies primarily chemical conversions of selected ALD thin film materials. Ruthenium, rhenium, aluminum oxide, zinc oxide, and zirconium oxide and their conversions are examined in the following sections. These materials are examples of a variety of conversion reactions and show great promise to benefit from them because they facilitate or even enable the materials to exist as thin films. For example, the deposition of RuO_2 by ALD is a very sensitive and slow process, and the control of parameters to obtain this film is extremely challenging. ReO_3 has not been obtained by ALD. Alumina grass is a self-standing, three-dimensional structure that cannot be achieved through ALD, but the features of which can be controlled by having a precise Al_2O_3 film as initial material. Finally, ALD of metal-organic thin films such as UiO-66 or ZIF-8, has not been possible.

The literature review of this thesis describes the advantages of each selected material and why they would benefit from a thin film form produced through conversion. It also concentrates on the methods that have previously been utilized to fabricate these materials and enlightens some of the key factors enabling the syntheses. The experimental section of this thesis describes studies on conversions of ALD Ru to RuO_2, Re to ReO_3, ZrO_2 to UiO-66, ZnO to ZIF-8, and Al_2O_3 to a grass-like structure by simple reactions. Conversion would allow for these materials to have a thin film form with the benefits provided by ALD.

Literature review

2 Atomic layer deposition (ALD)

Chemical vapor deposition (CVD) is a technique in which gas-phase precursors react on a substrate surface to form a film. In CVD, gaseous precursors and reactants are fed into the reaction chamber simultaneously. Reactions need to be activated with additional energy, such as heat or plasma, and a thin film is deposited on the substrate. Because of the simultaneous introduction of precursors into the reaction chamber, the reactions can be controlled by precursor diffusion or reaction kinetics and precise film thickness control is not evident.[1]

Atomic layer deposition (ALD) is a CVD-based technique for depositing thin films of various materials. Contrary to CVD, the precursors are pulsed alternately into the reaction chamber. Thus, the method is based on sequential pulsing of precursor gases onto a substrate, followed by saturative surface reactions or chemisorption of the precursors. The distinctive feature of ALD is its self-limiting, irreversible surface reactions, which allow atomic level thickness control and excellent film uniformity and conformality even on large substrates with complex geometries.[8,9]

ALD was first introduced by Suntola in the 1970s as atomic layer epitaxy.[10] It was originally used as a tool for manufacturing ZnS electroluminescent flat-panel displays, and the first ones operated in Helsinki-Vantaa airport from 1983 to 1998.[11] ALD research in the late 1980s focused mainly on fabrication of III-V compounds but no significant breakthroughs were made to surpass competing film deposition techniques. Silicon-based microelectronics re-sparked interest in ALD in the late 1990s, for the method seemed suitable for precise miniaturization of devices and creating new thin film materials.[12] Today, ALD has been a vital tool in the semiconductor industry with numerous applications, such as high-k dielectrics[13–15] and Cu metallization in interconnect technology[16,17]. It has also played an important role in the photovoltaic industry[18–20], biomedical industry[21–23], manufacturing of micro-electro-mechanical systems[4], and protective coatings[24,25].

A typical ALD process consists of four steps (Figure 1). First, a typically metal-containing precursor is introduced into the reaction chamber under vacuum. With a sufficient dose and pulse time, the precursor reacts with all available active surface sites and forms a layer of material on the substrate. Next, the excess precursor and reaction byproducts are purged from the reaction chamber with an inert gas or simply pumped away to ensure that reactions happen only at the substrate surface. After this, a second, typically nonmetal, precursor is introduced to the reaction chamber and reacts with the first layer of material. Again the excess precursor and reaction byproducts are purged from the reaction chamber, ideally leaving a monolayer (ML) of the desired material on the substrate. Theoretically film growth occurs one layer at a time. In practice, the growth per cycle (GPC) is about 0.5ML or less, due to steric hindrances and a limited amount of reactive surface sites. The thickness of the film can be controlled simply by repeating a cycle consisting of these four steps a selected number of times, forming the film in a layer-by-layer manner. Binary reaction sequences are the most representative ALD processes, though more than two precursors and reactants may also be used.[1]

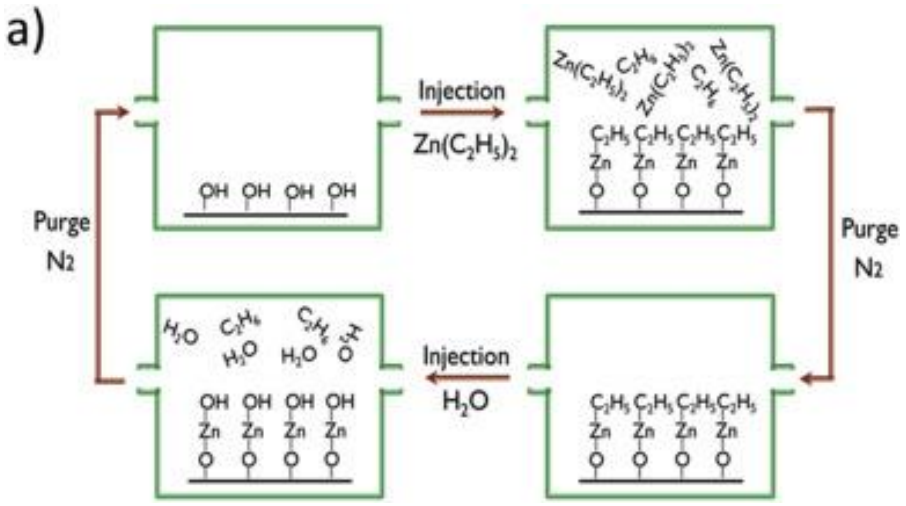

Figure 1. Typical ALD process steps. Reprinted from Ref. [1] with permission from Elsevier.

Deposition rates in ALD are about 100 nm/h even in good processes, which leads to long process times and sets limits to industrial applications.[4] Since slowness is the main drawback of ALD, methods to shorten process times have been studied and batch ALD, spatial ALD, and process engineering have been the three key solutions to the problem. Optimization of the tool flow dynamics and the increase of batch sizes can lead to a manyfold increase in deposition rates.[1,8]

In addition to an efficient reactor, proper precursors need to be chosen in order to create a good ALD process. The crucial requirements for ALD precursors include sufficient volatility, thermal stability, and high reactivity: the Gibbs free energy for the reaction should be as negative as possible. Also the precursor and the reaction by-products should not etch the substrate or the growing film. The precursor may be a liquid, gas or solid. Additional aspects to consider when choosing a precursor are its safety, sustainability and economical requirements.[14]

Surface reactions in ALD are typically driven by thermal energy, and process temperatures are usually about 150–350 °C. This type of ALD is considered as thermal ALD (T-ALD). The second, typically nonmetal, precursor can also be an organic linker or be added to a molecular fragment into the film. This grows the film in a molecular layer-by-layer manner, and is fittingly called molecular layer deposition.[26,27] Organic polymers and, when combined with ALD, inorganic-organic hybrid materials can be fabricated with this technique. Reactions can also be driven by other energy sources such as plasma, UV radiation or visible light. In plasma enhanced ALD (PEALD), the nonmetal precursor is activated with a plasma discharge in the third step of the ALD cycle (Figure 1), which supplies the additional energy required for an ALD process. PEALD is used in cases where a higher reactivity as compared to T-ALD is needed. The high reactivity of plasma species may result in improved material properties, lower deposition temperatures, and an increase in choices of precursor compounds. However, the aggressive nature of the plasma species may also lead to reduced conformality and film damage.[28]

3 Conversion Reactions

A chemical conversion is a process where a chemical transformation takes place, namely, the product composition differs chemically from the starting material and atoms rearrange.[29] For example, the rusting of iron can be considered as a chemical conversion. Changes that alter only state or appearance are physical changes; atoms or molecules do not change their identity. For example, the phase change of solid TiO_2 from anatase to rutile is a physical change. Conversion of thin films in the context of this thesis is defined as the chemical or physical transformation of a thin film in a manner that preserves the film-like structure of the original layer. This thesis will primarily focus on chemical conversions of ALD thin films.

Conventionally, thin films undergoing conversions are considered as problematic and unwanted. Once deposited, it is important for an ALD thin film to remain stable during its intended use, whether that is under harsh temperatures on spacecrafts or plain ambient conditions. Sometimes, however, the desired film material is obtained through converting existing ALD thin films. Conversion of thin films can take place via solid state reactions[30], vapor-solid reactions[31–34] and liquid-solid reactions[35], and can even be induced through irradiation[31]. Conversion may be the only route to new materials with the benefits of ALD thin films, or it can be a means of producing them in a more efficient manner.

For example, first-row transition metal thin films can be produced by conversion of ALD films. Metals such as Co[36], Ni[32,37], and Cu[38–40] are often deposited as nitrides or oxides rather than the elemental metals due to the low reactivity of the precursors in these processes. The oxide and nitride films are then converted to their metallic form for example by annealing at a high temperature or reducing with H_2 or NH_3 at a lower temperature. Film preparation through conversion can also improve film morphology. For instance, Cu films fabricated through the reduction of Cu_3N have a lower surface roughness compared to those deposited directly with ALD.[40] In addition to being an easier way to produce these films, this method offers higher growth rates and may allow deposition on a broader selection of materials.[41]

Post-deposition treatments of ALD thin films have also enabled crystallization of amorphous thin film materials. For example, growth of crystalline Metal-organic framework (MOF) thin films such as ZIF-8[42] or UiO-66[43] has not been successful directly by ALD, but the facile conversion of ALD films through vapor-solid reactions has enabled solvent-free synthesis of crystalline MOF thin films. This will be discussed in more detail in section 4.3. Furthermore, the fabrication of smooth 2D ALD thin films, such as as WS_2[44] and SnS_2[45] may need post-deposition annealing of the corresponding amorphous films to yield crystalline films (Figure 2). This has allowed the creation of smooth 2D films through scalable processes with thickness control down to monolayers.

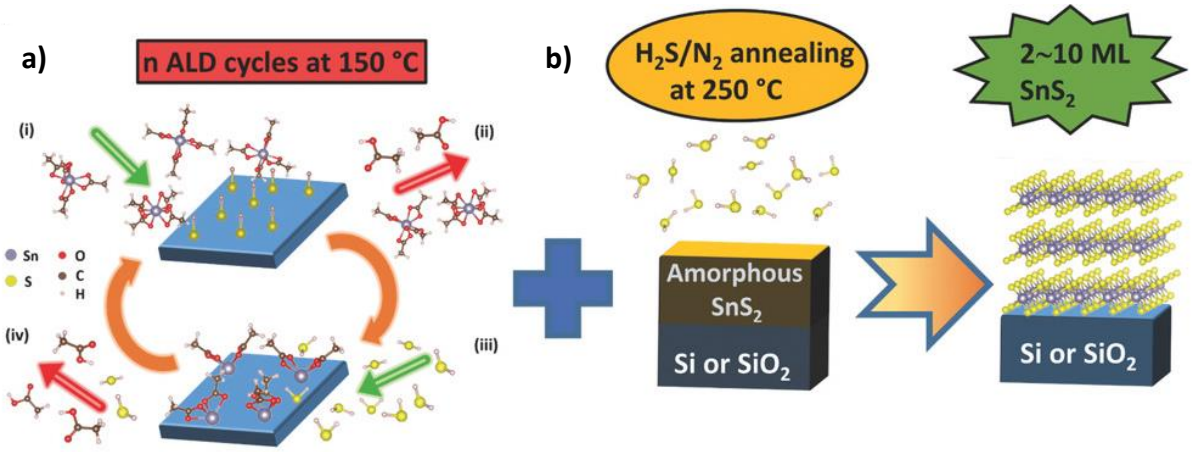

Figure 2. Representation of an ALD process for crystalline SnS_2 films: (a) deposition of amorphous SnS_2 through ALD followed by (b) a post-deposition conversion to crystalline SnS_2. Reprinted from Ref. [45] with permission from American Vacuum Society.

In addition to the fabrication of thin films of new materials, conversion can enable etching of film materials that are not otherwise readily removed, through a conversion-etch process. Atomic layer etching (ALE) can be considered as a reverse process for ALD. Both plasma and thermal ALE methods have been developed, and they offer both isotropic and anisotropic etching. Initial ALE methods are based on either fluorination and ligand-exchange reactions (thermal ALE)[46] or surface activation by halogenation followed by ion bombardment (plasma ALE)[47] to remove the surface layer. However, materials with volatile metal fluorides cannot be etched in a layerwise manner using these thermal ALE methods and some materials, such as elemental metals, may fluorinate readily, forming fluoride

layers that are too thick for ALE. In the conversion-etch process, the surface layer of a film is converted to a different material capable of being fluorinated and removed by ligand-exchange. It has been used for the ALE of WO_3[48], W[48], SiO_2[49], and ZnO[50] thin films, for example. This method is also promising for enabling the ALE of materials with volatile fluorides as etch products.[48]

While conversion is an excellent route to new thin film materials and enhanced film properties, it can have similar or even additional drawbacks to conventional ALD. Common conversion problems include long reaction times[43,51], industrial incompatibility[41], and incomplete transformations[52]. Even so, conversion of ALD thin films is a promising bridge between ALD and intricate thin film materials.

4 Materials Selected as Targets for Conversion Reactions

4.1 Noble metals

Noble metals are metallic elements that resist chemical action, do not corrode, and are not readily attacked by acids. They have remarkable resistance to oxidation even at high temperatures, are good conductors and have high catalytic activity. Noble metals are used frequently as catalysts to accelerate or control oxidation, reduction and hydrogenation reactions. The noble metal family is not strictly defined but typically includes ruthenium, osmium, rhodium, iridium, palladium, platinum, silver, and gold. In some classifications, rhenium is also considered as a noble metal because it shares some of the noble metal - like properties.[53,54]

Even though noble metals have outstanding resistance towards oxidation, they can be oxidized to form many different oxides with oxidation states ranging from +1 to +8. These oxides are quite unstable and tend to decompose quite readily upon heating. An interesting noble metal oxide is ReO_3, which has a lower resistivity than its metallic form and a metallic conductivity similar to the highly conductive Ag.[55] Some noble metal oxides with high oxidation states, such as RuO_4 and OsO_4, are volatile and dangerous.

Noble metal ALD processes commonly include the use of reducing agents, such as H_2 or formalin, or an oxidative agent, mainly O_2. These can also be combined so that first a noble metal oxide is grown with ozone, and H_2 is introduced between every growth cycle to reduce the oxide. T-ALD process temperatures for noble metal thin films typically range from 80 to 200 °C. Noble metal oxides typically need more careful growth parameters, and Rh_2O_3, IrO_2, PdO, RuO_2, and PtO_x have been grown with ozone through T-ALD. Reductive NH_3 and H_2 plasmas have usually been chosen for PEALD processes, and for example Ru, Ir, Pt, and Ag have been grown with this method. There are not many oxide PEALD processes for noble metal oxides but for example PtO_2 films have been grown with O_2 plasma.[56]

4.1.1 Ruthenium and Ruthenium Oxide

Ruthenium belongs to the platinum group of the periodic table. It has a low resistivity (~7 μΩ·cm for bulk), a high melting point (2333 °C), excellent chemical and thermal stability, and high work function (~4.7 eV).[57] Ruthenium is a desirable material for microelectronic applications not only for its physical properties but also for its low cost compared to most other noble metals.[58] Its high work function minimizes leakage current through a capacitor. Ruthenium thin films have been widely studied for microelectronic applications, such as metal gates in metal-oxide-semiconductor field-effect transistors[59,60], electrodes in metal-insulator-metal capacitors[61,62], and seed layers for Cu electroplating[63].[56,64]

Ruthenium has two oxides: RuO_2 and RuO_4. RuO_4 does not have thin film applications due to its low melting point of 25 °C and a boiling point of 40 °C. RuO_2, on the other hand, has a melting point of 1300 °C and, similarly to metallic Ru, a low resistivity (~46 μΩ·cm)[65], excellent thermal stability, and a high work function (~5.4 eV)[66]. These features make it a promising material for the electrodes in future dynamic random access memory (DRAM) devices.[66] Ruthenium(IV) oxide has been widely studied in recent years also due to its promising photocatalytic properties and photoelectrochemical performance.[67,68] For many of these applications, RuO_2 films need to be crystalline, smooth, and conformal even on three-dimensional structures, and as thin as possible to serve well in the ever-shrinking device dimensions. ALD is the most appropriate method for producing films with these requirements because of its unique features that produce films with accurate atomic scale control.

There are many ALD processes for Ru, and several of these consist of alternately pulsing a Ru-based metal-organic precursor and molecular O_2 into the reaction chamber.[65,69–78] ALD processes for RuO_2 film deposition consist mostly of these same precursors.[56] Selected RuO_2 ALD processes are reviewed in Table 1. Whether a Ru or RuO_2 thin film is deposited depends on the process parameters, such as precursor doses, oxygen partial pressure and deposition temperature. It has been shown that RuO_2 thin films are obtained with the same precursors as used in the Ru processes by lowering the deposition temperatures and lengthening the oxygen pulses.[65,70] The process optimization is, however, a very

complicated matter: RuO_2 film formation depends on the delicate balance of every single parameter involved. In addition to the delicacy of the process, the resulting film morphologies are often not optimal[79–81], and the oxygen pulses required can be long (~20 – 45 s) and flow rates high (180-500 sccm).[65,70,71] The use of ozone in these processes would be precarious since ozone etches Ru to form volatile RuO_4.[54]

Table 1. Precursors and reactants, deposition temperatures, resulting film thicknesses and resistivities, and publication years of selected T-ALD RuO_2 processes.

Precursor	Reactant	Deposition temp. (°C)	Film thickness (nm)	Resistivity (μΩ cm)	Year, reference
$Ru(EtCp)_2$	O_2	270			2004[82]
$Ru(EtCp)_2$	O_2	270	90	70	2007[83]
$Ru(EtCp)_2$ mod	O_2	265	40		2007[84]
$RuCp_2$	O_2	300	70	270	2008[85]
$Ru(EtCp)_2$	O_2	300			2009[86]
(MeCp)Ru(Py)	O_2		10		2009[61]
RuO_4 in organic solvent	H_2	230	7.2-21.6	250	2010[87]
$Ru(EtCp)_2$	O_2	280	30		2011[80]
$Ru(Me\text{-}Me_2\text{-}CHD)_2$	O_2				2011[88]
$Ru(DMPD)_2$	O_2	200			2012[89]
$(HD)^iPrMePhRu$	O_2	200	~30	270-290	2014[70]
EBCHDRu(0)	O_2	225	32	118	2014[79]
EBBDRu	O_2	225	5-35	140	2015[71]
$Ru(DMBD)(CO)_3$	O_2	240	10-40	62	2017[65]
$Ru(thd)_2$ (cod) in solvent	O_2	230-270	6-28		2019[81]

The poor morphology of RuO_2 thin films deposited *via* ALD and even MOCVD (metal organic chemical vapor deposition) can be seen for example from Brytavskyi's et al.[81] work. RuO_2 was deposited on porous silicon substrates using $Ru(thd)_2(cod)$ and O_2 as precursors *via* MOCVD and ALD. Deposition temperatures were 290 and 250 °C for MOCVD and ALD, respectively. The average size of macropores in the substrate was about 1-2 µm and the thickness of the porous layer roughly 21 µm. The ALD process consisted of 130 cycles and MOCVD of 150 injections. Transmission electron microscopy (TEM) and energy dispersive X-ray spectroscopy (EDS) showed that conformal coverage of the substrate surface was achieved with both deposition methods but MOCVD gave a non-uniform distribution of RuO_2 along the pores. Unfortunately, SEM images revealed granular morphologies with average grain sizes of 18 nm for the ALD samples and 25 nm for the MOCVD samples (Figure 3).

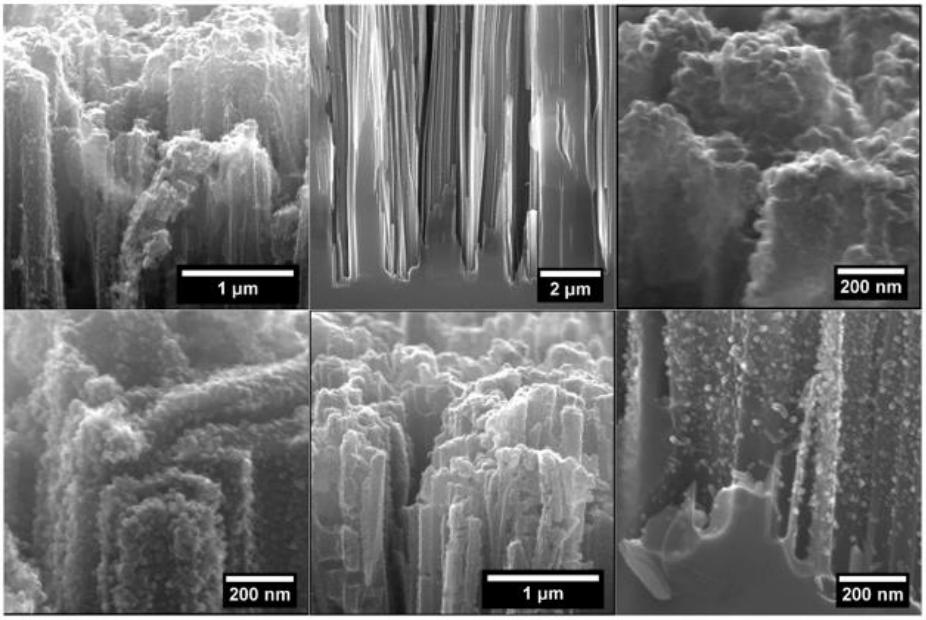

Figure 3. Cross-sectional SEM images of RuO_2 thin films deposited on a porous silicon substrates by MOCVD (top) and ALD (bottom). Reprinted from Ref. [81] with permission from Elsevier.

Commonly RuO_2 thin films have been deposited by ALD with precursors where ruthenium has a nonzero oxidation state, for example $Ru(EtCp)_2$[80,83,90] and (MeCp)Ru(Py)[61], together with O_2. These ALD RuO_2 processes have been found to have relatively long incubation periods: the initial growth rates are significantly lower than those after a few tens of

cycles.[61,80,90] This is due to a delayed nucleation of the film material, and leads to rough and discontinuous thin films. For example, Salaün et al.[80] reported island-like growth of an ALD-RuO_2 thin film even after 1200 cycles (Figure 4). The average thickness of the film was 30 nm and the process was conducted at 280 °C using $Ru(EtCp)_2$ and O_2 as precursors. Kim et al.[90] used the same precursors at 265 °C and the incubation period extrapolated from the film thicknesses to the number of ALD cycles was roughly 35 cycles.

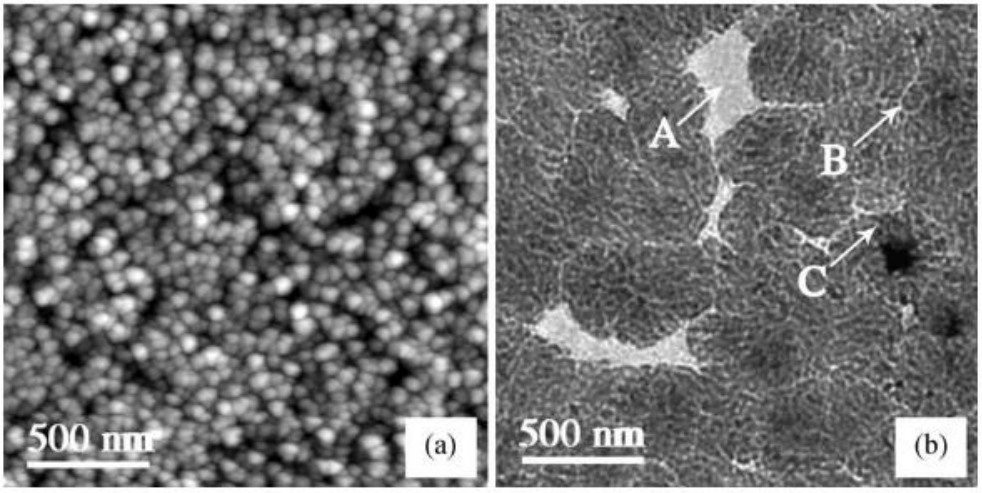

Figure 4. AFM (a) and TEM (b) images of the RuO_2 layer obtained by 1200 ALD cycles. Positions of no granular deposition (b,A), channels separating the RuO_2 islands (b,B), and micropores (b,C) are also depicted. Reprinted from Ref. [78] with permission from John Wiley and Sons.

It has been shown that the incubation period can be decreased by optimizing the Ru-precursor. Park et al.[79] showed that the nucleation period is reduced significantly when a zero metal valence Ru-precursor is used. The group deposited RuO_2 films on silica substrates at 225 °C using EBCHDRu ((ethylbenzyl)(1,3-cyclohexadienyl)ruthenium(0)) and O_2 as precursors. The growth rate was 1.9 Å/cycle, and the incubation time was determined to be only ~2 cycles. The number of ALD cycles was varied from 3 to 200, and a continuous RuO_2 thin film with a thickness of ~6.5 nm was achieved already after 40 deposition cycles. The roughness of a 32 nm film was determined to be 0.33 nm, while the roughness of Salaün's et al.[80] 30 nm RuO_2 film was approximately 5 nm. RuO_2 thin films were also

deposited successfully with a step coverage of ~100 % on trenches with a narrow top opening size of 25 nm and an aspect ratio of 4.5 (Figure 5).

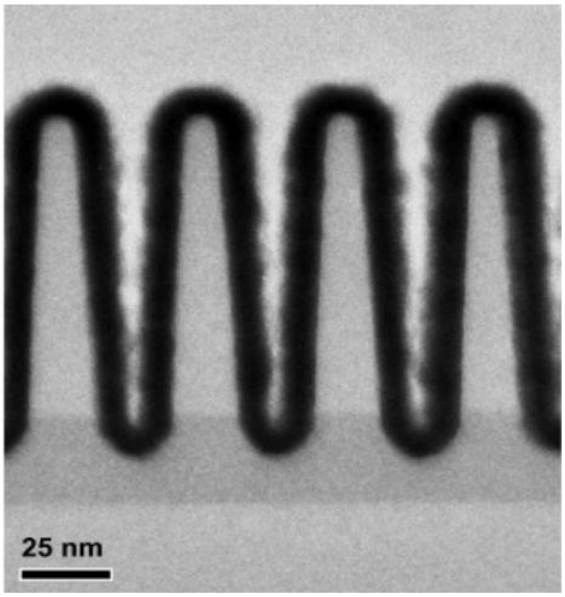

Figure 5. Cross-sectional TEM image showing the excellent step coverage of the RuO_2 ALD process using EBCHDRu and O_2 as precursors. Reprinted from Ref. [79] with permission from Elsevier.

Other attempts to decrease surface roughness include the use of PEALD, lengthening O_2 pulses, introduction of RuO_2 seeds, and use of different substrate materials. Kim et al.[91] showed a decrease in incubation cycles with the $Ru(EtCp)_2$-O_2 process from 45 to 13 cycles by changing the substrate from SiO_2 to Ta_2O_5. Sawada et al.[66] deposited 30 nm RuO_2 thin films by PEALD with $Ru(EtCp)_2$ and oxygen plasma on 10 nm Al_2O_3 and TiO_2 buffer layers as well as 100 nm thick SiO_2 films. The roughnesses of the films were 2.5 nm on SiO_2, 0.9 nm on Al_2O_3, and 0.7 nm on TiO_2. The lower roughnesses of the RuO_2 films grown on Al_2O_3 and TiO_2 were explained by a more uniform nucleation caused by the slightly charged surface layers of these substrates which in turn are caused by metal vacancies in these layers. When the substrate surface is charged (positively or negatively), the $Ru(EtCp)_2$ precursor is trapped on the surface for a longer time than on uncharged SiO_2, which promotes precursor decomposition. Surface roughness of the films grown on silica could be decreased from 2.5 to 1.4 nm by introducing sputtered 1 nm RuO_2 seeds on the substrate before PEALD.

Austin et al.[65] compared T-ALD and PEALD methods for RuO_2 film deposition using a zero-oxidation state ruthenium precursor, $Ru(DMBD)(CO)_3$, and oxygen or oxygen plasma as the reactant at 200-240 °C. The oxygen pulse lengths and flow rates for the T-ALD process and PEALD process were 20 s and 180 sccm, respectively. The films grown by PEALD had higher nucleation delays (76 cycles) and lower growth rates (0.29 Å/cycle) than those grown by T-ALD, which exhibited a nucleation delay of 35 cycles and a growth rate of 0.65 Å/cycle. The roughnesses determined with AFM for the 12 nm thick T-ALD and PEALD RuO_2 films were 0.6 and and 0.4 nm, respectively (Figure 6). Additionally, the films grown with T-ALD showed more distinct crystallinity (Figure 7) and lower resistivity (~62 μΩ cm) than the PEALD films (~377 μΩ cm). The inferior quality of the PEALD process is most likely due to the O_2 plasma reacting with the RuO_2 film to form volatile RuO_4 products and thus etching the film.[92]

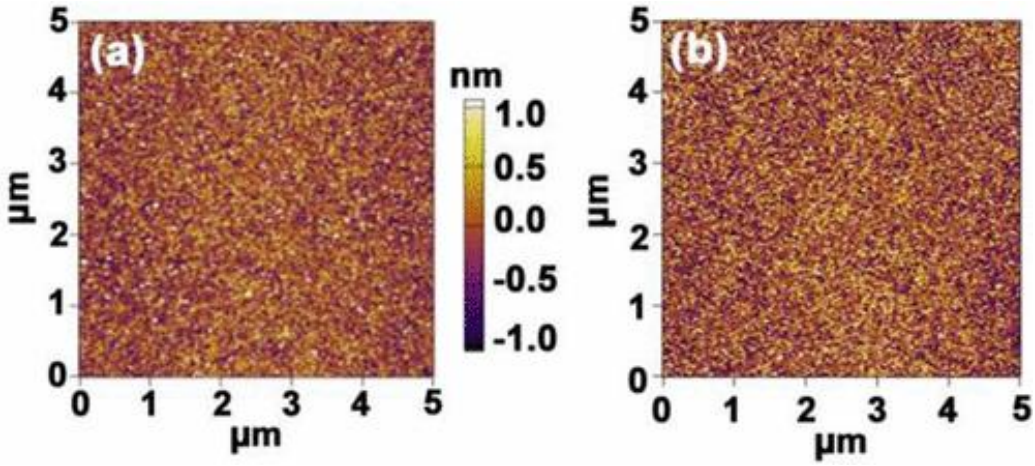

Figure 6. AFM images of 12 nm thick RuO_2 films deposited with (a) T-ALD at 240 °C and (b) PEALD at 230 °C. Reprinted from Ref. [65] with permission from American Chemical Society.

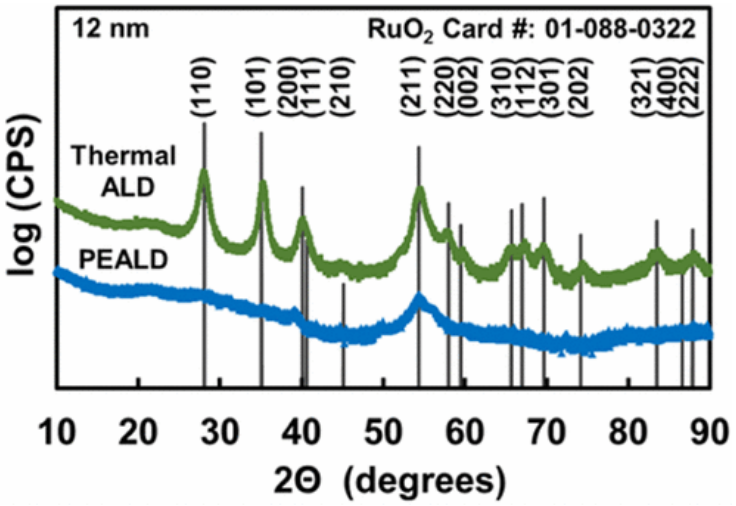

Figure 7. GIXRD diffractograms of for RuO2 thin films with a 12 nm thickness grown via T-ALD (green) and PEALD (blue) deposited at 240 and 230 °C, respectively. Reprinted from Ref. [65] with permission from American Chemical Society.

While using a zero-valent ruthenium precursor has helped in shortening the incubation period of RuO_2 ALD processes and thus improving the film morphology, Yeo et al.[71] have additionally used extremely long O_2 pulses to combat these issues. ALD RuO_2 thin films were deposited on SiO_2 with EBBDRu and O_2 at 225 °C. The O_2 pulse duration was 45 s with a flow rate of 200 sccm. Continuous films as thin as 5 nm were obtained with an incubation period of only 6 cycles and a growth rate of ~0.9 Å/cycle. TEM images (Figure 8) showed a continuous but slightly rough film.

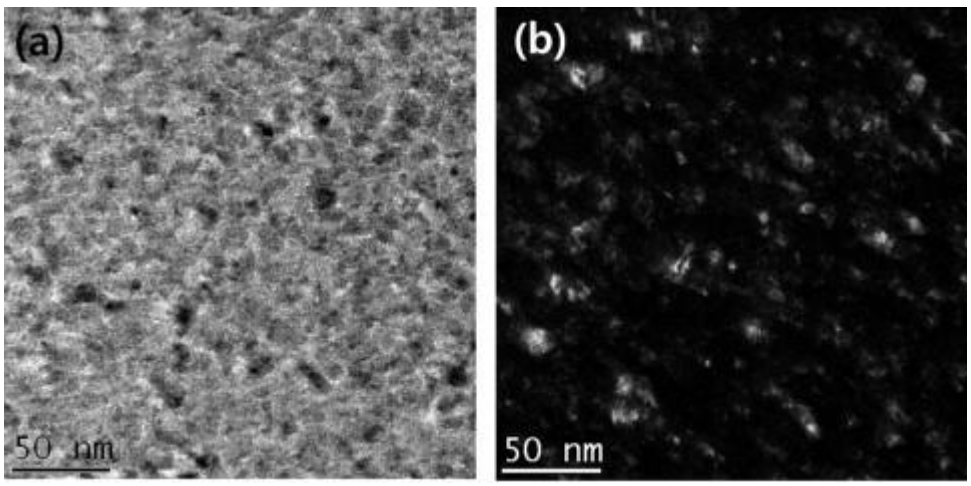

Figure 8. (a) Bright field and (b) dark-field plan-view TEM images of RuO_2 films grown by ALD with EBBDRu and O_2 as precursors. Reprinted from Ref. [71] with permission from Elsevier.

Conversion of Ru thin films into RuO_2 could be a solution to the difficulties of the conventional ALD processes. Yeo et al.[71] attempted this through conversion of Ru thin films. It was claimed that 20 nm ALD Ru film was successfully converted to RuO_2 by annealing under an O_2 atmosphere at 600 °C.

4.1.2 Rhenium and Rhenium Oxide

Rhenium has a work function of 4.7 eV, low resistivity (22 μΩ cm for a thin film), and is considered to be both a refractory and a noble metal.[93] Even though rhenium is a scarce material in the Earth's crust, it is widely used as a catalyst in the petroleum industry[94] and ammonia synthesis[95] as well as in Fischer-Tropsch synthesis[96] on a research scale. It is also used in microwave resonators[97] and is a promising material for superconducting quantum computing and quantum information applications.[93]

Rhenium films have previously been synthesized with molecular beam epitaxy (MBE)[97], CVD[98,99], pulsed laser evaporation (PLE)[100], electron-beam evaporation[99], electrodeposition[101], and sputtering[102]. There is only one published ALD process for Re thin films: a study by Hämäläinen et al.[93] employing $ReCl_5$ and NH_3 as precursors at 400 °C on silicon substrates covered by a 5-10 nm ALD Al_2O_3 film. Continuous films with thicknesses down to 3 nm were obtained and a total of 2 atom% N, H, Cl and C impurity content. The resistivity was about 90 μΩ cm for the 3 nm film and stabilized to about 22 μΩ cm for the thicker films. The thinner, 3-10 nm, films were observed to react under ambient conditions to form ReO_x, which can be verified from the FESEM images and GIXRD diffractograms (Figure 9). The thinner films were susceptible to ambient for a prolonged period of time. The FESEM images reveal large crystallites on the films even though the diffractograms show the films to be amorphous. It was proposed that the aging of the films in air lead to the formation of ReO_3. Rhenium nitride films grown with the same precursors between 275 and 375 °C did not exhibit this kind of behavior.

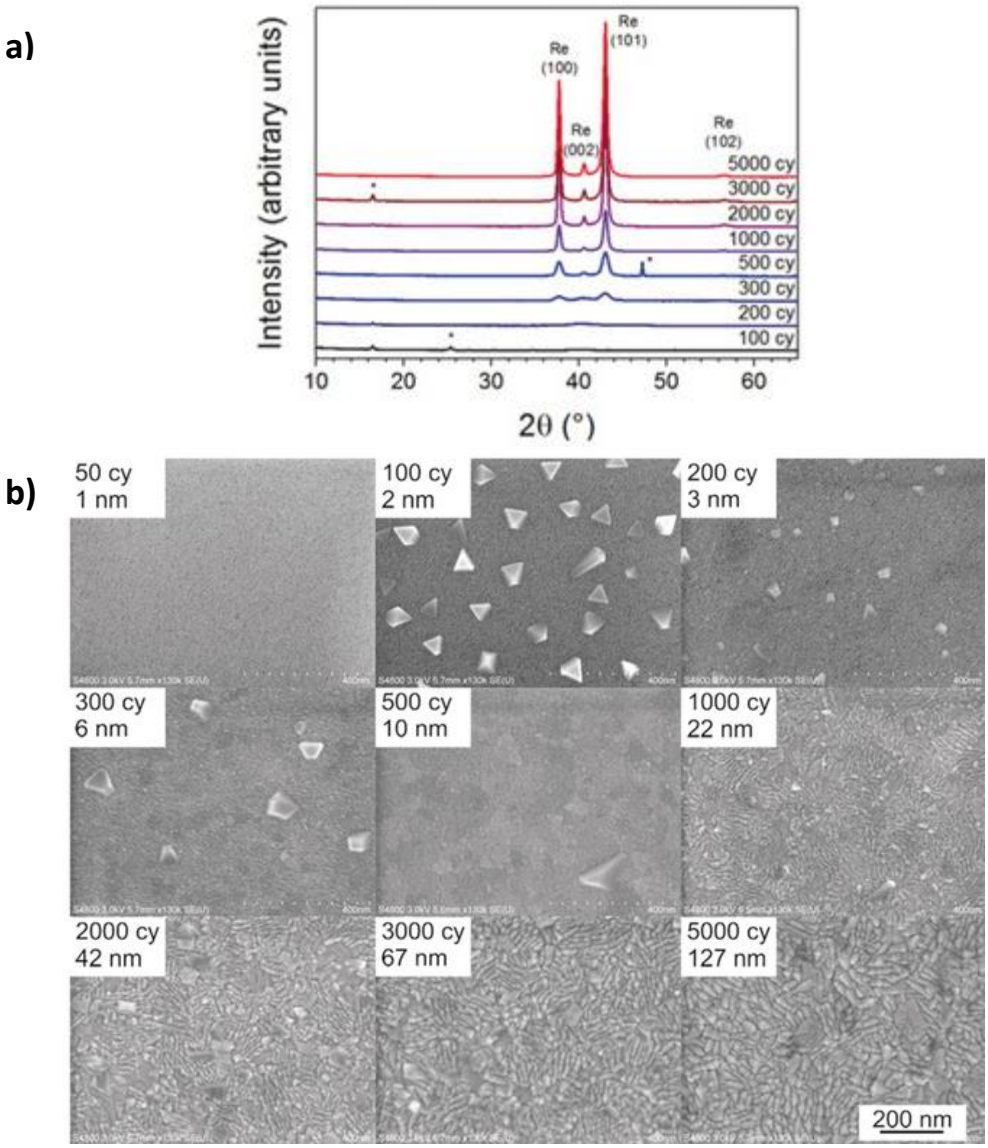

Figure 9. ALD Re films grown on Al_2O_3 films at 400 °C. (a) GIXRD patterns and (b) FESEM images with the numbers of deposition cycles and corresponding film thicknesses. The peaks denoted by asterisks could not be readily identified. Reprinted from Ref. [93] with permission from John Wiley and Sons.

Rhenium has a large number of oxidation states. The stable binary oxides of rhenium are ReO_2, ReO_3, and Re_2O_7.[103] The Re^{6+} cation in ReO_3 is not particularly stable and disproportionates at 400 °C while Re_2O_7 is chemically stable but sublimes at about 300 °C.[103] Mixed-valent rhenium oxide thin films have been prepared for example by RF sputtering[104], DC sputtering[105], and electrodeposition[106–108].

The most widely studied rhenium oxide is ReO_3 due to its low absorption within the visible spectrum, metallic conductivity, and a resistivity (~10 μΩ cm) lower than that of the metallic Re.[93,109] Because of these properties, ReO_3 could be used in applications like superconductors[110] and solar cells[111]. Problems in ReO_3 film deposition include film nonuniformity and contributions from Re with oxidation states other than 6+. For example, Murphy et al.[109] deposited ReO_3 films by reactive magnetron sputtering employing a metallic rhenium target within an oxygen-argon environment. After optimizing the oxygen flow ratio to 50 % and 60 %, XPS studies showed that the films consisted largely of ReO_3 but had also contributions of ReO_2, Re_2O_3, and Re_2O_7. The distribution of chemical states measured for the film deposited with the 50 % oxygen flow ratio after one day of air exposure consisted of 15 % Re^{3+}, 10 % Re^{4+}, 55 % Re^{6+} and 20 % Re^{7+}. Secondary electron micrographs of the films grown with the 50 % and 60 % oxygen flow ratios showed large cracks after 30 days air exposure (Figure 10).

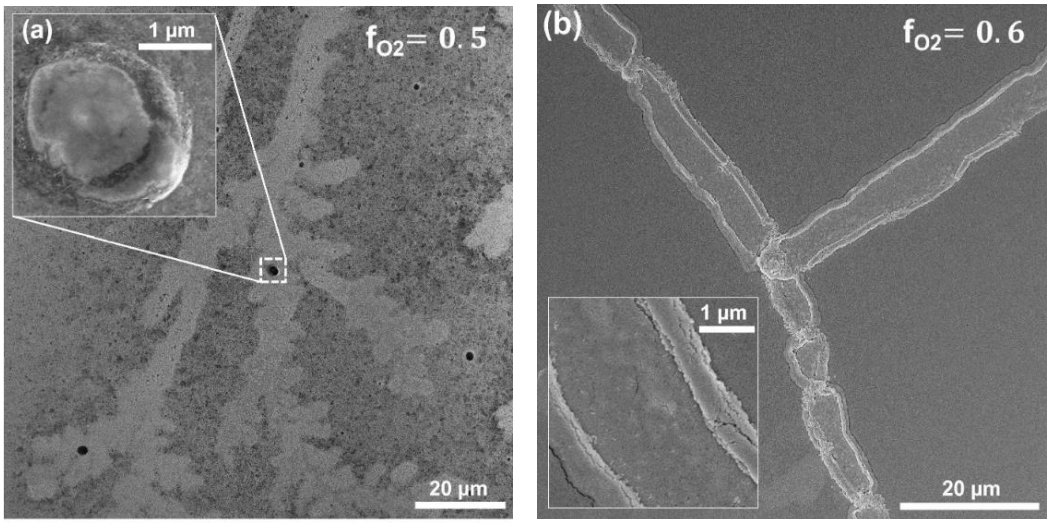

Figure 10. Secondary electron micrographs of rhenium oxide thin films deposited by reactive magnetron sputtering with (a) 50 % and (b) 60 % oxygen flow ratios. Reprinted from Ref. [109] with permission from Elsevier.

To be able to benefit from the properties of ReO_3 in microelectronic applications, ReO_3 films need to be thin, continuous, and conformal even on 3-dimensional structures, which could be possible by employing ALD. Depositing rhenium oxide thin films directly by ALD has not yet been demonstrated, but a film that fits into these standards could be fabricated by converting an ALD Re thin film to ReO_3.

4.2 Aluminum Oxide

Aluminum oxide is the most studied and used ALD thin film material. Its deposition is usually performed by pulsing trimethylaluminum (TMA) and water onto a substrate at 30 - 300 °C. The TMA-H_2O process is almost an ideal self-limiting ALD process and considered to be the model system for ALD. In addition to water, ozone and oxygen plasma have been used as reagents with TMA. Chlorides, bromides, alkoxides, alkylamides, amidinates and mixed ligand compounds have also been studied as aluminum precursors for the deposition of Al_2O_3 films. The vast spectrum of aluminum oxide ALD processes has been reviewed extensively by Miikkulainen et al.[112] Although the upper temperature limit for most organometallic aluminum precursors is about 300 °C, some publications report process temperatures up to 500 °C with TMA. Aluminum oxide films grown below 600 °C on any substrate are amorphous, but crystallization of for example thin (5 nm) films of Al_2O_3 on silicon is possible at 900 °C.[112]

Some of the features leading to the extensiveness of the research and use of Al_2O_3 thin films are their passivation and barrier properties, high thermal stability and conformality as well as excellent dielectric and optical properties.[113] They are widely used in MEMS[114,115], photovoltaics[116], protective coatings[5–7], optics[35,117], electroluminescent displays[2], and semiconductor devices[118,119]. Because of these outstanding features, alumina thin films can also be applied under extreme conditions, such as in space[120,121]. For this, films need to be reliable during outgassing of moisture and temperature variations, for example.[122,123]

Atomic layer deposited Al_2O_3 thin films have shown excellent gas diffusion barrier properties on polymers. They can protect polymers against atomic oxygen and vacuum ultraviolet attacks[121,124], and films as thin as 10 nm have been found to have barrier properties equivalent to glass against water.[125] However, studies have shown that ALD Al_2O_3 films are vulnerable to corrosion for example by water. Dameron et al.[126] studied water vapor transmission rates (WVTR) of 26 nm Al_2O_3 films on Kapton substrates at room temperature with the radioactive HTO tracer method (tritiated water markers). The films were grown with TMA and H_2O at 175 °C. The effective WVTR of films directly facing the HTO was found to be $\sim 1\times10^{-3}$ g/m^2/day. The widely accepted requirement for the WVTR for OLEDs for sufficient lifetimes is 1×10^{-6} g/m^2/day.[127] The WVTR started to increase after

130 h and after 160 h the film dissolved and failed overall to serve as a water vapor barrier.[126]

In addition to declining barrier properties, corrosion by water affects the overall strength of the films. Berdova et al.[123] studied the fracture strengths of 75 nm ALD Al_2O_3 membranes deposited at 110, 150, 200, and 300 °C using TMA and H_2O as precursors. The films were tested as-deposited and after keeping them in an environmental chamber with relative humidity of 95 % at 60 °C for 18 h or after annealing them at 800 °C under nitrogen for 15 minutes. The as-deposited films had high fracture strengths (2.25-3.00 GPa) but exposure to high humidity and annealing decreased the fracture strength significantly (1.25-2.34 GPa) (Figure 11). Corrosion and dissolution of the films in water as well as modification of composition of the film material at high temperatures were speculated as the reasons for the strength decrease.

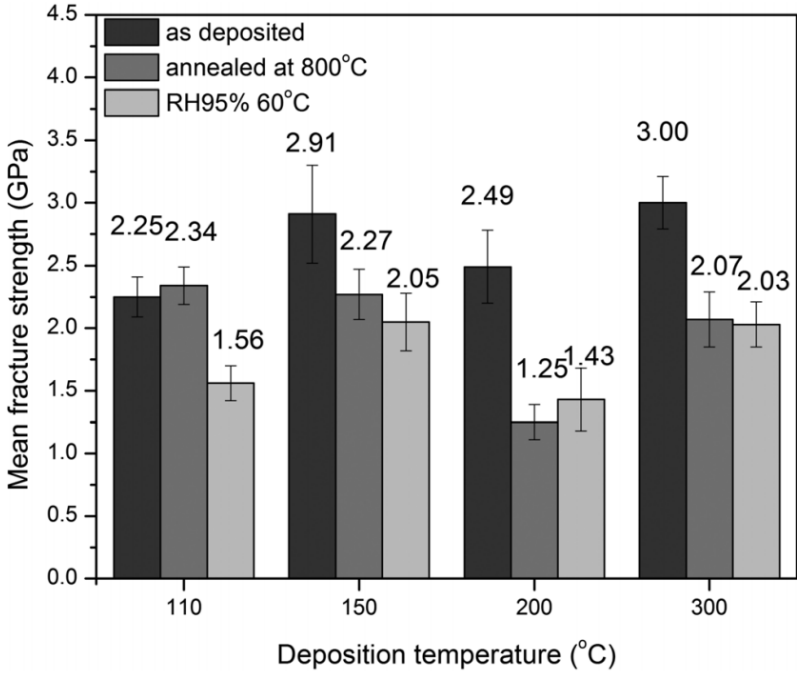

Figure 11. Mean fracture strength values vs deposition temperatures of 75 nm Al_2O_3 films in the as-deposited state, after annealing at 800 °C, and after being in an environmental chamber with relative humidity of 95 % at 60 °C for 18 h. Reprinted from Ref. [123] with permission from American Vacuum Society.

Therefore, Al_2O_3 films must be modified to prevent water corrosion. Abdulagatov et al.[128] successfully prevented water corrosion of copper substrates by employing TiO_2 films together with Al_2O_3 films as barriers. The Al_2O_3 films were grown with TMA and H_2O at 120 °C. TiO_2 films grown with $TiCl_4$ and H_2O were used because of their excellent water resistance properties.[129] Copper substrates coated with either 20 nm ALD Al_2O_3 or 18 nm ALD TiO_2 deposited at 120 °C were submerged into chromatography grade water at 90 °C for 75 h. Both films failed as a barrier: Al_2O_3 due to water corrosion and TiO_2 due to poor nucleation on copper leading to open copper areas (Figure 12 a-c). It was shown with ellipsometry measurements that a 20 nm Al_2O_3 film dissolved completely in 90 °C water within ~10 days. By contrast, combining the two films into a 5.5 nm Al_2O_3 adhesion layer and 20 nm TiO_2 capping layer prevented substrate corrosion in 90 °C water up to 80 days (Figure 12 d-e).

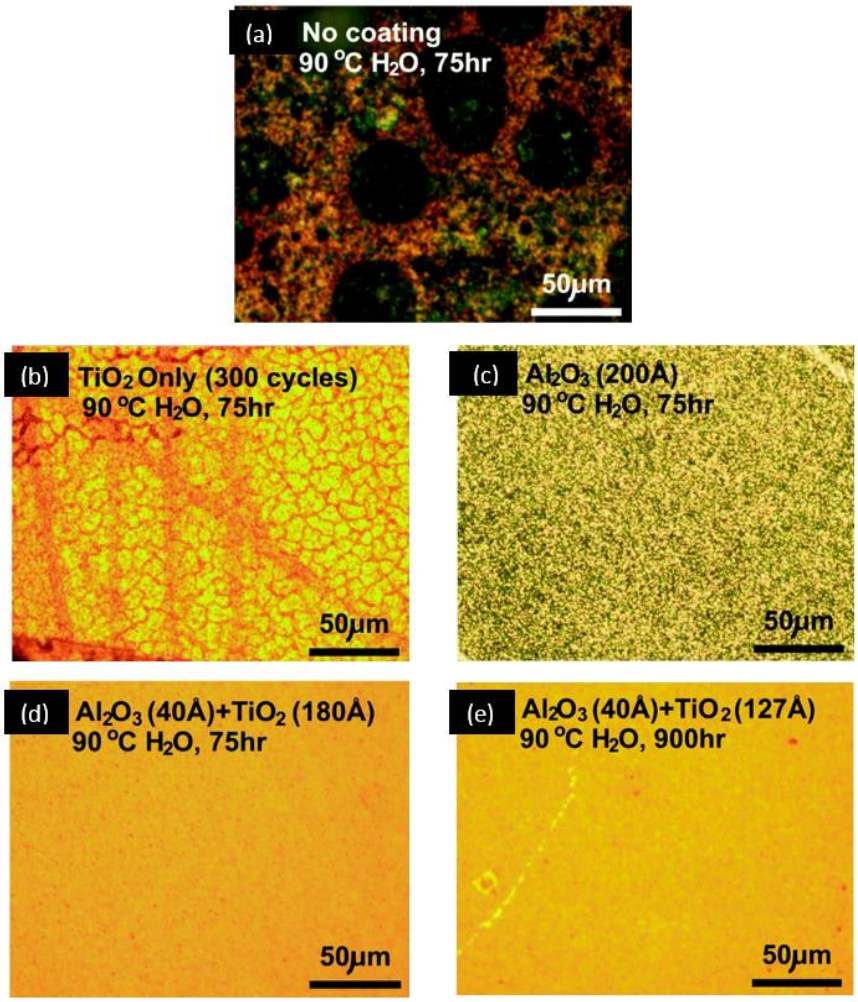

Figure 12. Optical microscope images of copper substrates submerged in 90 °C water for 75 h (a-d) or 900 h (e). Substrates were prepared with (a) no coating, (b) 18 nm ALD TiO_2, (c) 20 nm ALD Al_2O_3, (d) 4 nm Al_2O_3 and 18 nm TiO_2, (e) 4 nm Al_2O_3 and 12.7 nm TiO_2 coating. Reprinted from Ref. [128] with permission from American Chemical Society.

Titania and alumina films can also be combined into nanolaminates (NL) for enhanced water resistance properties. Kim et al.[130] prepared 50 nm Al_2O_3/TiO_2 NL films with PEALD for preventing water corrosion and gas permeation. The nanolaminates consisted of alternating 0.18 nm Al_2O_3 and 0.075 nm TiO_2 layers deposited at 100 °C. TMA and tetrakis(dimethylamino)titanium were used as precursors together with O_2 plasma for Al_2O_3 and TiO_2 films, respectively. The WVTR of the nanolaminate film was found to be 1.81×10^{-4} g/m^2/day on polyethylene naphtalate. Dense film morphology and introduction of TiO_2 into the Al_2O_3 backbone were presented as the reasons for the good barrier qualities. Other materials besides TiO_2 can also be combined with the alumina films for better barrier performance. In the study by Dameron et al.[126] previously mentioned in this chapter, the WVTR of the Al_2O_3 films could be decreased by combining 60 nm ALD SiO_2 layers with 26 nm Al_2O_3 layers to form bilayers. Two Al_2O_3/SiO_2 bilayers reduced the effective WVTR on from$\sim1\times10^{-3}$ of the Al_2O_3 layer to $\sim5\times10^{-5}$ g/m^2/day.

4.2.1 Grass-like Alumina Thin Films

Heikkilä et al.[27] and Kim et al.[130] are one of the earliest to have observed the grass-like structure of Al_2O_3. Kim et al.[130] studied 50 nm Al_2O_3 films grown with PEALD at 100 °C, and found that immersion in 90 °C water degraded the film already in 30 minutes. FESEM and AFM images reveal a conversion of the smooth Al_2O_3 to a "petal-like" morphology (Figure 13). Such a change in morphology was presumed to occur due to the corrosion of Al_2O_3 as described by the reaction equations (1) and (2).[130,131] On the other hand, immersion of a film in water at room temperature first caused a thickness increase from 50 nm to about 200 nm after 200 h of immersion, but after 700 h the film had fully disappeared.

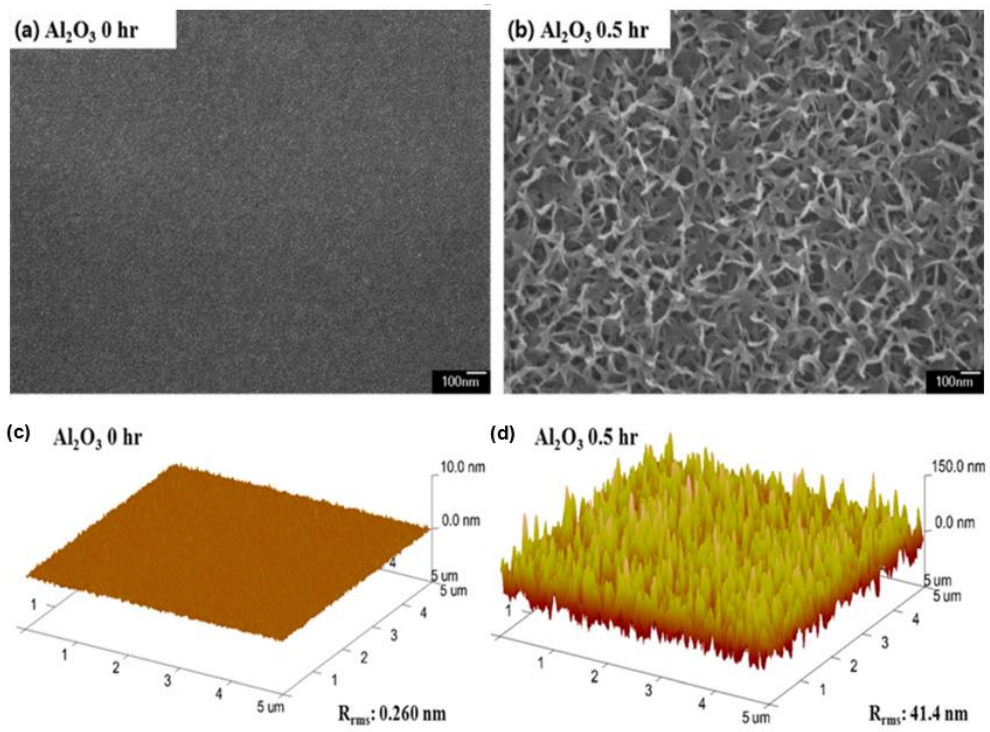

Figure 13. FESEM (a,b) and AFM (c,d) images of 50 nm PEALD Al_2O_3 thin films before (a,c) and after (b,d) immersion in water at 90 °C for 30 min. Reprinted from Ref. [130] with permission from American Chemical Society.

$$Al_2O_3(s) + 6H^+(aq) + 9H_2O(l) \rightarrow 2[Al(H_2O)_6]^{3+}(aq) \quad (1)$$

$$Al_2O_3(s) + 2OH^-(aq) + 3H_2O(l) \rightarrow 2[Al(OH)_4]^-(aq) \quad (2)$$

Grass-like Al_2O_3 film morphology has also been observed in several other studies.[35,132,133] Correa et al.[132] found that a significant increase of Al_2O_3 film stability in aqueous solutions can be achieved by crystallizing and densifying the film by annealing it at 900 °C. Broas et al.[133] made a similar observation on an increase of the stability of ALD Al_2O_3 films in aqueous solutions after being annealed at 800 and 900 °C.

Despite the apparent drawbacks of the stability of alumina films in aqueous solutions, the corroded, petal-like Al_2O_3 thin films may have applications as antireflective coatings. Antireflection coatings are widely used in solar cells and camera lenses, for example. These coatings can be fabricated, for example, by artificially lowering the refractive index of a material through an introduction of nanoscale porosity. The lowest refractive index achieveable with a dense inorganic material coating is not low enough for the minimization of the Fresnel reflection at normal incidence on glass. Therefore, the petal-like, or grass-like, alumina coating is a good antireflection coating for glass. Other applications could include Raman spectroscopy and cell cultivation substrates as well as etch masks and nanoporous filters.[35]

Grass-type alumina coatings for antireflection applications have been previously studied.[134–136] These coatings have been prepared by sol-gel and anodic methods followed by immersion in hot water. Kauppinen et al.[35] and Isakov[137] fabricated these coatings with ALD of Al_2O_3 followed by immersion in hot water. The advantage of this method is its superior conformality on the substrate enabled by ALD. In their work, 28 nm Al_2O_3 thin films were deposited with TMA and H_2O at 120 °C on Si and glass. After that, the films were immersed in deionized water (DIW) at 20-90 °C for 30 min. AFM and SEM images as well as ellipsometric measurements revealed that no major changes took place at temperatures below 40 °C. From 50 °C and up, a major decrease in the refractive indices and increase in the thicknesses, spectral transmittances and roughnesses of the films occurred (Figure 14).

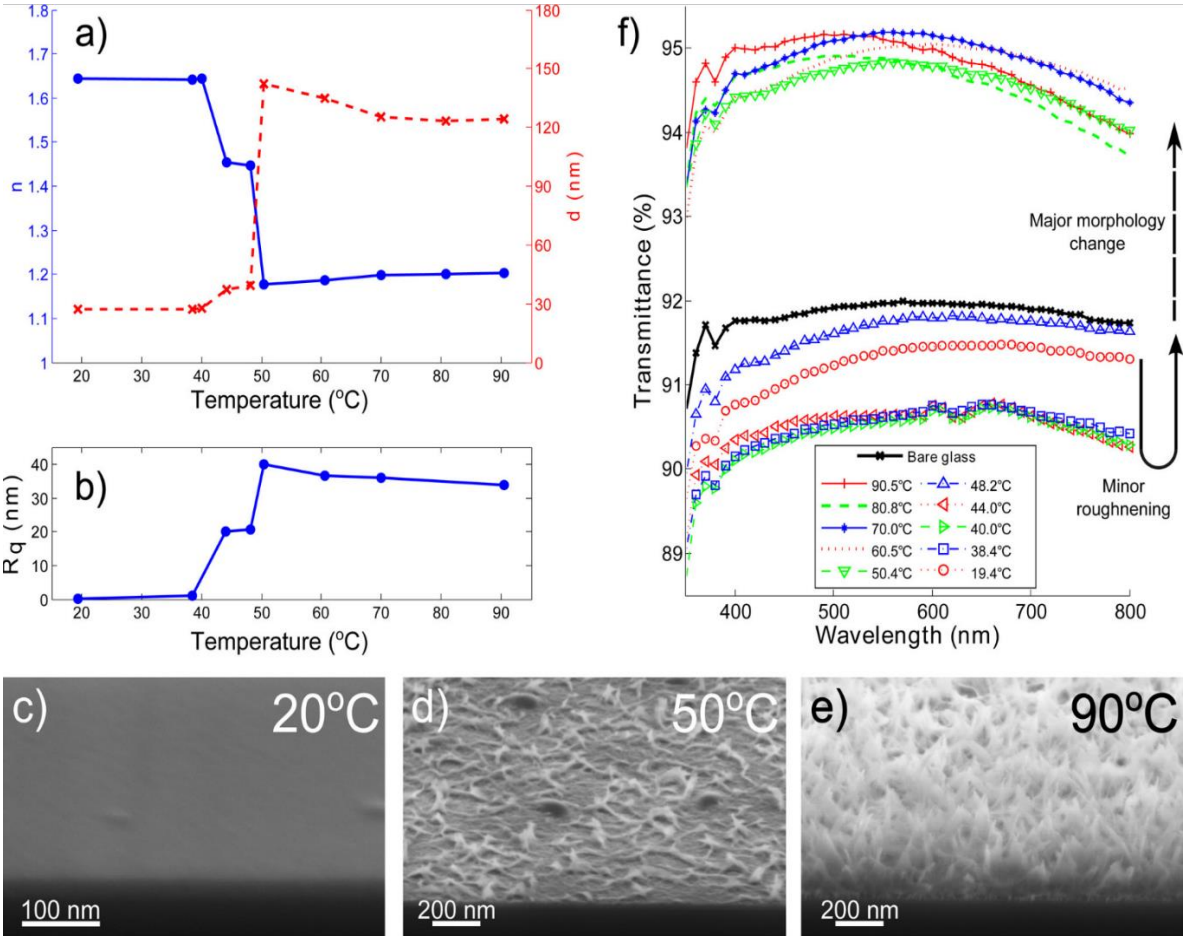

Figure 14. Properties of a 28 nm Al_2O_3 ALD thin film immersed into deionized water for 30 min at different temperatures. (a) Refractive indices and thicknesses measured with an ellipsometer. (b) Surface roughnesses of samples on silicon measured by AFM. (c-e) SEM images of the films taken at an angle of 18° from the plane of the substrate. (f) Transmission spectra of samples on glass at normal incidence. Reprinted from Ref. [35] with permission from American Chemical Society.

The observed changes can be attributed to the significant morphological conversions of the films from smooth to “grass-like” (Figure 14 c-e). The ideal refractive index for a coating on glass for Fresnel reflection minimization is 1.22, and the samples with the highest transmittance had refractive indices of approximately 1.20. The coatings also exhibited extreme omnidirectionality. Figure 15 shows a cross sectional image with a simulated refractive index profile of the film treated with DIW at 90 °C. The refractive index profile was simulated by fitting a transfer-matrix method calculation to the transmittance spectrum of a double-sided coated glass sample after treatment at 90 °C. It can be seen that the film has a thickness of approximately 200 nm, and the authors considered SEM as

a more reliable thickness measurement since in the ellipsometer measurement a uniform film was assumed. Therefore the ellipsometry measurements should be considered as approximations. The simulated refractive index profile reveals that the bottom parts of the film are less affected by the DIW treatment because the refractive index is very close to the untreated Al_2O_3 film (1.64 for the untreated and 1.6 for the bottom parts of the treated).

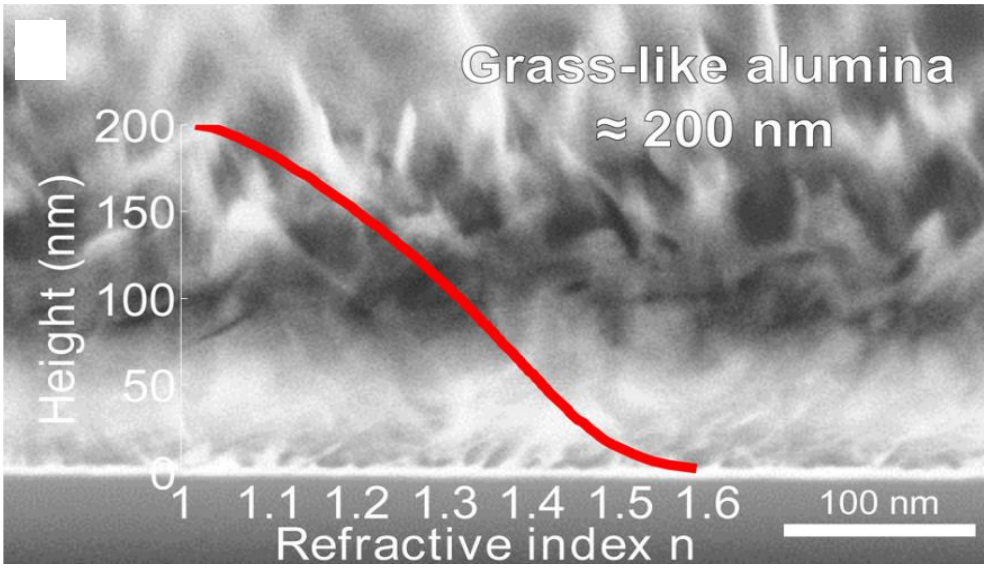

Figure 15. Cross-sectional SEM image of an ALD alumina film after DIW treatment at 90 °C for 30 min with simulated refractive index profile. Reprinted from Ref. [35] with permission from American Chemical Society.

The authors kept the DIW treated films in ambient conditions for several weeks and did not notice any observable changes. The group successfully deposited this grass-like alumina coating on a cleaved black silicon surface to demonstrate the possibility to coat surfaces with extreme topographies. Figures 16a-c show cross sectional SEM images of a black silicon surface (a), the same surface conformally coated with 28 nm ALD Al_2O_3 (b), and the alumina-coated surface after the DIW treatment.

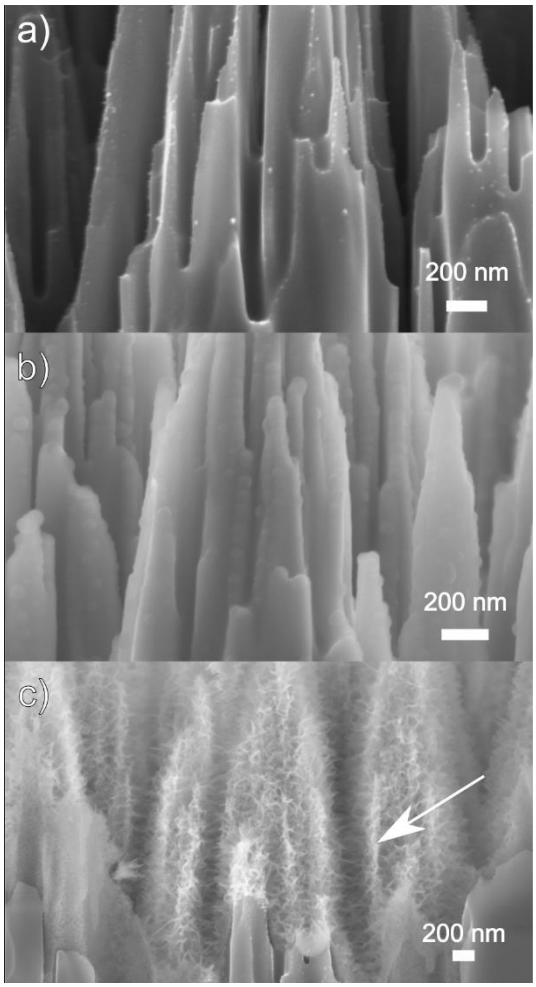

Figure 16. Cross section SEM images of (a) a cleaved black silicon surface, (b) the same surface with a conformal 28 nm ALD alumina coating, (c) and the coated surface after DIW treatment. Reprinted from Ref. [35] with permission from American Chemical Society.

The films in these studies were blown dry with a nitrogen stream after removal from the DIW. Isakov[137] speculated that the grass-like flakes of the films might arise from the drying of the samples: the Al_2O_3 thin films have regions with different atomic ordering, and during the DIW treatment the most favorably ordered regions stay intact while bonds to the less favorable orientations are broken. These intact pieces of alumina then form the flakes while blow-drying the sample due to the high surface tension of water.

4.3 Metal-Organic Frameworks

Metal-organic frameworks (MOFs) are coordination networks made of metal-containing units held together by organic linker molecules and containing voids (Figure 17). The metal units (ions or clusters) and organic linkers can be varied to make new materials, offering unique chemical versatility. Thousands of MOFs are prepared and studied each year.[138] The common practice for naming MOFs is to give them trivial names based on their place of origin followed by a number, for example HKUST-1 (Hong Kong University of Science and Technology, [Cu_3(1,3,5-benzenetricarboxylate)$_2$]) and UiO-66 (Universitet i Oslo, Zr[1,4-dicarboxybenzene]). The first mentions of MOFs, then known as coordination polymers, can be dated back to the 1980s[139], and structures with permanent porosity were first reported in the late 1990s as MOFs.[140,141] MOFs can be synthesized as powders and shaped to pellets or extrudates if so required by the application. Sometimes the MOFs need to be grown as thin films to function as needed.[42]

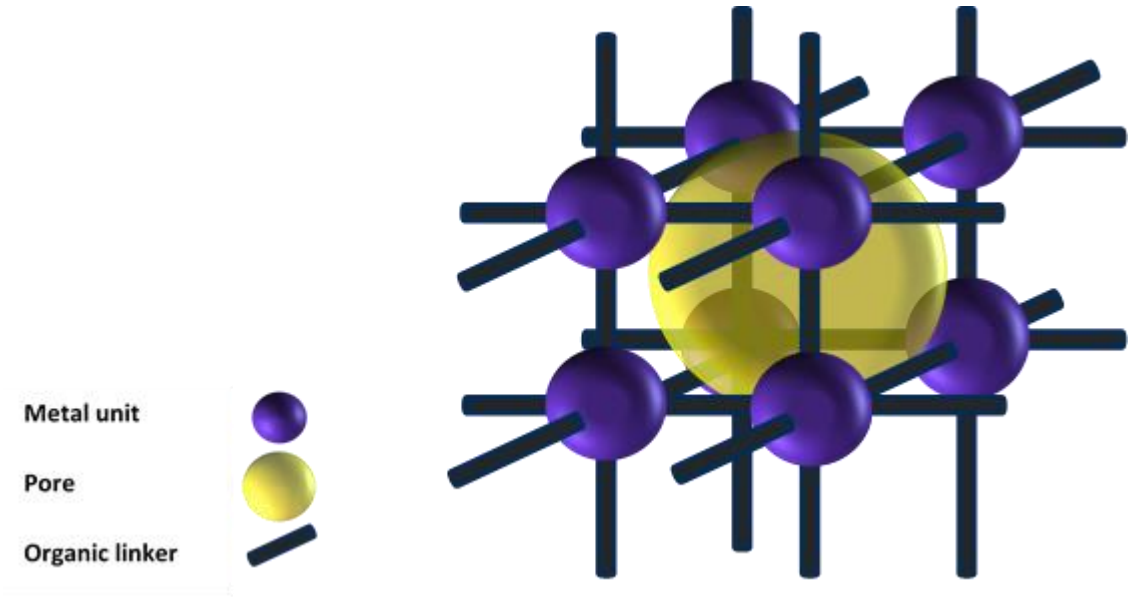

Figure 17. An illustration of a typical MOF structure.

4.3.1 Properties of Metal-Organic Frameworks

Each application of a specific MOF is based on its well-defined crystalline chemical structure. The structure can be carefully tuned in terms of its metal units, organic linkers, and shape and size of the pores. The organic linkers are bonded to the metal units coordinatively, making the structure fairly flexible. Other porous structures like zeolites have a high contribution of covalent bonds which leads to rigidity. Another unique characteristic of MOFs is that the metal sites can be accessible to chemical compounds (open metal sites, OMS), while in zeolites the metal atoms are blocked.[142] The versatility of MOFs also offers extraordinarily large and permanent porosity as well as the highest surface areas per gram of any known material.[143] Applications of MOFs include catalysis[144–147], gas storage and separation[148–150], sensing[151,152], drug delivery[153], and self-cleaning surfaces[154].

The efforts to prepare MOFs with ultrahigh, stable porosity and large surface area have led to the concept of secondary building units (SBUs) and the isoreticular principle, which allow varying MOF constituents in a precisely controlled manner.[155] Examples of SBUs and organic linkers are shown in Figure 18[138]. By controlling the chemistry and pore size of MOFs, structures with exceptional chemical, thermal and/or mechanical stability have been synthesized. The stability of MOFs is a vital requirement for applications and has been the focal point in many papers covering the synthesis of novel MOFs. [138,156–162]

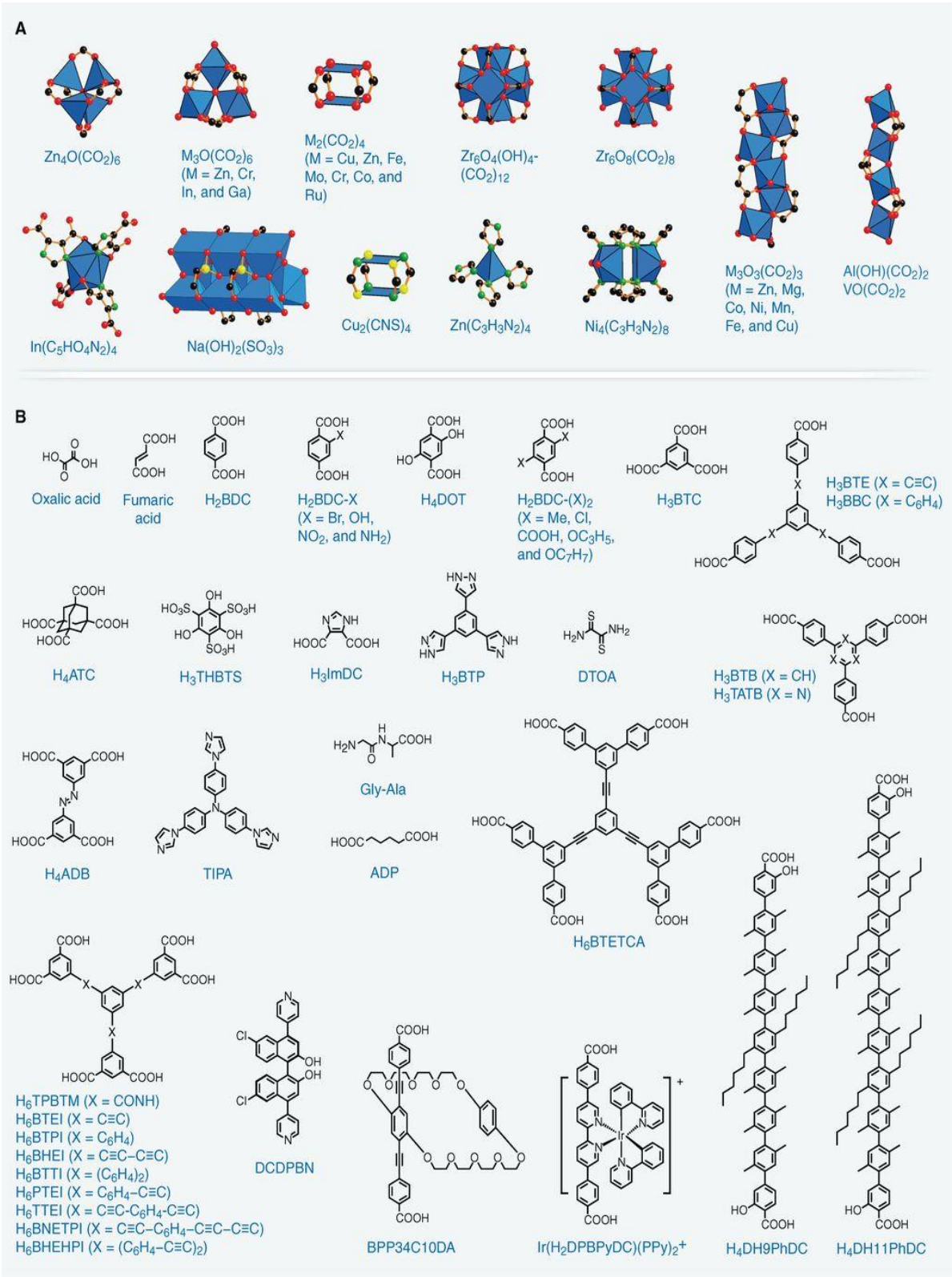

Figure 18. Examples of known inorganic secondary building units (A) and organic linkers (B) of MOFs. Color code: black, C; red, O; green, N; yellow, S; purple, P; light green, Cl; blue polyhedra, metal ions. Hydrogen atoms are omitted for clarity. AIPA, tris(4-(1*H*-imidazol-1-yl)phenyl)amine; ADP, adipic acid; TTFTB4^{-}, 4,4′,4″,4‴-([2,2′-bis(1,3-dithiolylidene)]-4,4′,5,5′-tetrayl)tetrabenzoate. Reprinted from Ref. [138] with permission from AAAS.

4.3.2 Metal-Organic Framework Thin Films

MOF thin films can be classified as polycrystalline (< 50 µm) or ultrathin (nm range) with almost perfect orientation. Polycrystalline MOF thin films, which will be labelled as P-MOFs for clarity, consist of randomly oriented crystals or particles that can either completely cover the substrate or be scattered on a surface. Their properties are expected to be similar to those of the corresponding powder material. Nearly perfectly oriented MOF thin films, which will be labelled as SURMOFs for clarity, are smooth (roughness approximately a few elementary cells), and their properties can differ from the polycrystalline films because of their dimensions and close proximity to the surface.[163]

Interface effects between the substrate and film as well as surface effects due to high specific surface areas are found in SURMOFs. For example, lattice shrinkage compared to bulk material dimensions has been observed.[164] This might arise from the increased surface ratio of thin films, increasing surface energy and strain, shrinking the lattice. Another explanation might simply be the lattice mismatch between the support and MOF.[165] When film thicknesses exceed the nm range, interfacial strain decreases, so it is necessary to shrink the films down to nm order for these unique properties. Other properties owing to the small dimension MOF films include: dynamic gate opening, in which the sorption of guest molecules promotes the rearrangement of the flexible MOF crystal structure so that it starts to take up the guests[166], improved gas separation abilities[167], and metastable structures[168]. Down-sizing also facilitates the study of MOF structures and has made it possible to reveal coordination processes in certain MOFs.[169] MOF thin film applications include gas separation (molecular sieving)[170,171], sensing[172,173], and low-k dielectrics[174] as well as tunable conductors[175] in microelectronic devices.

4.3.3 Fabrication Methods for Metal-Organic Framework Thin Films

Synthesis of MOF thin films can be very complex because the growth of crystalline material needs to be promoted selectively on a support. Typical ways of preparing MOF thin films involve depositing the film on top of a substrate using known bulk methods for the selected MOF. Self-Assembled Monolayers (SAMs) on typical substrate materials like Si are often used because they have a long-range 2D order and abundant functional sites that can be patterned easily on the substrate. Growth of MOFs has been achieved selectively on patterned SAMs. For example Hermes et al.[176] created a patterned MOF-5 thin film by anchoring MOF-5 building units selectively on carboxylate-terminated SAMs. In their work, a Au-substrate with patterned SAMs of 16-mercaptohexadecaonic acid and 1H,1H,2H,2H-perfluorodecane thiol was immersed into a supersaturated reaction mixture used for the synthesis of MOF-5 macrocrystals. The MOF-5 thin film was formed only on the carboxylate-terminated areas of the SAMs. The resulting MOF squares had dimensions of $40 \times 40\ \mu m^2$ and the crystallites were about 100-500 nm in size (Figure 19).

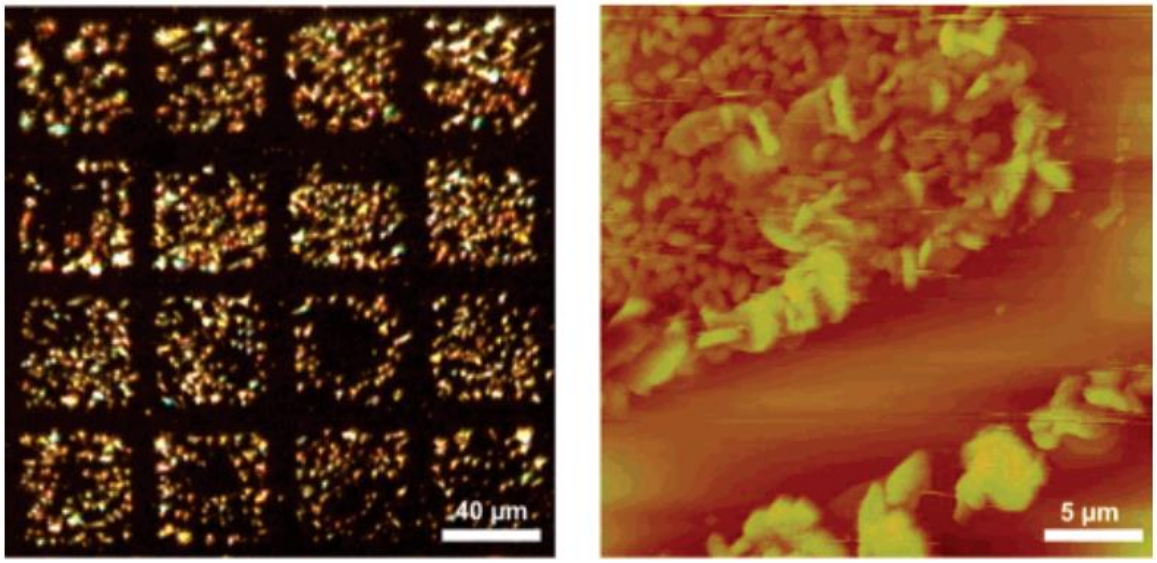

Figure 19: An optical microscope (left) and AFM (right) image of a MOF-5 thin film grown selectively on patterned SAMs. Reprinted from Ref. [176] with permission from American Chemical Society.

In addition to SAMs, metal oxide thin films on selected typical substrates can be used as precursors for MOF thin film fabrication.[33,177,178] The metal oxide film provides the metal ions required for the nucleation and growth of MOFs close to the substrate[178] and may stabilize the MOF thin film formation, as shown by Lemaire et al.[179]. The study analyzed HKUST-1 thin film nucleation on ALD Al_2O_3, ZnO and TiO_2 thin films in solvothermal growth at 120 °C. The MOF grew remarkably faster on ZnO compared to the other two oxide films due to the formation of zinc-copper hydroxy double salts (HDS). It was shown that the HDS are reaction intermediates that accelerate the MOF formation by promoting a high rate of anion exchange in the linker solution. The structure and consequently the stability of the HDS depends on the composition of the metal oxide used. As with the patterned SAMs, HKUST-1 could be grown selectively on the ZnO areas of patterned wafers.[179,180]

The most common methods used for SURMOF fabrication are layer-by-layer deposition and Liquid-Phase Epitaxy (LPE). In LPE, the substrate is alternately dipped in a solution of positively and negatively charged polymers, and the MOF components are adsorbed from the liquid phase to a surface in a layer-by-layer manner. SAM layers are often formed on substrates as bases for SURMOF fabrication because they can dictate the orientation of the MOF in addition to the features previously mentioned. In the layer-by-layer deposition, the SAM covered substrate is sequentially dipped in solutions of the structural components of the MOF. In both methods, resulting film thicknesses can be controlled through the number of immersion cycles.[163]

P-MOFs have been prepared by immersing substrates in appropriate solutions or growing pre-deposited seeds into films.[163] The solvothermal method is one of the most direct methods: substrates are submerged into a mother solution of the MOF and the solution is heated. A mother solution is an aged MOF synthesis solution that contains MOF building blocks. The film can also form from the mother solution without heating; the substrate is simply dipped in the MOF mother solution several times, with each dip forming new seeds on the substrate surface and growing larger those already present. Another way for fabricating P-MOF thin films at room temperature is to heat the mother solution to initiate crystallization, filter it and submerge the substrate into the crystallite-containing solution. The solutions can also be prepared without saturation of the MOF components, attaining a crystalline MOF film when the solvent is evaporated. Other approaches include

electrochemical methods[181], seeded growth[182–184], solution shearing[185], and diffusing reactants through a polyethyleneoxide gel[186].

4.3.4 Limitations of Solvent-based Methods

Deposition of MOF thin films by methods requiring solutions is often simple, effective, and of low cost at a lab scale. Solvent-based chemistry is an excellent platform for MOF fabrication because the dissolved building units are mobilized efficiently for crystallization by self-assembly. Solvents may also increase the chemical stability of the building blocks and promote crystallization.[187] Film deposition requiring solutions can be, however, troublesome at industrial scales in terms of sustainability, chemistry and cost.

Solutions typically used for MOF processing contain metal salts that can react with unwanted surfaces, such as the deposition container walls, and may cause particle contamination to the film in the form of MOF particles forming in the solution itself. Solutions may also not wet the substrate surface completely, unlike vapors directed on a surface.

Solvents in MOF fabrication, such as dimethylformamide (DMF), are often toxic and harmful to both the environment and operator. Solution-based processes yield larger volumes of waste than vapor-based ones because vapor precursors can be simply neutralized directly at the reactor exhaust. Handling of high-purity solvents and liquid waste are heavily regulated, and large volumes of these lead to high production costs.[42] These problems could be overcome by developing solvent-free, vapor-based MOF thin film deposition methods.

4.3.5 Vapor Phase Methods

A nudge towards solvent-free MOF fabrication methods was a powder milling process in where powders of linkers and metal precursors are milled together to attain MOFs.[188] Here the linker is protonated and acts as an acid towards the metal precursor. The protonated counter anion of the metal salt can be considered as a fluid and plays an important role in the reaction by enabling the neutralized M-L building blocks to mobilize and self-assemble during crystallization. Sometimes stoichiometric amounts of fluid molecules are added to the reaction to boost the crystallization (Fluid Assisted Synthesis, FA, Figure 20)[42], as has been done for example by Friščić et al.[189] In their work, different porous frameworks were obtained with mechanosynthesis. First, ZnO and fumaric acid were ground in a 1:1 stoichiometric ratio but no reaction was observed. By adding small quantities of ethanol or methanol to the process, different MOFs could be obtained. The amount of fluid was so minute that it did not serve as a solvent[190]. Another way of boosting crystallization is to supply heat to the reaction (Figure 20).[42]

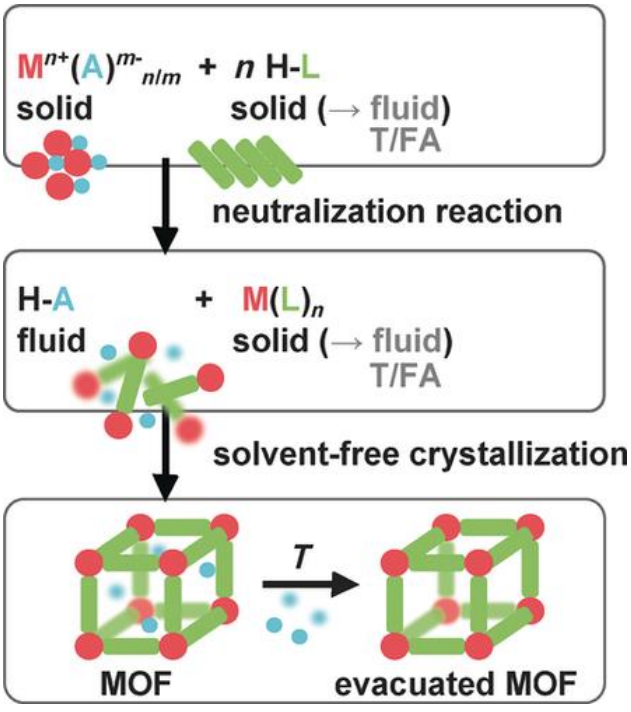

Figure 20. Solvent-free synthesis of MOFs demonstrated via one metal cation inorganic node (M), conjugate base organic linker (L), and protonated counter anion fluid (H-A). Thermal treatment (T) and the addition of stoichiometric amounts of fluid molecules (FA) are also portrayed. Reprinted from Ref. [42] with permission from John Wiley and Sons.

Vapor deposition techniques can be divided into Physical Vapor Deposition (PVD) and CVD methods. In both methods the precursor is vaporized, and the vapor is transported to the substrate in vacuum conditions. The difference is that in PVD the precursor is a vapor of the material to be deposited and in CVD the precursor(s) undergo a chemical reaction with each other or the substrate to form the desired material. PVD methods are seldom used for the fabrication of MOF thin films because MOFs have low vapor pressures and their thermal decomposition temperatures are fairly low (from 300 °C). It has been difficult to obtain intrinsically nanoporous materials through PVD methods. CVD methods, in contrast, offer versatility in the choice of precursors and process conditions. CVD methods also enable precise growth of MOF thin films on complex surfaces, improved film quality, industrial scale reproducibility, and control over building block mobility.[42]

MOF-CVD consist of a conversion-type vapor-solid reaction between a precursor film and an organic linker vapor. This can be done in a layer-by-layer manner (Molecular Layer Deposition, MLD) or through one step. An example of a one-step MOF-CVD is the formation of Zeolite imidazole framework 8 (ZIF-8) by Stassen et al.[33], where an ALD zinc oxide thin film was exposed to 2-methylimidazolate vapor at 100 °C for 30 minutes. The sacrificial oxide film was converted to ZIF-8 fast without solvents. Lausund and Nielsen[43] prepared UiO-66 by depositing zirconium terephthalate films from $ZrCl_4$ and 1,4-benzenedicarboxylic acid (terephthalic acid) followed by crystallization under acetic acid at 160 °C for 24 h. Fabrication methods for ZIF-8 and UiO-66 will be discussed in detail in sections 4.4.1 and 4.5.1.

By using uniform and defect-free ALD thin films as precursors for vapor-phase MOF thin film fabrication we can open doors towards applications in microelectronics, for vapor-phase conversion of ALD thin films can be integrated with existing processes in microelectronics manufacturing. This can also be a route towards non-corrosive synthesis methods and a way around problems caused by solvent-based methods, such as chemical contamination or stiction of small features.

4.4. ZIF-8

Zeolite imidazole frameworks (ZIFs) are a subclass of MOFs that have high surface areas as well as exceptional chemical and thermal stabilities. They have a similar topology as inorganic zeolites: large pores and small apertures. ZIFs have a sodalite-type structure where transition metal cations are linked together by imidazole ligands in a tetrahedral, three-dimensional framework.[191,192]

ZIF-8 is an elastic framework that consists of Zn^{2+} metal ions coordinated to nitrogen atoms of the 2-methylimidazolate (mIM) linker. It has hydrophobic pores with a diameter of 11.6 Å, which are accessible through six-membered ring apertures with diameters of 3.4 Å (Figure 21a)[171]. ZIF-8 has attracted a lot of interest in gas separation applications because its pore apertures are in the range of the kinetic diameters of many gas molecules and its adsorption capacity for gases such as CO_2 is high (Figure 21b)[170]. The hydrophobicity of the pores enables gas separation even from mixtures with steam, which is an advantage over zeolites.

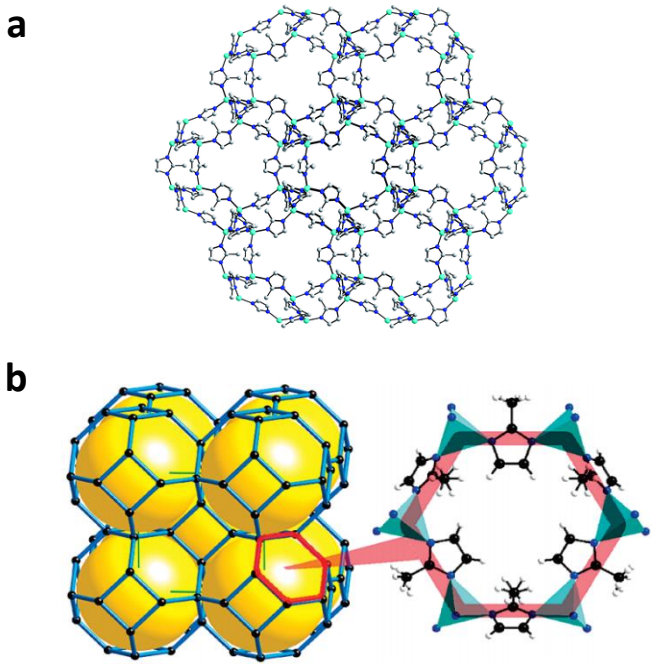

Figure 21. a) The crystal structure of ZIF-8. Cyan, blue and grey spheres represent Zn, N, and C atoms, respectively. H atoms have been omitted for clarity. Reprinted from Ref. [170] with permission from Royal Society of Chemistry. b) A representation of the narrow six-membered ring opening through which molecules have to pass. The yellow spheres represent the pores. Reprinted from Ref. [170] with permission from American Chemical Society.

4.4.1 ZIF-8 Thin Films

ZIF-8 thin films have been fabricated in a number of ways, and Table 2 summarizes some of the methods reported in literature. A vast majority of the methods are solution-based, and only in the recent years have ZIF-8 films been prepared through vapor phase based techniques. In addition to many precursors needed to deposit the films, solution-based methods involve a multitude of time-consuming steps the duration of which has usually not been disclosed. Vapor-based methods generally involve only one or two steps and comprise of converting a ZnO thin film into ZIF-8 by delivering HmIM vapor on the film. Thicknesses of MOF films fabricated through solution-based methods are generally higher than those made by vapor-based methods. Deposition temperatures in the solution-based methods range from room temperature to 150 °C, whereas the vapor-based methods always require a vaporization temperature starting from 100 °C to obtain a sufficient vapor pressure of the HmIM linker.

Table 2. Synthesis methods for ZIF-8 thin films. The durations refer to the shortest times reported for all the synthesis steps together (solution preparation, seed preparation, conversion etc.), but any substrate preparation times have been excluded. Temperatures refer to the highest temperature used in the fabrication process. Minimum film thicknesses refer to the smallest film thicknesses obtained with each process.

Method	Substrate	Minimum film thickness	Temperature	Duration	Year, reference
Solution based					
Microwave-Assisted solvothermal synthesis	Porous titania	~30 nm	100 °C	> 1 day	2009[170]
Dip coating from mother solution	Si wafers, amorphous silicon	100 nm/cycle	RT	> 30 min	2010[172,192]
Seeded growth	α-Alumina supports	5 µm	100 °C	30 min	2011[193]
Seeded growth	Tubular α-Alumina supports	~ 5 µm	100-150 °C	> 1 day	2010[171]
Dip-coating in colloidal solution	Silica wafers	40 nm	130 °C	> 1h	2010[173]
Solvothermal growth	α-Alumina	20 µm	120 °C	> 1 day	2010[194]
Microwave-assisted solvothermal synthesis	Titania	~25 µm	100 °C	4h	2011[195]
Slow diffusion	Flexible nylon membrane	18 µm	RT	> 72h	2011[196]
Conversion of ALD ZnO layers through microwave-assisted solvothermal synthesis	Tubular porous ceramic support	15-20 µm,	80 °C	1h	2014[197]
Solvothermal conversion	Si wafers	~95 nm	100 °C	24h	2014[178]
Solvent-free					
Conversion of sputtered ZnO films and flakes * (solid-solid or solid-melt conversion)	Si wafers	>1 µm	160 °C	1 min	2013[177]
Vapor conversion of ALD ZnO films	TiO_2 film on silicon wafers and pillars	52 nm	110 °C	40 min	2016[33]
Vapor conversion of ZnO and AZO fibers	ZnO and AZO fibers	fiber diameters 200-400 nm, 100% conversion	200 °C	42h for AZO, 68h for ZnO	2018[52]

Control of MOF thin film microstructure is important because it affects the optical, electrical, magnetic, and gas transport properties of the films. Film microstructure has been a focal point in many ZIF-8 thin film fabrication studies. For example, McCarthy and coworkers[194] found that film microstructure can be controlled by changing the pH of the mother solution in a solvothermal process for ZIF-8 thin films. An increase in the pH of the mother solution resulted in omnidirectional growth of larger, well-intergrown ZIF-8 crystals.

ZIF-8 structured thin films have been exploited in sensing applications by monitoring their refractive index (*n*). The refractive index of a MOF thin film is a volume-weighted average of the indices of the cavities and the framework limiting the cavities. The *n* of vacuum is equal to one and that of the framework greater than one. When a molecule is inserted into the cavity, vacuum is displaced and the refractive index of the material increases. This can be detected by a Fabry-Pérot device: the Fabry-Pérot device produces interference peaks when light waves pass through it, and these peaks shift when the refractive index of the material changes. Lu et al.[172] examined UV-vis transmission spectra of ZIF-8 thin films exposed to ethanol and water vapors and found that there were notable shifts in the interference peak positions when ethanol concentration in the water vapor increased (Figure 22).

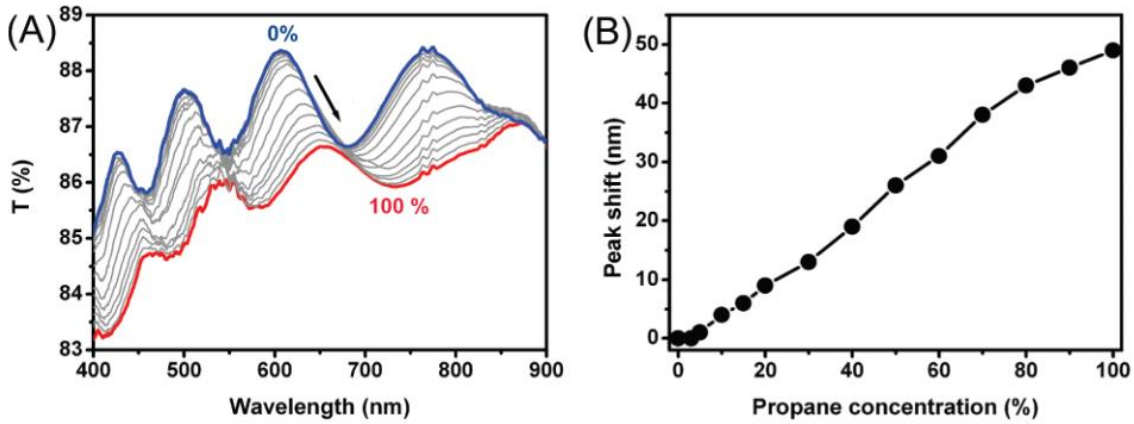

Figure 22. UV-vis transmission spectrum of a ~950 nm ZIF-8 film grown on glass on exposure to water and ethanol vapor (A). Interference peak shift from 612 nm as a function of ethanol concentration (vol%) in ethanol/water vapor mixtures (B). Reprinted from Ref. [172] with permission from American Chemical Society.

Stassen et al.[177] studied the effects of conversion time and initial ZnO film thickness on the crystal size and morphology of the resulting ZIF-8 film. They partly converted sputtered, patterned (*via* microcontact printing), or electrochemically deposited flake-like ZnO films to ZIF-8 films (Figure 23) with control over crystal size. The conversion was done by covering the ZnO films with a thin layer of finely ground HmIM powder and heating to 160 °C with the aim of melting the HmIM powder and wetting the sample surface completely. Reaction times were varied from 1 to 20 minutes. The samples were then cooled down to room temperature and washed with methanol to remove any excess linkers. For a completely solvent-free synthesis, the methanol rinse step was proposed to be substituted with an evaporation step. Longer reaction times appeared to lead to ripening of the crystals, resulting in larger crystals (Figure 24). It was also observed that increasing the initial ZnO film thickness from 0.1 to 0.5 µm and therefore increasing the amount of zinc available for growing the crystals yielded larger crystals with a similar reaction time (Figure 25). It was hypothesized that with smaller initial ZnO film thicknesses, Zn^{2+} ions are depleted sooner, ceasing crystal growth.

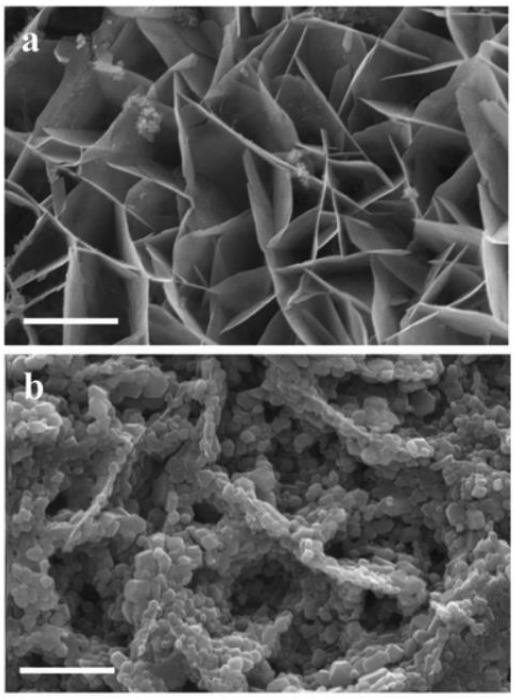

Figure 23. SEM images of (a) electrochemically deposited flake-like ZnO precursor film and (b) the resulting ZIF-8 film after a 20 min conversion time. Scale bars: 5 µm. Reprinted from Ref. [177] with permission from Royal Society of Chemistry.

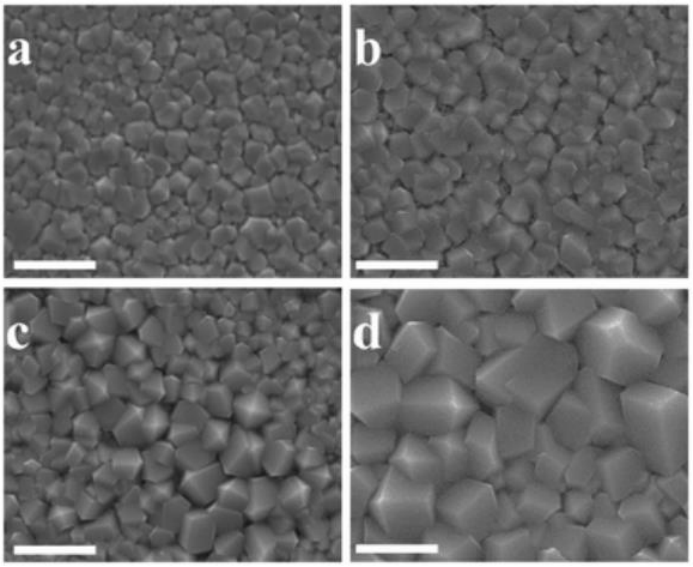

Figure 24. SEM images of ZIF-8 films obtained by a conversion of a 1 μm thick sputtered ZnO precursor films for (a) 1 min, (b) 2 min, (c) 5 min, and (d) 10 min. Scale bars: 5 μm. Reprinted from Ref. [177] with permission from Royal Society of Chemistry.

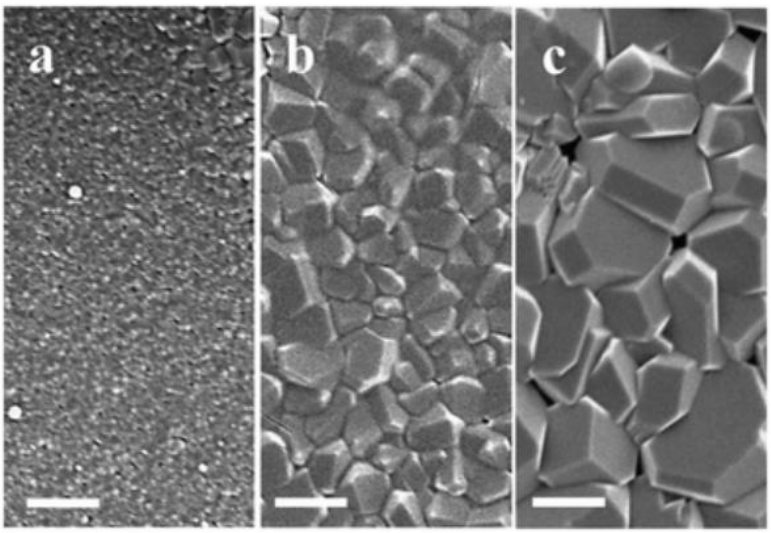

Figure 25. SEM images of ZIF-8 films obtained by a 20 min conversion of ZnO precursor films with initial thicknesses of (a) 0,1 μm, (b) 0,5 μm, (c) 1 μm. Scale bars: 5 μm. Reprinted from Ref. [177] with permission from Royal Society of Chemistry.

The first method for vapor deposition of ZIF-8 thin films was reported by Stassen et al. in 2016.[33] ALD ZnO films with thicknesses of 3-15 nm were deposited on top of a 40 nm thick ALD TiO_2 film and the overlying ZnO film was converted to ZIF-8 by exposing it to HmIM vapor. The TiO_2 film served as an adhesion layer to bridge the MOF to the SiO_2 substrate and improved the resulting film morphology. The conversion method consisted of three steps: first the ZnO film and a reaction vessel with HmIM powder were separately pre-heated to 100 °C, then the substrate was suspended top-down 5 cm above the HmIM powder in the reaction vessel for 30 minutes, after which the substrate was activated by placing it on a hot plate at 110 °C under a nitrogen flow for 10 minutes. The purpose of the post-conversion activation was not explained. The formation of ZIF-8 was confirmed with XRD (Figure 26) and complete conversion of 10 nm as well as thinner ZnO films to ZIF-8 films was verified via TEM.

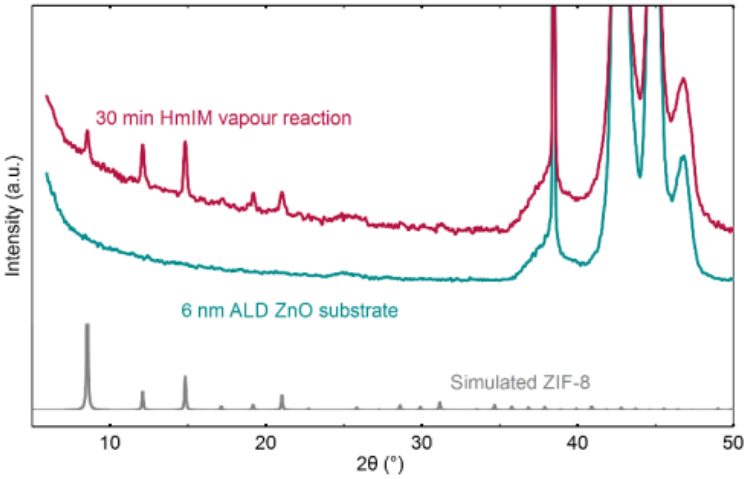

Figure 26. XRD patterns of a ZnO substrate, ZIF-8 film formed by a 30 min conversion reaction, and a simulated ZIF-8 film. The wide peaks above 35° appear most likely due to the SiO_2 substrate. Reprinted from Ref. [33] with permission from Springer Nature.

To demonstrate the conformality of the MOF-CVD process, ZIF-8 films were also deposited on silicon pillars with a 25:1 aspect ratio[33]. The initial thickness of the ALD ZnO film was 25 nm (Figure 27). MOF patterns with the highest resolution made by photolithography in literature were formed through lift-off patterning combined with MOF-CVD (Figure 28). In lift-off patterning a lithographically patterned photoresist serves as a mask on the substrate

during vapor-phase material deposition. The mask is removed after the deposition step in order to leave a pattern of the deposited material on the substrate. Photoresists may swell or dissolve in a typical MOF synthesis solution, so the solvent-free MOF-CVD method offers an advantage for careful patterning of MOF films. In this study, ZnO was deposited through directional reactive sputtering and converted to 1.7 µm wide ZIF-8 rings with MOF-CVD (Figure 28). Also functionalized elastomeric pillar arrays were coated with ZIF-8 films by MOF-CVD without affecting their structural integrity, which might not be the case with solvent processes.

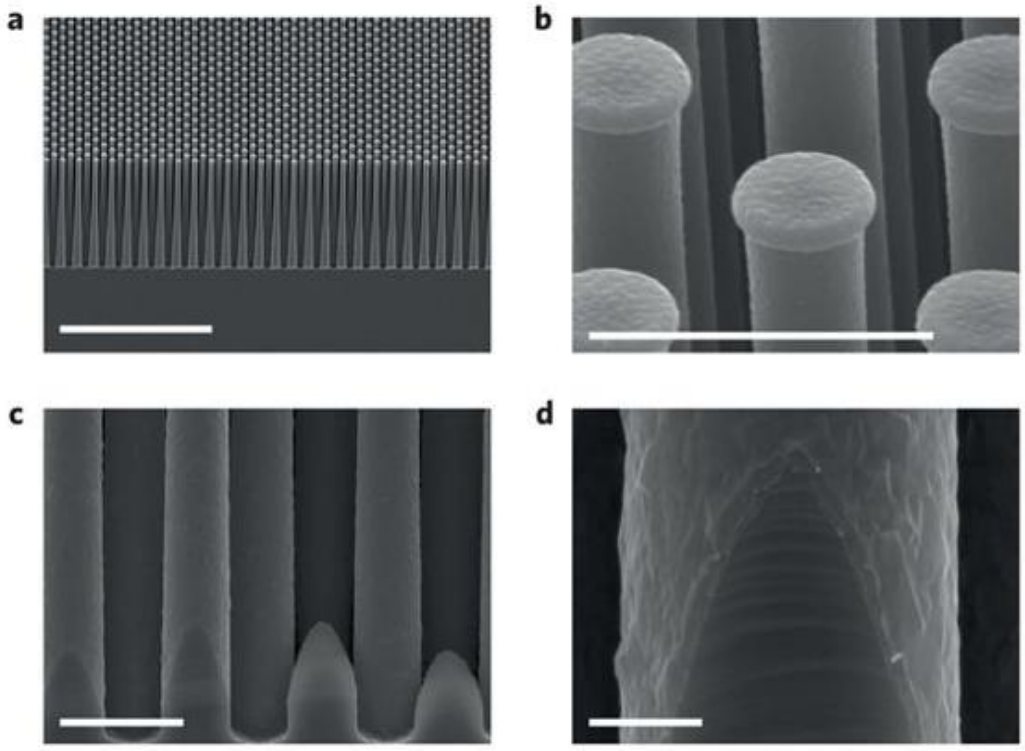

Figure 27. SEM images of (a,b) a ZIF-8 -coated silicon pillar array. (c,d) High-magnification SEM images illustrating the uniform coverage at the base of the pillars. Scale bars (a) 50 µm, (b,c) 5 µm and (d) 1 µm. Reprinted from Ref. [33] with permission from Springer Nature.

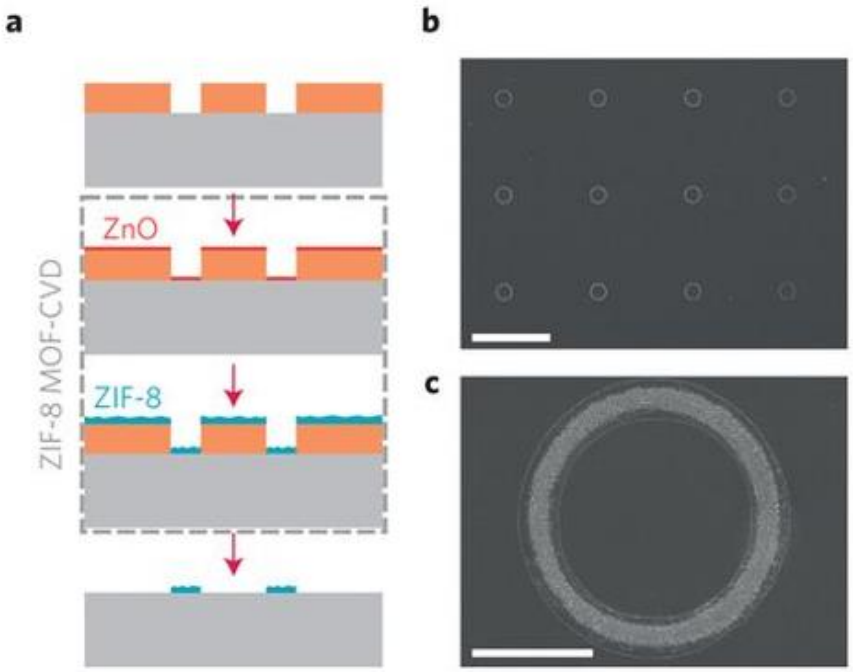

Figure 28. (a) Schematics of MOF-CVD combined with lift-off patterning for making ZIF-8 structures. The photoresist is shown in orange. (b,c) SEM images of the resulting ZIF-8 patterns. Scale bars: (b) 100 µm and (c) 10 µm. Reprinted from Ref. [33] with permission from Springer Nature.

The conversion of zinc oxide to ZIF-8 occurs by the reaction:

$$\mathrm{ZnO\ (s) + 2HmIM\ (g) \rightarrow H_2O\ (g) + Zn(mIM)_2\ (s)}$$

Water is formed as a byproduct in the neutralization reaction between ZnO and HmIM. It was proposed based on *in situ* XRD experiments that water forms a liquid-like layer at the reaction interface and serves as a catalyst and mobilizing medium for the MOF building blocks (Figure 29a)[33]. This was supported by the inability to readily resume the conversion after interruption, which caused dehydration and immobilization of the surface layer: after placing the substrate again under the reactive atmosphere the reaction could not be readily resumed. The important role of water in this process is analogous to the fluid molecules described in section 4.3.5. Similarly, water plays an important role also in solvent-free crystallization of zeolites as reviewed in detail by Wu et al.[198]

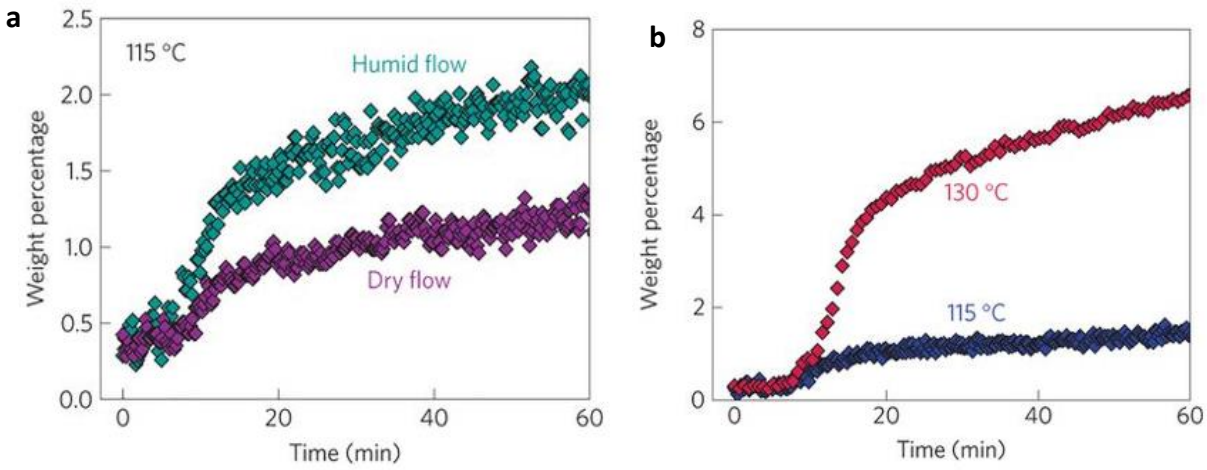

Figure 29. ZIF-8 phase quantification by *in situ* XRD measurements on the conversion reaction. In these experiments, a ZnO film was exposed to HmIM vapor at 115 °C under a continuous dry nitrogen flow (purple) and a nitrogen flow humidified to 33 % relative humidity at room temperature (green) (a), and crystallization rate of ZIF-8 at 115 and 130 °C described by phase quantification by *in situ* XRD experiments (b). Reprinted from Ref. [33] with permission from Springer Nature.

In situ XRD experiments also revealed that the crystallization rate of the MOF increased as a function of time until leveling off after a certain amount of time (Figure 29). Raising the reaction temperature resulted in a higher ZIF-8 mass fraction even though the crystallization rate leveled off at about the same time as at the lower temperature (Figure 29b). It was deduced that the forming ZIF-8 layer acts as a diffusion barrier for Zn^{2+} ions and organic linkers (in this case HmIM) alike, which slows down the reaction. The elevated reaction temperatures mobilize Zn^{2+} ions better, forming more ZIF-8 crystals and thicker films.

Studies on ZIF-8 fibers disagree with the observations on ZIF-8 thin films regarding ZIF-8 conversion thickness.[33] Holopainen et al.[52] examined the conversion of calcined electroblown ZnO and aluminum doped ZnO (AZO) fibers to ZIF-8 via a vapor-phase reaction. The conversion reaction was conducted in an autoclave by exposing the fibers to HmIM vapor at 150 and 200 °C for 1-68 h (Figure 30). After the reaction, the cooled fibers were placed in an oven at 150 °C for at least 2 h to remove any excess HmIM. The initial fiber diameters ranged from 200 to 400 nm and they were fully converted after 42 hours resulting in ZIF-8 fibers with diameters over 1 µm, which means that the reaction can

penetrate much deeper into the ZnO matrix than previously reported[33]. The higher conversion reaction temperatures led to larger diameters of ZIF-8 fibers, as compared to ZIF-8 film thicknesses obtained by MOF-CVD at 100-115 °C[33]. Also the homogeneity of the ZIF-8 fibers was noted to improve with higher reaction temperatures. Additionally it was observed, in agreement with Stassen's et al.[177] previous study on a conversion of ZnO films to ZIF-8 films *via* a solid-melt conversion reaction with HmIM powder, that the ZIF-8 crystallite size increased with longer reaction times. Complete conversion of ZnO fibers to ZIF-8 was verified by XRD measurements.

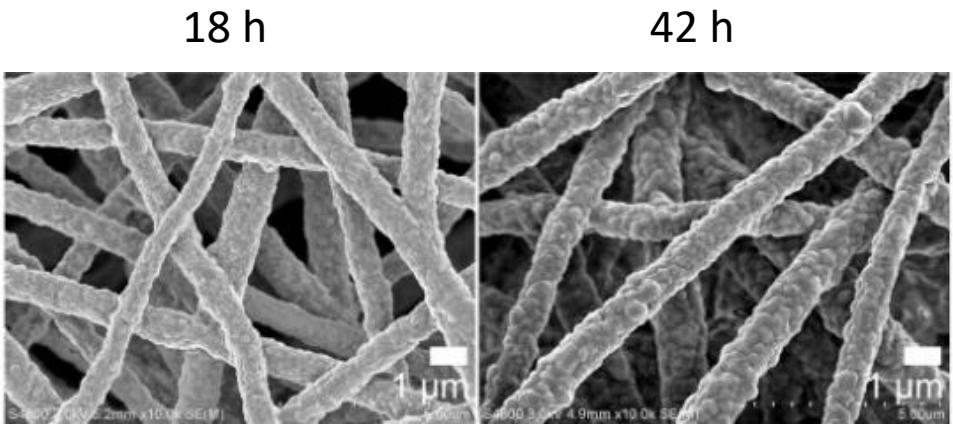

Figure 30. SEM images of ZIF-8 fibers prepared from ZnO fibers calcined at 500 °C by conversion treatment at 200 °C for 18 h (left) and 42h (right). Reprinted from the open-access article from Ref. [52] under the terms of the Creative Commons Attribution 4.0 International License.

4.5 UiO-66

UiO-66 has been named by its place of origin: Universitet i Oslo. UiO-66 is comprised of $Zr_6O_4(OH)_4$ nodes and benzenedicarboxylic acid (BDC) linkers. The six Zr^{4+} ions in the nodee are arranged in an octahedral geometry and the four hydroxide ions and four oxide ions are located at the centers of each facet of the octahedra. These nodes are coordinated with twelve BDC linkers so that each Zr atom is coordinated with eight oxygen atoms in a square antiprismatic geometry, as shown in Figure 31. This leads to a face centered cubic crystal structure with tetrahedral and octahedral cages with diameters of 0.7 and 0.9 nm, respectively. These cages are accessible through triangular windows of about 0.6 nm in diameter.[199]

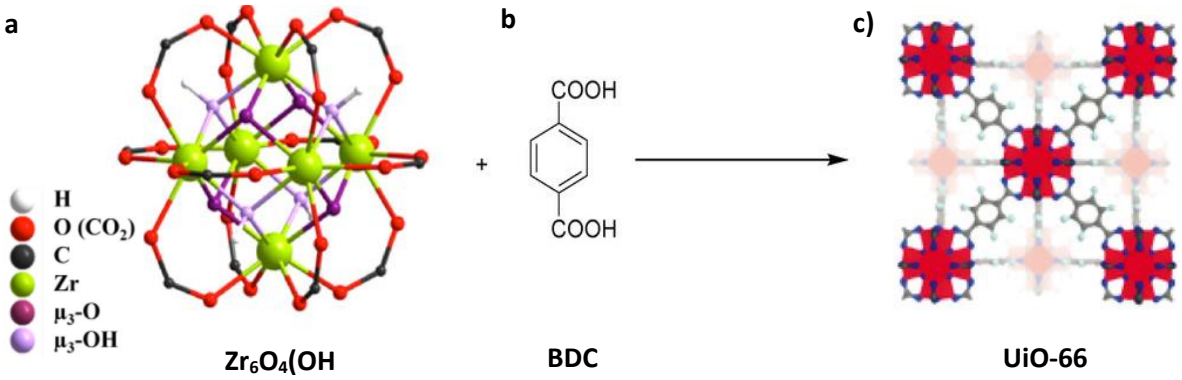

Figure 31. A depiction of the node (a) and linker of UiO-66 (b), and an illustration of the UiO-66 structure (c). Reprinted from Ref. [199] with permission from John Wiley and Sons.

In addition to the properties common to all MOFs, including high surface area and open metal sites, the most relevant properties of UiO-66 are its high thermal[199], mechanical[200] and chemical[201] stability. It can be heated up to 375 °C without collapsing the structure and it is stable in the presence of corrosive reagents such as hydrochloric acid and various amines.[199] These properties allow for multiple applications, including drug delivery[202], catalysis[199,203], gas storage,[204] and gas separation[205].

It has been observed through neutron powder diffraction measurements that bulk UiO-66 does not have a perfect crystal structure and typically contains linker vacancy defects. On average, one out of every 12 linkers is absent. This is atypical for MOFs where the inorganic nodes are commonly coordinated 4-, 5-, or 6-fold to their linkers, unlike with UiO-66, so the impact of the structural disorder would be increased with such a high concentration of missing linkers.[204]

Introducing acetic acid into the solvothermal synthesis of bulk UiO-66 has revealed its role in defect promotion and crystal growth. By adding acetic acid into the solutions, the crystallinity of the MOF can be improved. By increasing the amount of acetic acid in the synthesis, the UiO-66 pore volume can be enhanced by 50 % and BET surface area by 60 %.[204] As the defect content increases, the uptake of gases such as CO_2 is enhanced by almost 50 % at high pressures (35 bar), which emphasizes the applicability of UiO-66 in gas adsorption and the interplay between the preparation method and functional properties.

4.5.1 UiO-66 Thin Films

Table 3 summarizes methods that have been used to fabricate UiO-66 thin films. This material is a fairly new addition to the MOF thin film family, but many processes have been developed. Most of them include a vast amount of solvents and are time consuming with durations from minutes to several days. The solvent-free methods consist of gas-phase conversions of zirconium terephthalate hybrid MLD thin films. The conversion times are 23-24 h. Both solvent-free and solvent-based methods produce films with large thicknesses: solvent-free methods have yielded UiO-66 films with thicknesses from 500 nm to 7.5 µm and solvent-based methods from 82 nm to 2 µm. The advantage of solvent-based methods is the possibility for room temperature syntheses, yet solvent-free processes are more compatible for microelectronic and other industrial applications. In many processes, acetic acid is added as a modulator to improve crystal growth.

Table 3. Synthesis methods for UiO-66 thin films. The durations refer to the shortest times reported for all the synthesis steps together (solution preparation, seed preparation, conversion etc), but exclude any substrate preparation times. Temperatures refer to the highest temperature used during film deposition. Minimum film thicknesses refer to the smallest film thicknesses obtained with each process.

Method	Substrate	Temperature	Minimum film thickness	Duration	Year, reference
Solvent based					
Electrophoretic deposition	Fluorine-doped tin oxide glass (FTO)	RT	-	3h	2014[206]
Solvothermal	FTO + carboxylic acid terminated SAMs	120 °C	2 µm	24h	2015[207]
Electrochemical deposition (anodic and cathodic)	Anodic: Zr foil, Cathodic: Zr foil, Ti, titanium nitride on Si-wafer	108 °C	<1 µm	30 min	2015[208]
Solvothermal	SAMs terminated with BDC	120 °C	900 nm	> 4 days	2016[209]
Hydrothermal	Optical fiber with polymer coating	120 °C	1.6-1.9 µm/layer	24h	2017[210]
Solution shearing	Si wafers	130 °C	-	0.25 mm s^{-1}	2017[185]
Vapor-assisted conversion	Au	100 °C	200 nm	3h	2018[211]
Spin-coating	Si wafers	RT (assumed)	380 nm	21 min	2018[212]
Dip-coating	Si wafers	RT (annealed at 200 °C)	285 nm	> 5 min	2018[212]
Self-assembly	Si wafers	RT (assumed)	273 nm	> 25 min	2018[212]

Table 3 continued

Method	Substrate	Temperature	Film thickness	Duration	Year, reference
Solvent based					
Solvothermal	Si wafers	100 °C	-	54 h	2018[212]
Layer-by-layer	Si wafers	40 °C	153 nm	~12h	2018[212]
Coordination modulator Liquid phase epitaxy	Si wafers	70 °C	82 nm	~33 h	2019[213]
Vapor phase					
Gas-phase conversion	amorphous zirconium terephthalate hybrid MLD film	160 °C	500 nm	24 h	2016[43]
Gas-phase conversion	Zr-BDC films on Si	200 °C	7.5 µm	23 h	2018[51]

Lausund and Nielsen[43] successfully converted zirconium terephthalate hybrid MLD thin films (ZrBDC) to UiO-66 thin films through a gas-phase process. The hybrid thin films were deposited with $ZrCl_4$ and 1,4-BDC (terephthalic acid) as precursors. Film thickness increased by 20 % when exposed to a moist environment of 70-75 % relative humidity at room temperature for 24 h due to terephthalic acid crystallizing on the film surface. This was eliminated by introducing an acetic acid pulse after the terephthalic acid purge step to the MLD ZrBDC film deposition process. It was shown by X-ray reflectance (XRR) and Fourier-transform infrared (FTIR) methods that the acetic acid pulses direct the film bonding scheme from mixed mono- and bidentate coordination to only bidentate coordination, resulting in denser films.

ZrBDC films deposited *via* the acetic acid modulated process were crystallized to UiO-66 films by sealing them in an autoclave with ~0.1 ml of acetic acid at 160 °C for 24 h. Film crystallinity was verified with XRD which showed a diffractogram similar to a powder diffractogram simulated for desolvated UiO-66 (Figure 32a). The film thickness increased from 229 nm (ZrBDC) to roughly 500 nm (UiO-66, Figure 32b). The coordination changed from bidentate to bridging, which is the coordination configuration of UiO-66. Samples deposited without the acetic acid modulation had some acetic acid left in the UiO-66 films after the autoclave treatment in acetic acid.

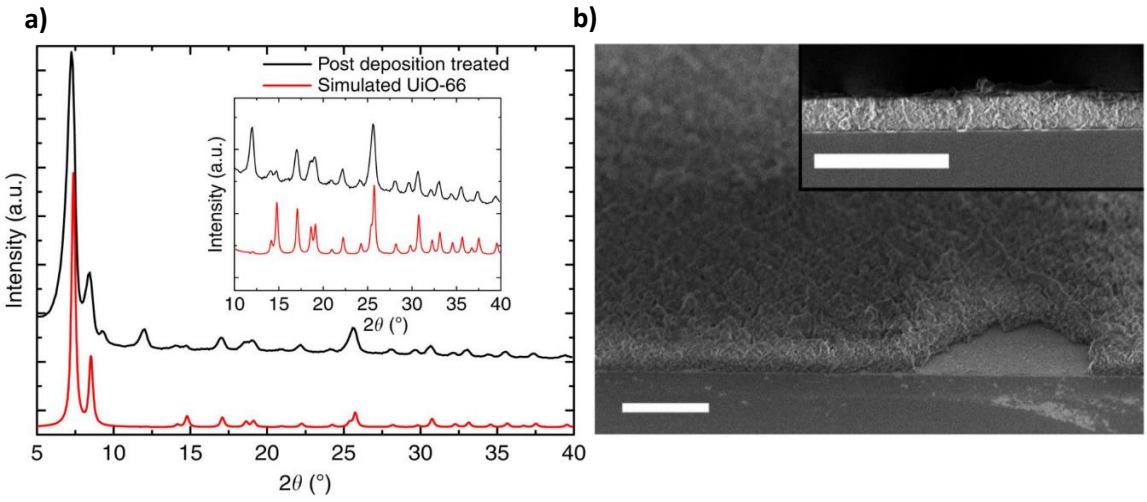

Figure 32. a) GIXRD diffractogram of a UiO-66 film after a treatment under acetic acid at 160 °C for 24 h (black) and simulated powder diffractogram for desolvated UiO-66 (red). The inset shows the same diffractograms zoomed in the 2Θ angles between 10 and 40 degrees. b) Cross-section SEM images of a UiO-66 film viewed at 45 ° and 90 ° (inset). Scale bar: 2 µm. Reprinted from the open-access article Ref. [43] under the terms of the Creative Commons Attribution License.

Lan et al.[51] prepared UiO-66 thin films with a process slightly modified from that of Lausund and Nielsen[43]. A ZrBDC thin film was deposited by MLD with an acetic acid modulation similar to Lausund and Nielsen. The resulting film was pre-heated in an oven to the conversion temperature for 10 min and then placed in an autoclave with 4 ml acetic acid at 200 °C for 23 h. The pre-heating was done to ensure that no acetic acid could condense on top of the film. This procedure led to a complete conversion of ZrBDC to UiO-66 and a thickness increase from 200 nm to 7.5 µm. The amount of acetic acid used for the conversion was considerably larger than what Lausund and Nielsen[43] used in their similar process. When less than 4 ml of acetic acid was used or the conversion time was below 21 h, the conversion was incomplete. The extensiveness of the conversion was not commented in the study by Lausund and Nielsen.[43]

In addition to acetic acid used as a modulator in thin film growth, methacrylic acid (McOH) and water have been studied as crystal growth promoters. Semrau et al.[213] prepared UiO-66 thin films *via* a layer-by-layer method by submerging an UV activated silica substrate alternately into ethanol solutions of $Zr_6O_4(OH)_4(OMc)_{12}$ ($McO^- = H_2C{=}C(CH_3)CO_2^-$) and 3 mM H_2BDC at 70°C. The substrate was submerged into each solution for 10 minutes and 80 deposition cycles were repeated for each film. The substrate was washed with ethanol for 5 min in between the immersion steps. This deposition process resulted in amorphous thin films.

Crystalline films with thicknesses of 82 to 744 nm were obtained by adding water to the H_2BDC solution and McOH to both precursor solutions. The amounts ranged from 0-300 equivalents of McOH and 0-1000 equivalents of H_2O with respect to the SBU. The crystalline films did not cover the substrates completely but instead formed islands with small (<1 µm) spaces in between. The addition of McOH led to thinner and more densely packed films. Increased amounts of H_2O added resulted in smaller crystallite domains and increased the deposited mass. The crystalline films had the predicted stoichiometry, unlike the amorphous films synthesized without McOH and water, which had considerable zirconium and oxygen deficiency.

5 Summary

Conversion reactions of ALD thin films occur when the starting ALD thin film material transforms chemically to another material and atoms rearrange. Conversion reactions have enabled thin film materials with the properties of ALD without direct ALD. For example, some first-row transition metals are typically deposited as nitrides and subsequently annealed or reduced to form the metallic film. Additionally, conversion has allowed for the crystallization of amorphous thin film materials. Conversion can also alter film morphology, may enable the use of a broader selection of substrate materials, and can serve as a pathway for removing ALD thin films that cannot be conventionally etched.

The literature review of this thesis focused on the properties and current preparation methods of five selected materials: RuO_2, ReO_3, Al_2O_3 grass, ZIF-8, and UiO-66. Their synthesis in a thin film form has proven to be immoderately complex, if not impossible, to this day. These are materials that could benefit from the properties of ALD, and conversion reactions might enable their thin film deposition.

Even though noble metal thin films are known for their remarkable resistance to oxidation, many noble metal oxides have been deposited by thermal ALD. The processes, however, need very careful control of growth parameters. Ruthenium has many viable ALD processes, but the deposition of RuO_2 has proven to be challenging. ALD would allow for crystalline, smooth, and conformal RuO_2 thin films but developed processes have been observed to be extremely delicate, required long incubation periods and yielded poor morphology. Zero metal valence precursors, varying substrate materials, and exceptionally long O_2 pulses have been examined to solve these issues. Conversion of Ru into RuO_2 is an appealing concept since the ALD of Ru is more straightforward than that of RuO_2.

Another example of a noble metal oxide that could benefit from conversion reactions is ReO_3. Rhenium has only one existing ALD process. ReO_3 has no published ALD processes, but for example mix valent ReO_3 thin films have been deposited by magnetron sputtering. It has been observed that thin (3-10 nm) Re films react with ambient air to form ReO_x but

rhenium nitride thin films do not exhibit this behavior. Another problem of these films is their nonuniformity. No studies of conversion of ALD Re to ReO_x have been published even though it could be the missing link between uniform ReO_3 films and a facile synthesis route.

Aluminum oxide is the most studied ALD thin film material due to its almost ideal self-limiting process and vast number of applications. Despite its great passivation and barrier properties, ALD Al_2O_3 films are vulnerable to corrosion by water. It has been observed that if the exposure of alumina films to liquid water is not prolonged, instead of fully corroding away, the Al_2O_3 film converts from flat and smooth to a three dimensional, grass-like film. These films have been prepared before by sol-gel and anodic methods for antireflection applications, but a conversion of ALD Al_2O_3 to grass-like alumina has been published as well. The causes of the formation of this grass have been conjectured, but no definitive conclusions have been reached.

Metal-organic frameworks are three dimensional frameworks made of metal-containing units held together by organic linker molecules. MOFs are usually synthesized in the bulk form, but thin film structures enable new features as well as enhance a multitude of MOF key abilities. ZIF-8 and UiO-66 are examples of these kinds of MOFs. The synthesis of MOF thin films is challenging overall because the growth of this crystalline material needs to be promoted on a support.

A vast majority of ZIF-8 preparation methods are solution-based, but recently films have been prepared through vapor phase-based techniques. These methods generally involve a few steps, and one of them comprises of converting an ALD ZnO thin film into ZIF-8 by delivering 2-methylimidazole vapor on the film. This three-step method produces films with excellent conformality on challenging surfaces. The optimization of the conversion and capabilities of the film have yet to be explored.

UiO-66 is typically prepared through draining solvothermal processes and developed vapor-based methods have long reaction times (24 h). The vapor-based methods consist of gas-phase conversions of zirconium terephthalate hybrid MLD thin films. Direct vapor phase conversion of zirconium oxide ALD films could be a simple and reproducible method for synthesizing UiO-66 films in the future.

Experimental

6 Experimental Methods

6.1 Atomic Layer Deposition

Thin film depositions were done using a F120 ALD reactor (ASM Microchemistry Ltd) and a Beneq TFS 200 ALD reactor. In both reactors, nitrogen gas (AGA, 99.999 %) was used as the inert gas, and the pressure during depositions was 5 - 10 mbar. The films were deposited on 5x5 cm^2 Si(100) substrates in the F120 reactor and on 200 mm Si(100) and Si(111) wafers in the TFS200 reactor without the removal of the native oxide. Before use, the substrates were blown with compressed nitrogen and the native oxide remained.

6.2 Film Characterization

Film thicknesses were determined using a Film Sense FS-1 Multi-Wavelength ellipsometer and X-ray reflectivity (XRR, PANalytical X'Pert Pro MPD). Crystal structure was determined by grazing incidence X-ray diffraction (GIXRD) using a Rigaku SmartLab X-ray diffractometer (incident angle of CuK_α, wavelength 1.54 Å, radiation 1°). High temperature X-ray diffraction (HTXRD) measurements were conducted on approximately 1.5x1.5 cm^2 samples in an Anton-Paar HTK1200N oven connected to the PANalytical X'Pert Pro MPD X-ray diffractometer. For non-ambient measurements, the chamber was filled with O_2 (AGA, 99.999 %) or N_2 (AGA, 99.999 %) gas up to atmospheric pressure. All XRR and XRD data was analyzed with PANalytical Highscore Plus 4.1 and PANalytical X'Pert Reflectivity 1.2a software.

The ZIF-8 to ZnO phase ratios were determined from the XRD data by Rietveld refinement using MAUD software.[214] For some of the conversions of ZnO films grown on a TiO_2 film, the TiO_2 phase was visible in the diffractograms. In these cases, the ZIF-8/ZnO ratios were determined by subtracting the TiO_2 phase and calculating the ratio manually.

Film morphology and conformality were examined by a Hitachi S-4800 field emission scanning electron microscope (FESEM). Before imaging, 4 nm of Au/Pd was sputtered onto the samples to improve the image quality. Thermogravimetric analyses (TGA) were conducted with a Mettler Toledo Star^e system equipped with a TGA 850 thermobalance using a heating rate of 10 °C/min in air and N_2 at 1 atm. The weights of the samples were approximately 10 mg.

6.3 Conversion Reactors

All thin film materials for the conversions were grown on Si. Two custom-made reactors were used for the conversions. These reactors are described below. Some of the experiments were done in an autoclave (Parr 4744).

Conversion Reactor Z (Figure 33) consists of two glass vials, A and B, followed by a removable connection to a rotary vane vacuum pump. There are hand valves between Vials A and B as well as between Vial B and the outlet. Experiments in Reactor Z were conducted by placing the precursor in Vial A and the substrates (ALD thin films) in vial B. The substrates were cut to pieces of approximately 20x50 mm in order to fit in Vial B. Air was pumped out from both Vials A and B independently with the vacuum pump before the experiments. If elevated temperatures were required for the experiment, the reactor was placed inside an oven after both vials had been evacuated. The experiments were conducted only after the system had reached the target temperature.

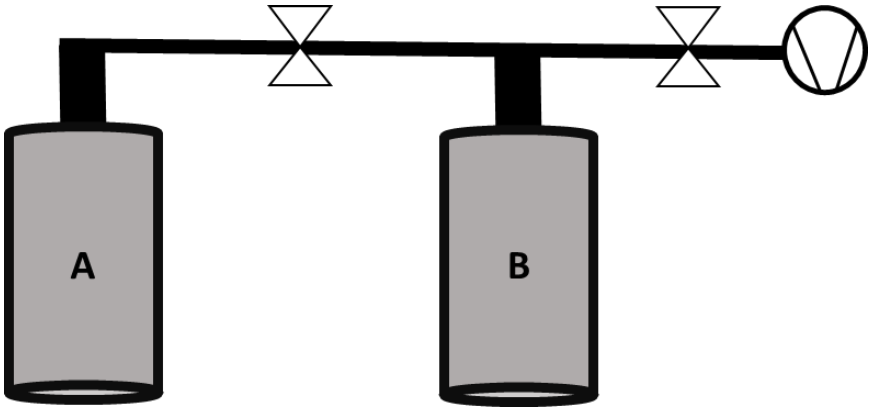

Figure 33. An illustration of Conversion Reactor Z.

Conversion Reactor Y (Figure 34) consists of two hollow stainless steel vessels, followed by an Inficon VGC402 pressure gauge and a connection to a rotary vane vacuum pump. The outer diameter of the vessel is 69 mm and the diameter for the indentations inside is 49 mm. Hand valves are placed between Vessels A and B, between Vessel B and the pressure gauge, and between the pressure gauge and the vacuum pump. A hand valve also exists between the system and the pressure gauge.

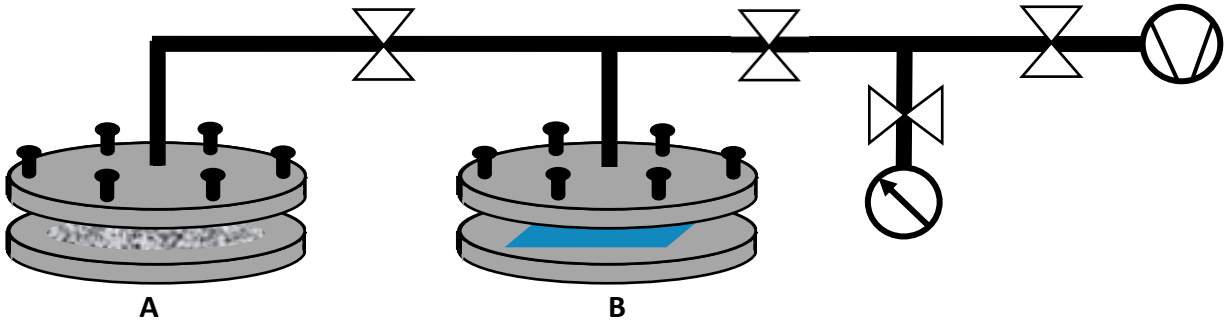

Figure 34. An illustration of Conversion Reactor Y.

For conversions, the solid precursor was placed in an aluminum foil boat inside Vessel A and two thin film samples were placed inside Vessel B (Figure 35). The films to be converted were placed on top of each other inside Vessel B, so that the bottom film was facing downwards and the top film upwards. A second indentation in Vessel B allowed for a gap between the bottom film and the vessel base. The vessel lids were tightened in place with bolts and copper gaskets sealed the pieces together. For reactions requiring both a liquid and solid precursor, the reactor was modified so that the pressure gauge was substituted by a glass vessel containing the liquid precursor.

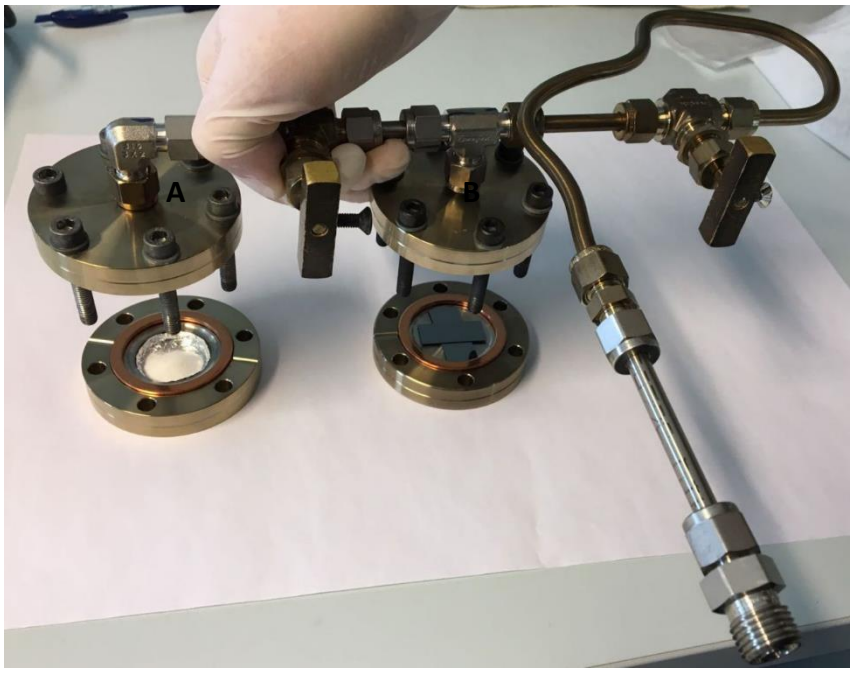

Figure 35. A photograph of Conversion Reactor Y with a solid precursor in Vessel A and two thin film samples is Vessel B.

The system was pumped down to a base pressure before experiments. Contact between precursors and substrates during pumpdown was avoided. The base pressure inside the vessels was approximately 0.1-0.3 mbar after pumpdown. Vessels A and B were placed inside an oven if temperatures above room temperature were required. The liquid precursors in Conversion Reactor Y were not heated.

7 Conversion Reactions

7.1 Ruthenium

In this section, the conversion of metallic Ru thin films into crystalline RuO_2 under ambient and O_2 atmospheres is studied. The objective is to get smooth and conformal films with a simple, one-step conversion.

First, metallic Ru thin films were deposited with ALD on Si. A 20 nm layer of Al_2O_3 was deposited on Si before the metallic ruthenium film with $AlCl_3$ and H_2O as precursors. The pulsing sequence consisted of 1 s pulses and purges for both precursors. The role of the Al_2O_3 layer was to aid Ru nucleation and obtain uniform films. Ruthenium thin films were subsequently deposited on Al_2O_3 films with $RuCp_2$ and O_2 as precursors. The deposition sequence consisted of a 2 s pulse of $RuCp_2$ followed by a 1 s purge, and a 1 s pulse of O_2 followed by a 1 s purge. Both films were grown successively at a deposition temperature of 300 °C.

Nucleation of the Ru ALD films seems to start slowly, and a clear nucleation delay of approximately 200 cycles is evident (Figure 36). A GPC of 0.43 Å/cycle was attained after the delay. XRD measurements confirmed the films to be hexagonal ruthenium (Figure 37), though peaks for the thinnest film were very small. The roughnesses of the resulting films were 2.4, 2.2 and 2.6 nm for 46, 20 and 3.4 nm thick Ru films, respectively. SEM images (Figure 38) indicate that the Ru films are indeed quite rough for ALD Ru films.

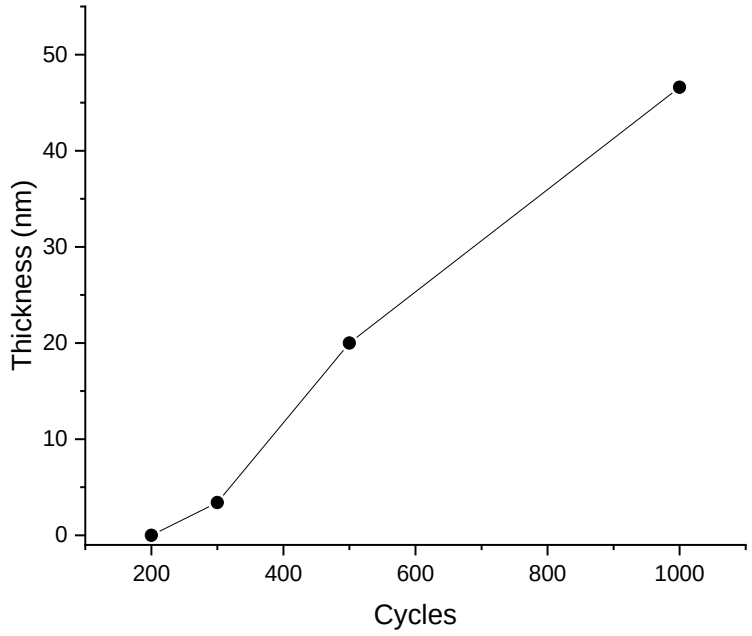

Figure 36. Film thickness as a function of cycle count for Ru films deposited on Al_2O_3 at 300 °C.

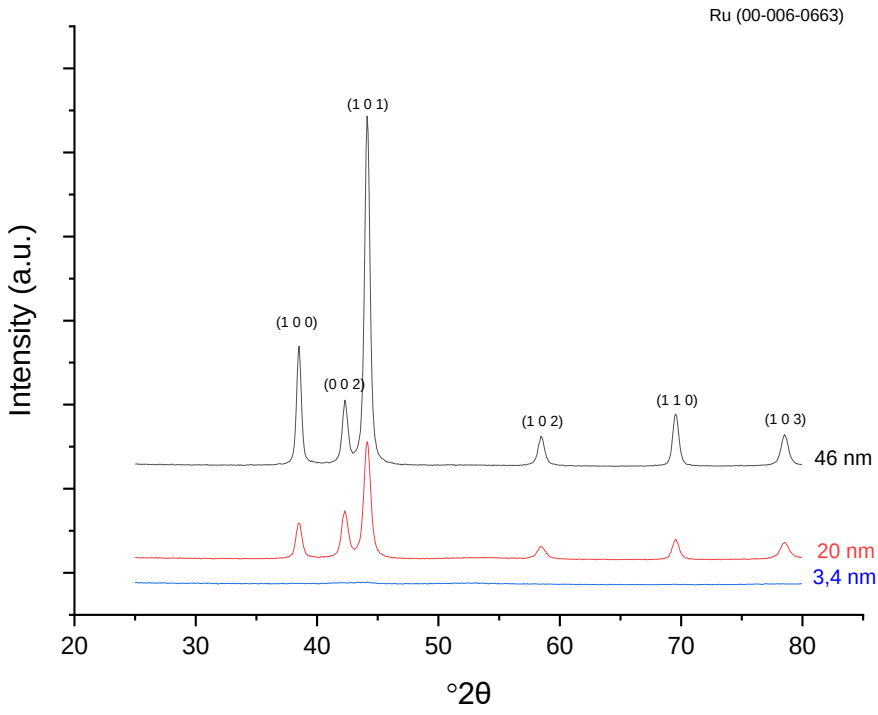

Figure 37. X-ray diffractogram of Ru films with various thicknesses deposited on Al_2O_3 at 300 °C.

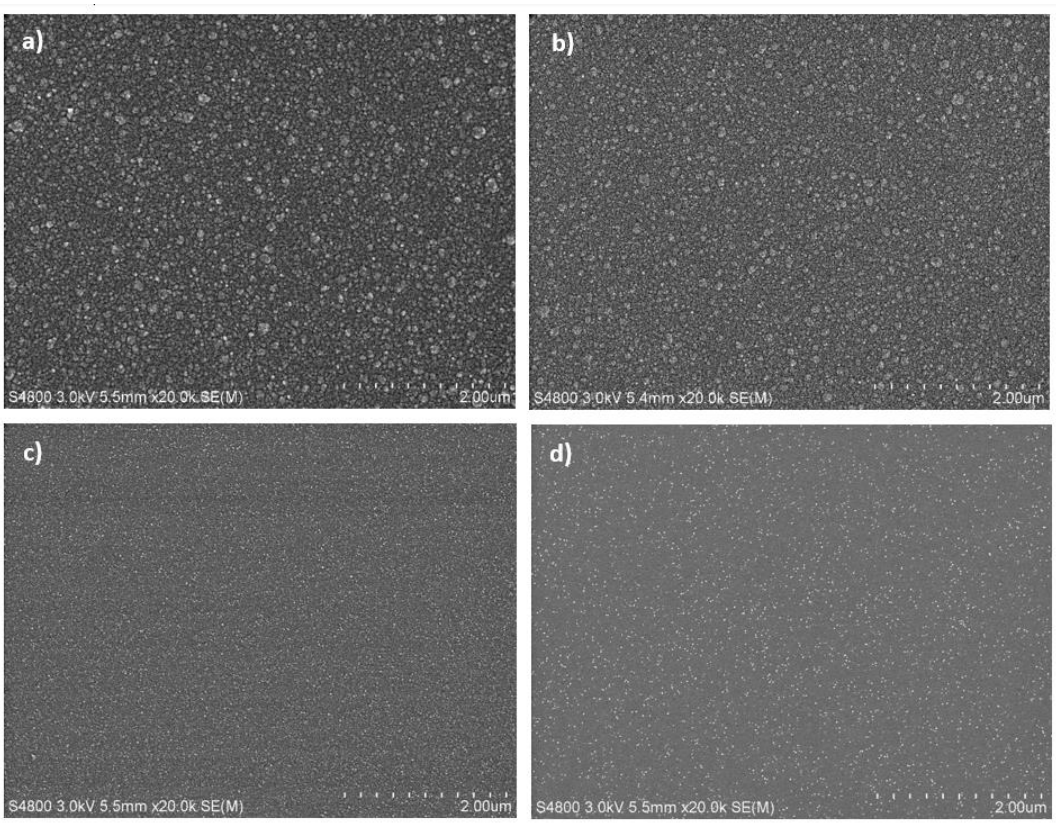

Figure 38. Plan-view SEM images of Ru thin films deposited on Al_2O_3 at 300 °C. Thicknesses of the films were determined as a) 46, b) 20, c) 3.4, and d) <1 nm.

All the HTXRD measurements were conducted under O_2 and ambient air conditions. In the figures (Figure 39), the grayscale background represents the overall HTXRD measurement. The dark lines correspond to peaks that emerged during the measurements. Their darkness scales with the intensity of the peaks attained during the measurement at various temperatures. The coloured diffractograms labelled with a temperature have been chosen as examples from all the measurement points to represent the state of the films at the corresponding temperatures.

Films with Ru thicknesses of 46, 20, and 3.4 nm were heated under ambient air and O_2 atmospheres up to 745-1000 °C to convert them into RuO_2. The thickest 46 nm film seems to fully convert to RuO_2 at around 650 °C under ambient air and 600 °C under O_2 (Figure 39). The RuO_2 film seems to disappear at 700 °C under O_2, which suggests it has converted into the volatile RuO_4 that evaporates away from the substrate.

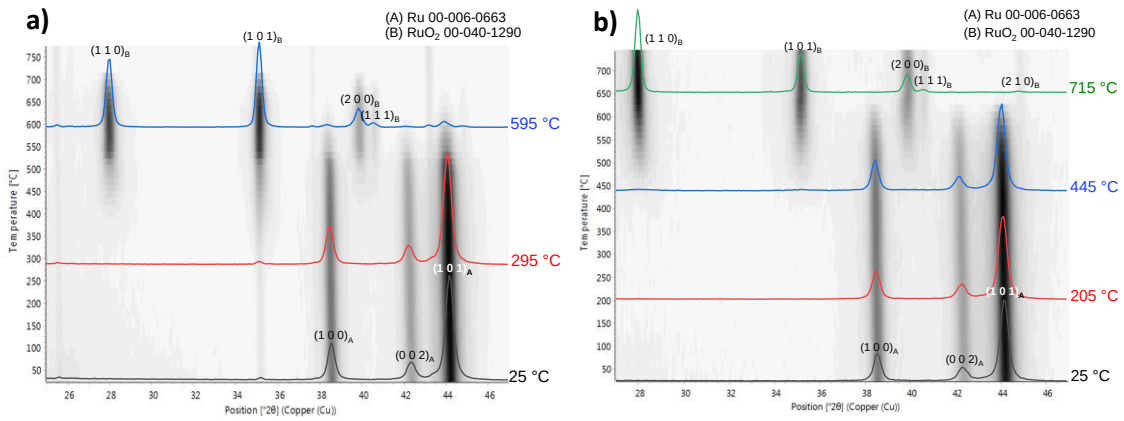

Figure 39. HTXRD measurement under ambient air (a) and O_2 (b) of a 46 nm Ru thin film grown on Al_2O_3 at 300 °C. The peaks passing through the entire temperature spectrum at approximately 25, 35, 37, and 43 degrees correspond to corundum Al_2O_3, which is an impurity arising from the measurement setup (b).

The 20 nm film seems to fully convert to RuO_2 at around 600 °C under ambient air and 550 °C under O_2 (Figure 40). The lower conversion temperature can be expected since the thickness is less than half ofthe thicker film. Additionally, the film evaporates at 800 and 675 °C under ambient air and O_2, respectively. This again suggests that the conversion to RuO_4 has occurred at those temperatures. The thinnest film of 3.6 nm shows only one broad Ru peak at the beginning of the measurement (Figure 41). The lack of peak intensities is attributed to the thinness of the film. Even so, RuO_2 peaks appear at 450 °C, indicating a conversion to have taken place. Conversion to RuO_4 seems to occur already at approximately 575 °C.

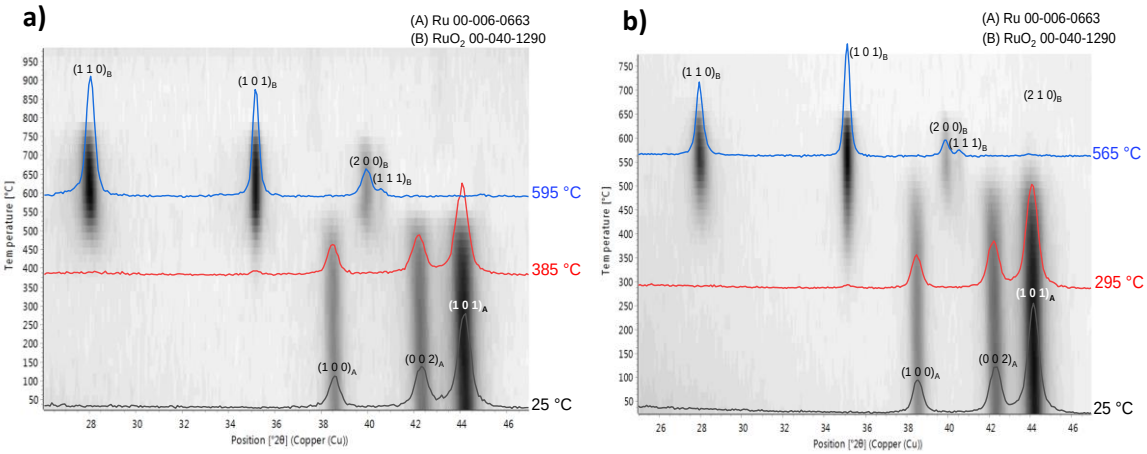

Figure 40. HTXRD measurement under ambient air (a) and O_2 (b) of a 20 nm Ru thin film grown on Al_2O_3 at 300 °C.

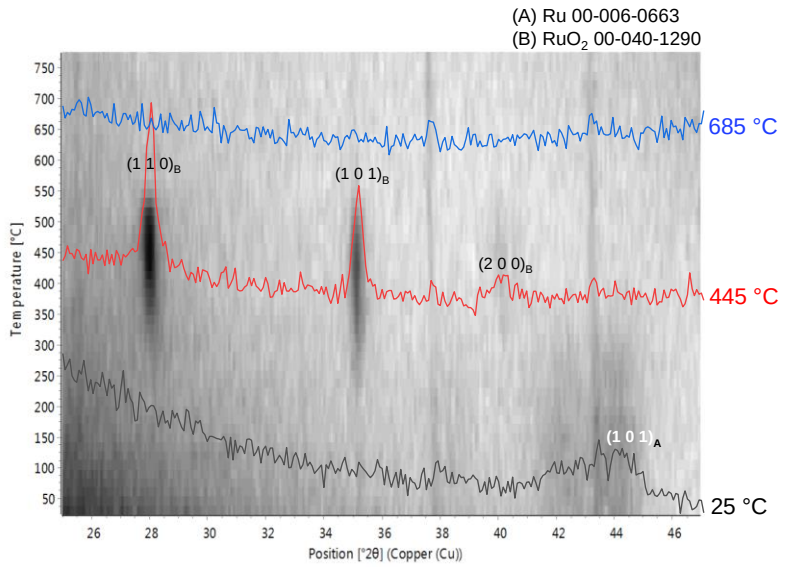

Figure 41. HTXRD measurement under O_2 atmosphere of a 3,6 nm Ru thin film grown on Al_2O_3 at 300 °C. The peaks passing through the entire temperature spectrum at approximately 25, 35, 37, and 43 degrees correspond to corundum Al_2O_3, which is an impurity arising from the measurement setup.

7.2 Rhenium and Rhenium Nitride

The goal of this part of the workwas to obtain continuous ReO_3 directly from Re and ReN_x thin films through a facile conversion reaction. Rhenium and rhenium nitride thin films were deposited on 10 nm thick ALD Al_2O_3 on a Si substrate by Jani Hämäläinen as described in further detail in the corresponding article[93]. Both Re and ReN_x films were grown with $ReCl_5$ and NH_3 as precursors at 375 (ReN_x) and 400 °C (Re). The underlying Al_2O_3 films were grown with $AlCl_3$ and H_2O as precursors. Film thicknesses are about 22 nm for Re and and 31 nm for ReN_x.

A newly grown Re film was heated up to 750°C in a N_2 atmosphere. HTXRD measurements (Figure 42) reveal that no changes in the film happen. This means that Re should not react to heat up until 750 °C.

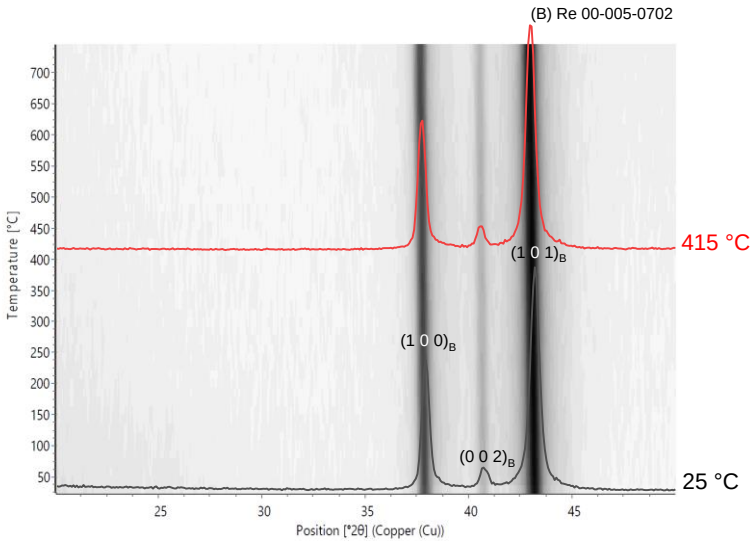

Figure 42. HTXRD measurement under a N_2 atmosphere of a 22 nm Re film grown at 400 °C on Al_2O_3.

It had been previously noted that Re and ReN_x films undergo some type of reaction when stored under ambient air. Therefore, the newly grown Re film was heated under ambient air up to 700 °C in the HTXRD setup (Figure 43). It can clearly be seen that the film amorphized or evaporated after 300 °C. As stated in section 4.1.1, Re_2O_7 sublimes at around 300°C. The oxide formed here might instead of ReO_3 be Re_2O_7, which directly sublimes off the substrate without leaving evidence. There was no film left on the substrate after the measurement.

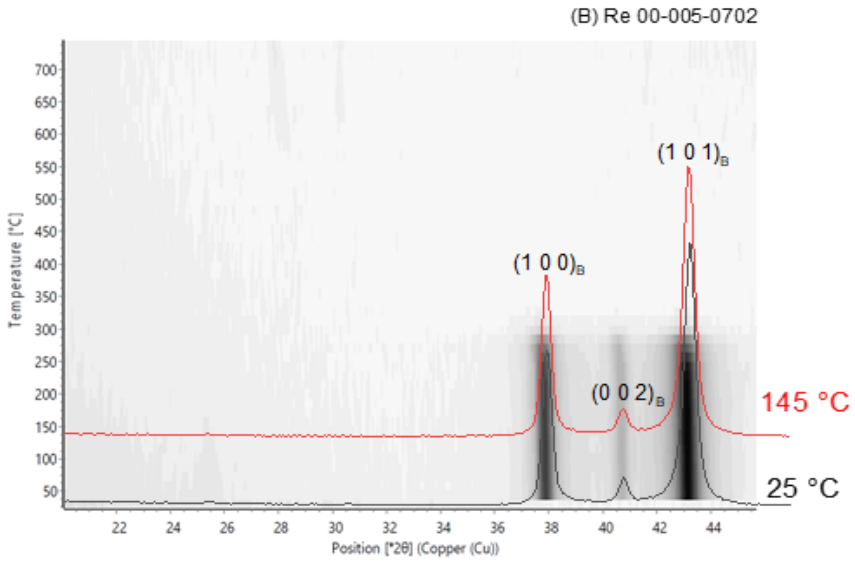

Figure 43. HTXRD measurement under ambient air of a 22 nm Re film grown at 400 °C on Al_2O_3.

The Re film was also treated under an O_3 environment for 1 h at both room temperature and 100 °C. The film exhibited very little change in morphology after the room temperature treatment (Figure 44b) as compared to the original film (Figure 44a). Conversely, SEM images after the treatment at 100 °C (Figure 44c) show that the film continuity had clearly suffered, and large crystals had formed. Both films revealed small ReO_3 peaks in their XRD diffractograms (Figure 45). The crystals formed on the films are most likely ReO_3 crystals, which would explain the peaks observed in the XRD measurements. The low intensities of the ReO_3 peaks after the 100 °C treatment can be explained by the low number of crystals and the crystals being more oriented because of the way they have grown on the film.

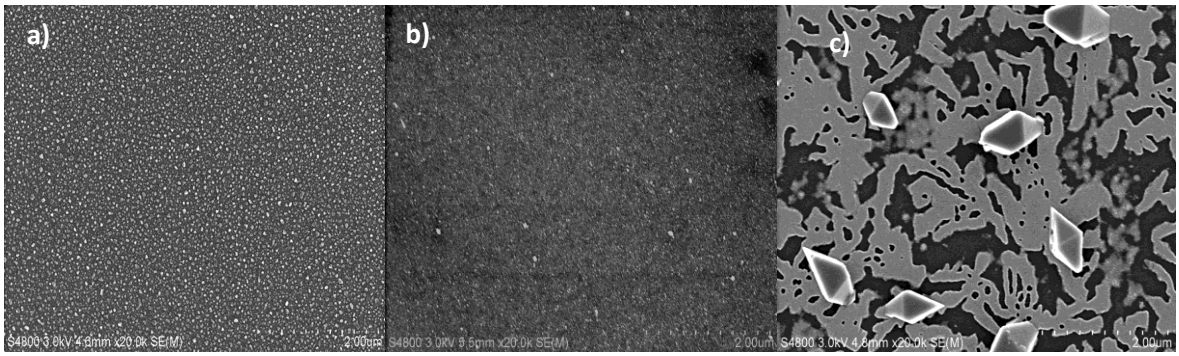

Figure 44. SEM images of a 22 nm Re film grown on Al_2O_3 at 400 °C (a) after a treatment under ozone at room temperature (b) and 100 °C (c) for 1 h.

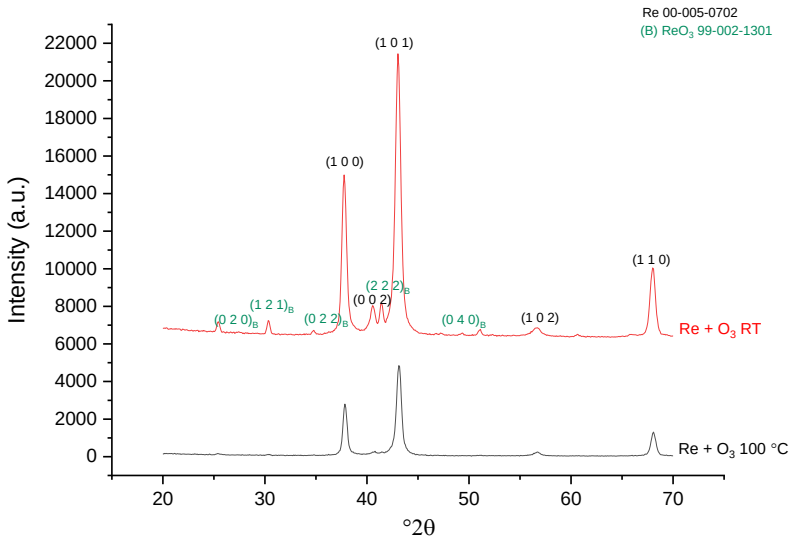

Figure 45. X-ray diffractograms of a 22 nm Re film grown on Al_2O_3 at 400 °C after a treatment under ozone at room temperature (top) and 100 °C (bottom) for 1 h.

The same treatments under ozone were repeated on a 31 nm ReN_x film grown at 375 °C. At room temperature, the ReN_x film cracked only from where crystals began to grow (Figure 46a) while holes in the film are present throughout the whole film after the ozone treatment at 100 °C (Figure 46b,c). Again, XRD showed small ReO_3 peaks for both films.

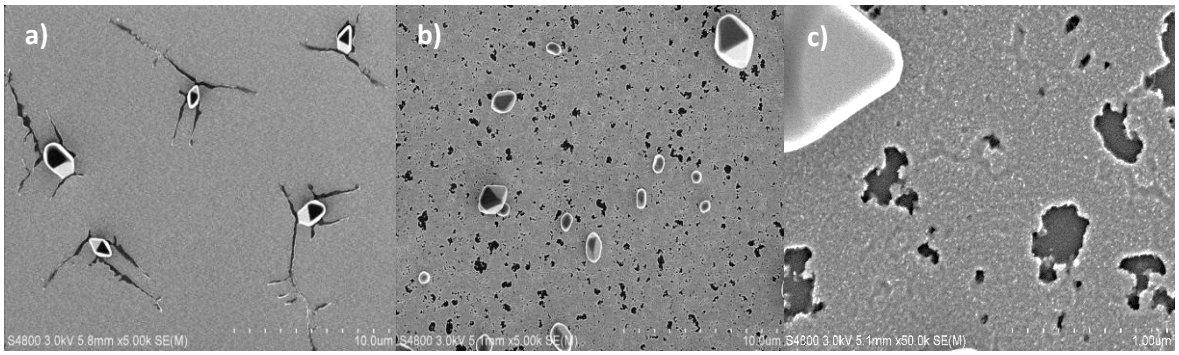

Figure 46. SEM image of a 31 nm ReN_x film grown at 375 °C on Al_2O_3 after a treatment under ozone at room temperature (a) and 100 °C (b,c) for 1 h.

To see the effects of humidity on the Re thin films, a 22 nm Re film was placed under a relative humidity of 94-98 % at room temperature. After 24 h no change was visually observed, so the film was taken out only after 7 days. SEM images of the film before and after this treatment (Figure 47 a and b) showed that relatively large crystals had formed on the film and the film continuity had deteriorated much like the Re films treated under ozone. The XRD diffractogram again displayed low intensity ReO_3 peaks.

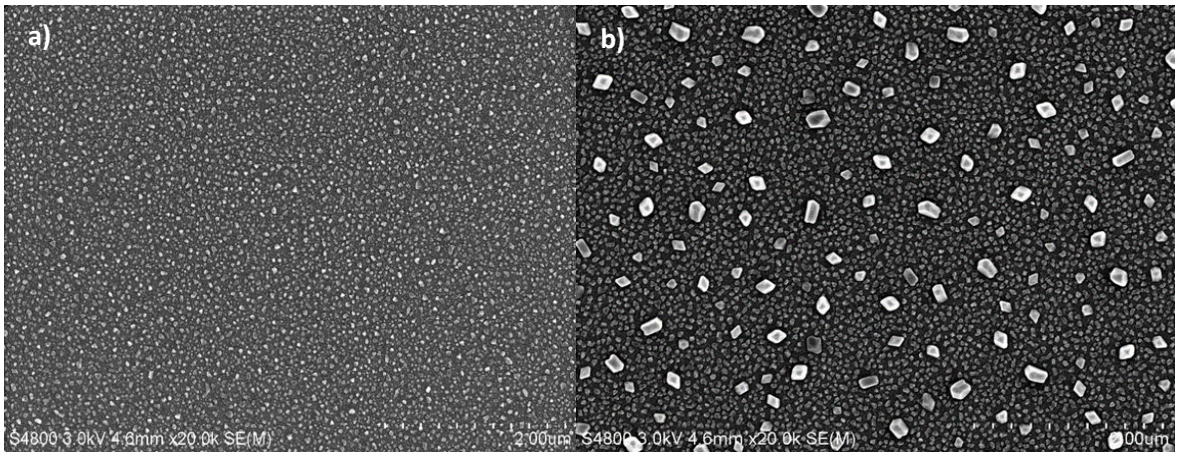

Figure 47. SEM image of a 22 nm Re film grown at 400 °C on Al_2O_3 before (a) and after (b) treatment under 94-98 % relative humidity at room temperature for 7 days.

The 24 nm ReN_x film on Al_2O_3 was coated with a 10 nm layer of Al_2O_3 in an attempt to prevent any evaporation of the film under the HTXRD examination. The film was heated up to 600-625 °C under ambient air (Figure 48a) and O_2 (Figure 48b). The ReN_x film thermally decomposes to form hexagonal Re. In both atmospheres, the film converts to hexagonal Re around 475 °C. Clearly, the Al_2O_3 film protects the ReN_x film from oxygen and prevents the reaction to form volatile rhenium oxides (c.f. Figure 43).

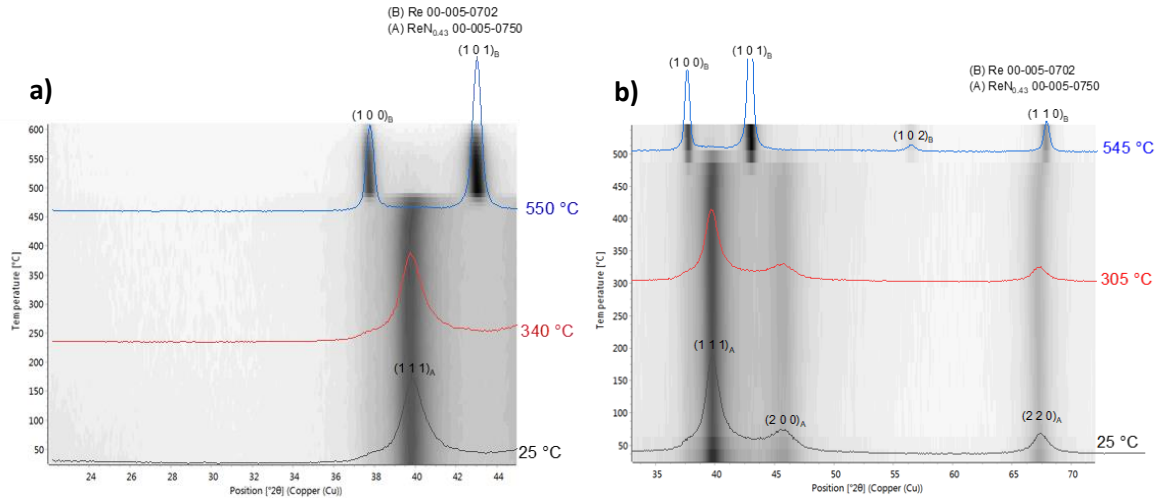

Figure 48. HTXRD measurement under ambient air (a) and O_2 (b) of a 24 nm ReN_x film grown at 400 °C and capped with a 10 nm Al_2O_3 layer.

7.3 UiO-66

In this section, the conversion of zirconium oxide ALD thin films to UiO-66 through a single-step reaction with terephthalic acid (TPA) and acetic acid is examined. The effect of the original film crystallinity to the conversion was also to be examined. Unless stated otherwise, the conversions were carried out in Conversion Reactor Y.

Thermogravimetric analysis revealed that TPA starts to vaporize at around 250 °C and has evaporated completely by 350 °C (Figure 49). Consequently, the conversions were carried out at 250°C and 300°C.

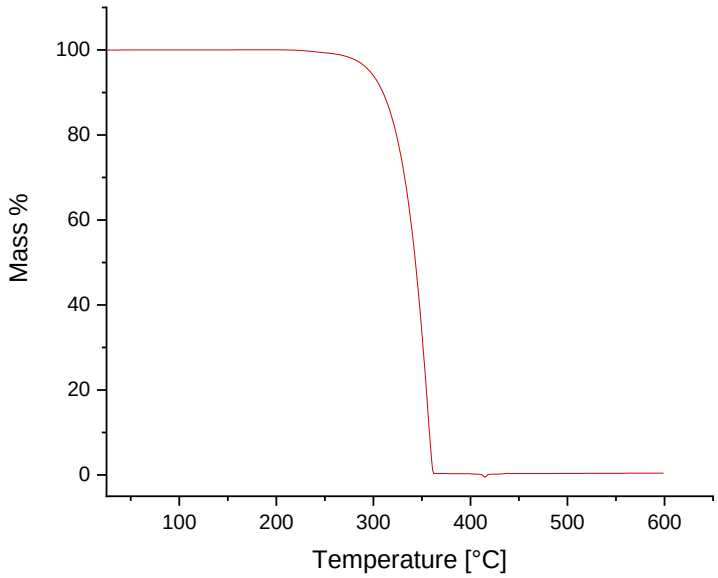

Figure 49. Thermogravimetric analysis of terephthalic acid.

Weakly crystalline ZrO_2 films grown with Zr(Cp)(^{t}BuDAD)(O^{i}Pr) and O_3 as well as Zr(Me_5Cp)(TEA) and O_3 as precursors, as in in the work of Seppälä[215], with thicknesses ranging from 6 to 60 nm, were placed under TPA vapor. The conversion times ranged from 1 to 18 h and temperatures from 250 to 300 °C. No change was observed in any of the films.

Previous studies have confirmed acetic acid to aid the reaction. For example, Lausund and Nielsen[43] found that introducing acetic acid to their vapor phase UiO-66 process steered the bonding scheme from mono- to bidentate and treatment under acetic acid vapor

crystallized amorphous UiO-66 films. Crystalline, weakly crystalline (16-40 nm), and amorphous (50-64 nm) ZrO_2 thin films were placed in the conversion reactor with TPA and acetic acid. The reactions took place at 300 °C for 4-68 h. Both the crystalline and weakly crystalline ZrO_2 films were grown with $Zr(Me_5Cp)(TEA)$ or $Zr(Cp)(^tBuDAD)(O^iPr)$ and O_3 as precursors at 250, 350, or 400 °C [215]. The amorphous ZrO_2 films were grown with ZrMeCp(TMEA) and O_3 as precursors at 200 and 250 °C[215]. Only the amorphous ZrO_2 films exhibited visual changes after 7 h (Figure 50). Consequently, a 64 nm amorphous ZrO_2 film was exposed to TPA and acetic acid at 250 °C for 68 h (Figure 50). The resulting film appeared visually much darker and matte than the original ZrO_2 film, but XRD measurements revealed the film to have remained amorphous. SEM images revealed bubble-like disturbances in the morphology (Figure 51). A 51 nm amorphous ZrO_2 film exposed to TPA and acetic acid at 250 °C for 68 h demonstrated similar mattifying without a change in crystallinity. The attempted conversion reaction of ZrO_2 to UiO-66 can be written as:

$$6ZrO_2 + 6H_2BDC(g) \longrightarrow Zr_6O_4(OH)_4(BDC)_3 + 4H_2O(g)$$

The bubbles on the mattified amorphous ZrO_2 might have formed due to $H_2O(g)$ trying to escape from the film, indicating that a reaction of some degree had occurred. Crystallization of both mattified films was attempted in an autoclave with ~0,1 ml of acetic acid at 160 °C for 24 h, but no change in crystallinity was achieved. Lausund and Nielsen crystallized amorphous UiO-66 with a similar treatment.[43] Additionally, amorphous ZrO_2 grown with $Zr(Me_5Cp)(TEA)$ and O_3 as precursors at 250 °C, with thicknesses of 7 and 17 nm, were placed into an autoclave with 0,5 ml THF and 2,5 ml acetic acid in DMF. The autoclave was sealed for 4 h at 250 °C. There was no change in the visual appearance of the film, and XRD measurements showed no change in crystallinity.

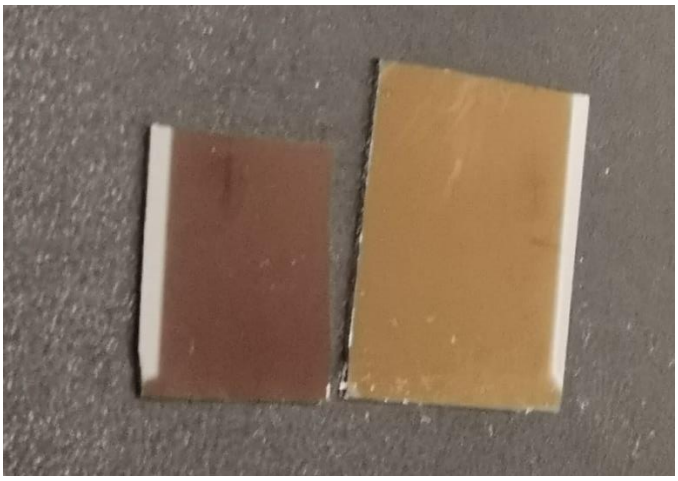

Figure 50. A 64 nm amorphous ZrO_2 film exposed to TPA and acetic acid at 250 °C for 68 h (left) and the same film exposed to TPA and acetic acid at 300 °C for 7 h (right).

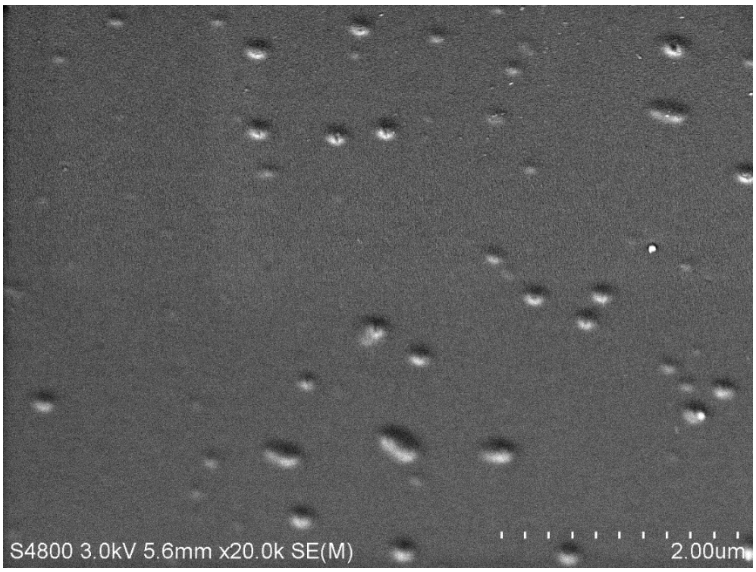

Figure 51. SEM image taken at a 45° angle from a 64 nm amorphous ZrO_2 film exposed to TPA and acetic acid at 250 °C for 68 h.

7.4 ZIF-8

The objective of this work was to fabricate continuous ZIF-8 thin films on Si via one-step conversions of an ALD ZnO thin films under 2-methylimidazole (99.9 %, Sigma-Aldrich) vapor. The experiment setup was designed so that the ZnO film was not in the same vessel as the solid 2-methylimidazole (HmIM).

ZnO thin films were grown on Si at 250 °C with diethylzinc (DEZ) and H_2O as precursors. The sequence for ZnO film growth consisted of 1 s DEZ pulse and 2 s purge, followed by 1.5 s pulse of H_2O and 3 s purge. A layer of either TiO_2 (T-ZnO) or Al_2O_3 (A-ZnO) was deposited at 250 °C before the ZnO film to improve ZIF-8 adhesion and uniformity (Figure 52). Trimethylaluminum and H_2O were used as precursors for the Al_2O_3 films, and the TiO_2 films were grown with titanium tetrachloride and H_2O as precursors.

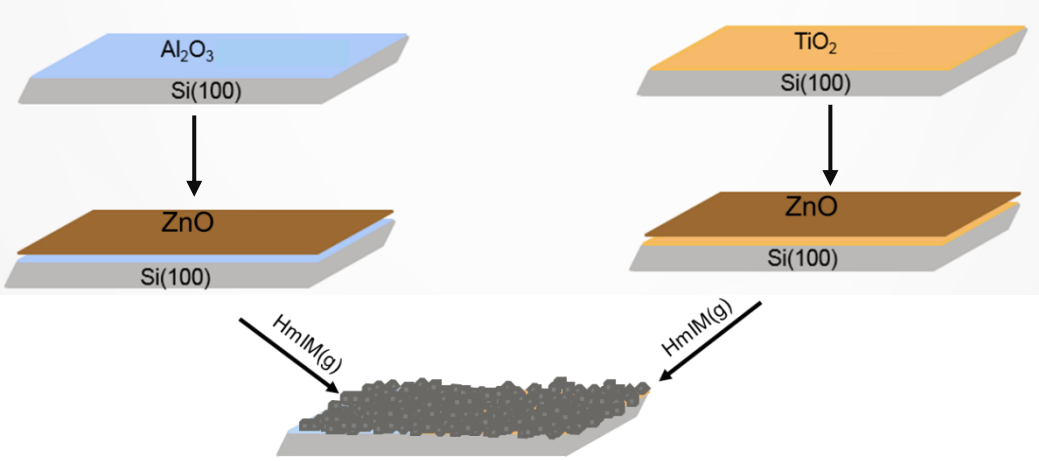

Figure 52. An illustration of the different steps taken for the deposition of ZIF-8 thin films. First, a TiO_2 or Al_2O_3 thin film was grown on a Si(100) substrate. Next, a ZnO thin film was deposited on the TiO_2 and Al_2O_3 films. Finally, the ZnO films were converted to ZIF-8 under HmIM vapor.

The thicknesses of the TiO_2 films were 20 ± 1 nm and 8-20 nm for Al_2O_3. Growth rates of ZnO were found to be 1.1 Å/cycle on Al_2O_3 (Figure 53) and 0,47 Å/cycle on TiO_2 (Figure 53). The thicknesses of ZnO films on Al_2O_3 could not be accurately measured through XRR measurements due to a density profile in the ZnO layer. However, the error is not

significantly large. All conversions to ZIF-8 as the target material were done with Conversion Reactor Y. T-ZnO and A-ZnO films were converted in the same experiment each time to obtain comparable results.

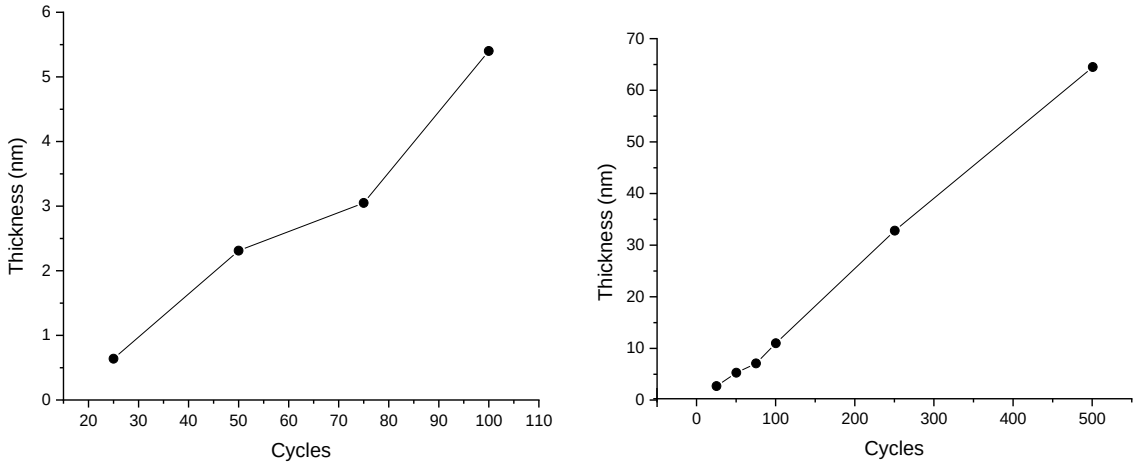

Figure 53. ZnO film thickness as a function of ALD cycles at 250 °C on TiO_2 (left) and Al_2O_3 (right).

The boiling point of HmIM is 270 °C. Thermogravimetric analysis revealed that HmIM starts to vaporize at around 150 °C and has evaporated completely by 210 °C (Figure 54). Consequently, the conversions were carried out at 150 and 200 °C. Conversion reaction times were varied between 30 min and 2 h. Thicknesses of ZnO films before conversion ranged from 2.7 to 65 nm for A-ZnO films and 0.6-5.4 nm for T-ZnO films.

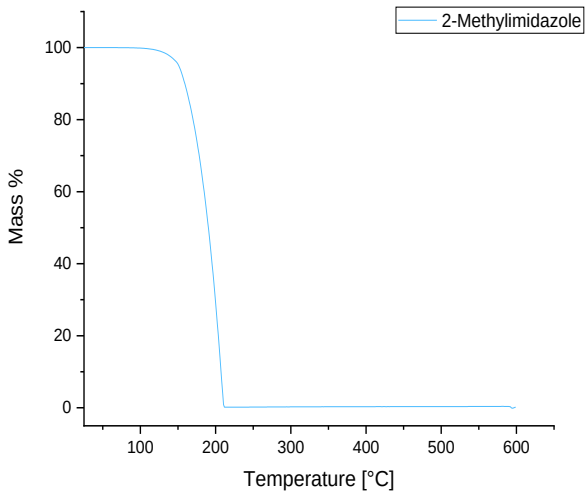

Figure 54. Thermogravimetric analysis of 2-methylimidazole.

Figure 55 shows SEM images of initial T-ZnO (Figure a, thickness 5.4 nm) and A-ZnO (Figure 55 c, thickness 7.1 nm) films together with the same films after the conversion at 200 °C for 30 min (Figure 55 b and d). In both films, an evident and similar change in morphology to the ZIF-8 structure can be observed. The resulting ZIF-8 thin film on the Al_2O_3 adhesion layer appears to have a more uniform morphology than the ZIF-8 on TiO_2. As estimated from ZnO and ZIF-8 peak ratios in XRD using Rietveld refinement, the T-ZnO film has undergone a 88 % and the A-ZnO film a 91 % conversion to ZIF-8. Visually, the ZnO films transform from mirror-finish coatings to matte ZIF-8 (Figure 56).

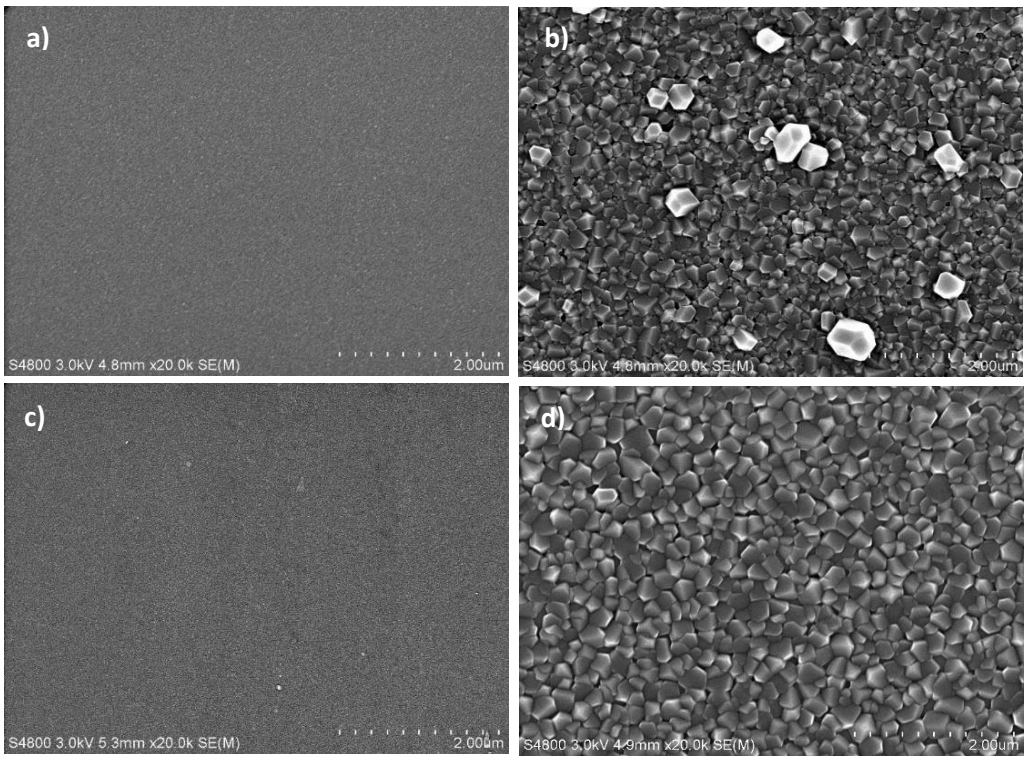

Figure 55. Top-down SEM images of ZnO thin films deposited on a) TiO_2 and c) Al_2O_3 followed by conversion to ZIF-8 at 200 °C for 30 min (images b) and d), respectively). Image a) ZnO film thickness 5.4 nm and c) 7.1 nm.

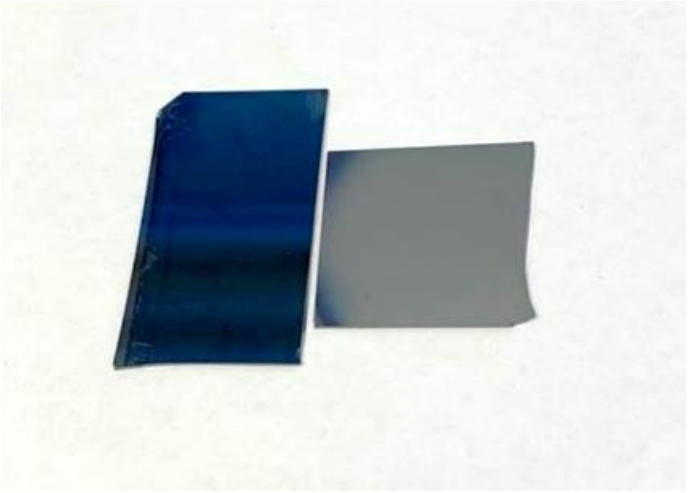

Figure 56. A photograph of a 33 nm A-ZnO thin film before (left) and after (right) conversion to ZIF-8 at 200 °C for 2 h.

Full conversion of ZnO to ZIF-8 on Al_2O_3 and TiO_2 was achieved after 2 h at 200 °C, as evaluated from the ZnO and ZIF-8 peak ratios in XRD using Rietveld refinement (Figure 57). Conversion of A-ZnO to ZIF-8 after 2 h is at 98 %, but the film has most likely converted fully. Due to the nature of the Rietveld refinement, extremely small ZnO XRD peaks cannot be fitted accurately. The shortest reaction time, 30 min, led to roughly 90 % conversions at 200 °C. The initial film thicknesses for T-ZnO and A-ZnO were 3.1 and 7.1 nm, respectively.

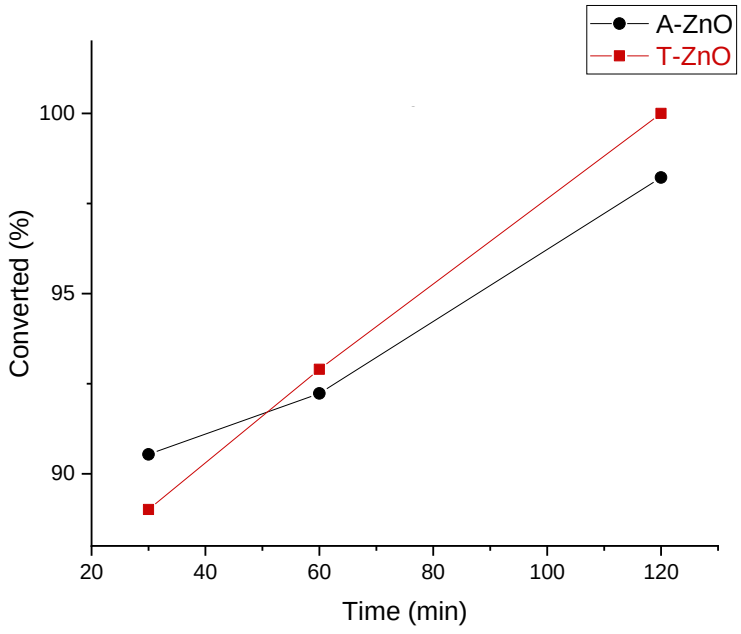

Figure 57. Proportion of ZnO converted to ZIF-8 with HmIM at 200°C as a function of time as analysed by Rietveld refinement of the XRD diffractograms. The error of the Rietveld refinement was approximated as 4%.

When evaluating the effect of the initial ZnO film thickness to the advancement of the conversion reaction, a clear trend can be seen. Diffractograms of A-ZnO films with various initial thicknesses subjected to the ZIF-8 conversion for 30 minutes at 200 °C show a clear decrease of ZnO peaks the thinner the initial film is (Figure 58). Rietveld analyses from these diffractograms indicate the conversion reaction to progress in a linear manner at later stages (Figure 59). These Rietveld analyses agree with the ones shown in Figure 57 for varying the reaction time for both A-ZnO and T-ZnO films. By extrapolating from these graphs, the reaction appears to progress at a faster rate during the initial stages of the conversion. The conversion percentage of the film with an initial ZnO thickness of 11 nm in Figure 59 deviated somewhat from the trend of the other samples for unknown reasons. Nevertheless, a clear linear conversion trend can be seen. This trend concurs with the observations made by Holopainen at al.[52] who discovered that the conversion reaction begins from the top of the ZnO film and advances towards the bottom.

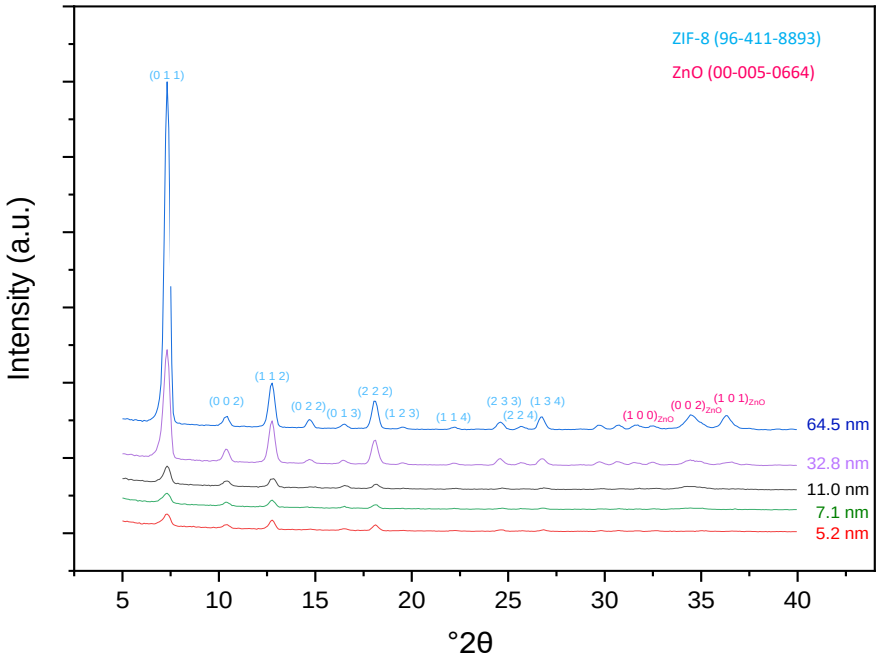

Figure 58. XRD diffractograms of A-ZnO films of various thicknesses converted to ZIF-8 at 200 °C for 30 minutes.

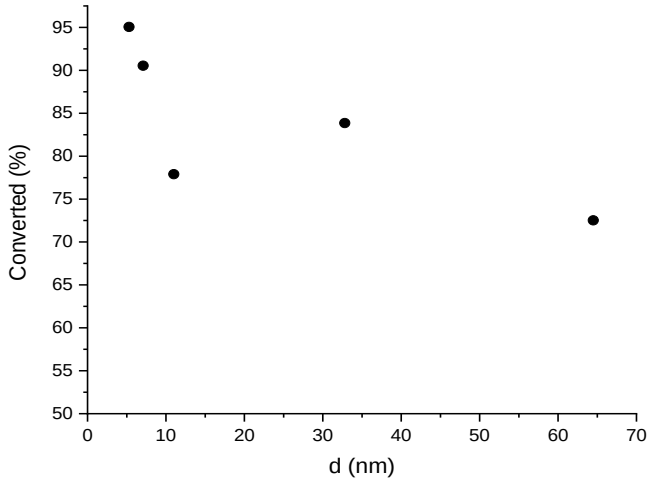

Figure 59. Proportion of A-ZnO film converted to ZIF-8 as a function of initial ZnO thickness after conversion for 30 minutes at 200 °C.

SEM images of some of the ZIF-8 films resulting from the conversions are presented in Figure 60 and indicate that the ZIF-8 crystals coalesce and start to grow larger at arbitrary sites when the conversion progresses and available space on the substrate runs out. The initial ZnO film thickness does not appear to affect the crystal size at equal reaction times.

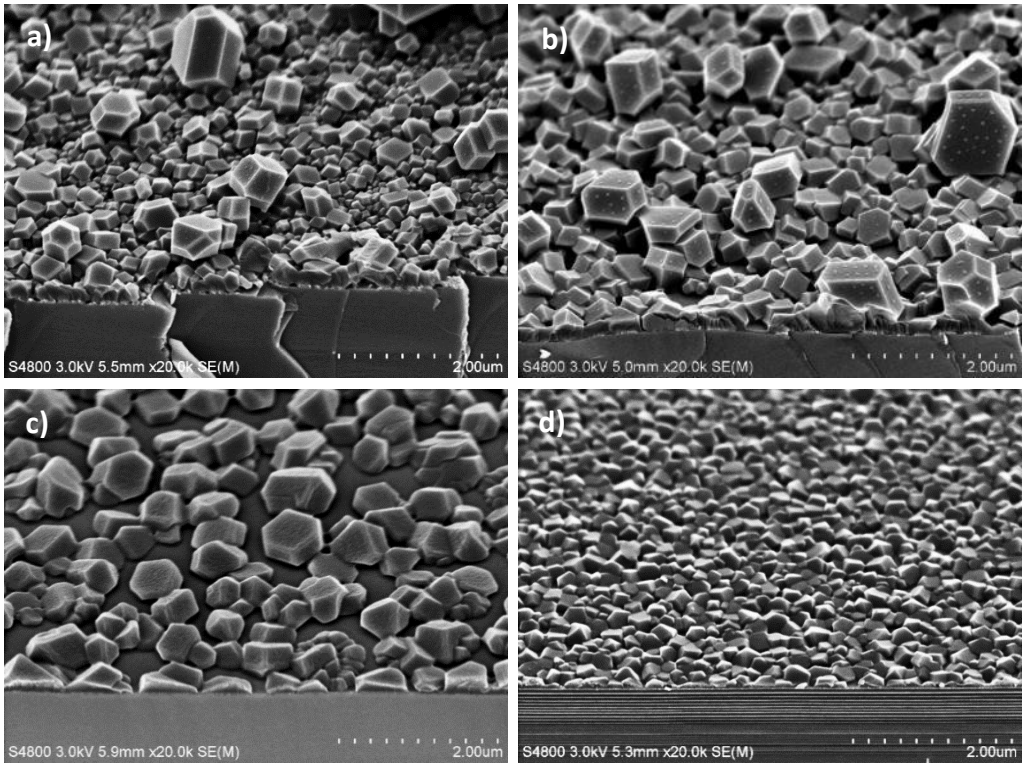

Figure 60. SEM images taken at 45° from A-ZnO films with thicknesses of a) 65, b) 33, c) 11 and d) 7.1 nm converted to ZIF-8 at 200 °C for 30 minutes.

Conversion reaction experiments were also conducted at 150 °C for 30 min for ZnO on Al_2O_3. This resulted in 23 % and 32 % conversions with the initial A-ZnO thickness of 65 and 33 nm, respectively. Compared to 200 °C, the conversions at 150 °C advance slower (Figure 61). The thicker ZnO film was twice the thickness of the thinner film, yet the proportion of the converted film is not double for the thinner film. This supports the interpretation of the reaction not progressing in a linear manner during the initial stages.

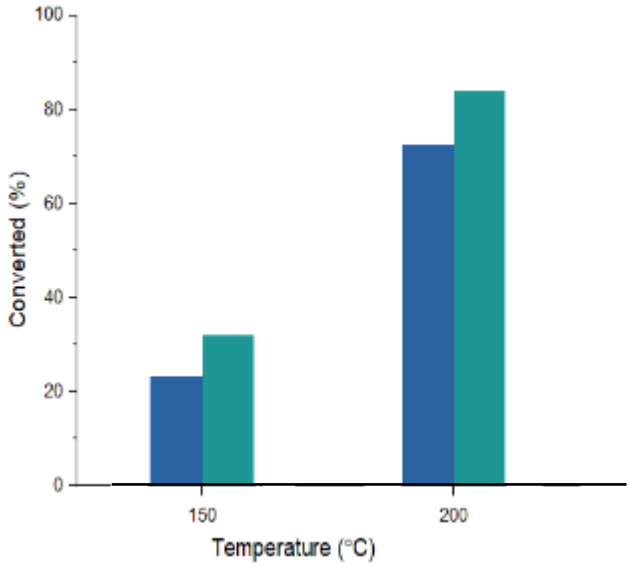

Figure 61. Comparisons of portions of A-ZnO with initial thicknesses of 65 nm (green) and 33 nm (blue) converted to ZIF-8 at 150 °C and 200 °C for 30 min.

The morphologies of the films converted at 150 °C (Figure 62) are significantly more uniform than those of the same A-ZnO films converted at 200 °C for 30 min (Figure 60). Comparing the conversions at 200 and 150 °C, it further seems that the ZIF-8 crystals form with uniform size at the beginning of the conversion and then coalesce to larger crystals. This is in agreement with Stassen's et al. observations on longer reaction times leading to ZIF-8 crystal ripening.[177] The uniformity of the crystal size after the 150 °C conversion could also be a consequence of a smaller nucleation density at lower temperatures, resulting in more space to grow per crystal.

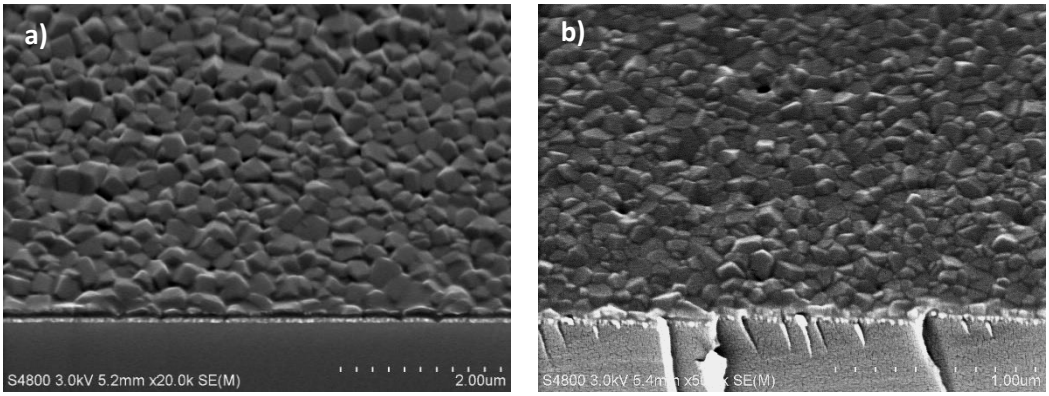

Figure 62. SEM images taken at 45°of A-ZnO films with initial thicknesses of a) 65 and b) 33 nm converted to ZIF-8 at 150 °C for 30 min.

Compared with TiO_2, Al_2O_3 seems to be a better adhesion layer for the ZIF-8 growth. Figure 63a and b show SEM images of ZIF-8 films after the conversion at 200 °C for 30 min with a 7.0 nm A-ZnO and a 5.4 nm T-ZnO as the original films. The fractions of converted film for T-ZnO and A-ZnO were 88 % and 91 %, respectively. Figures 63c and d present SEM images of ZIF-8 films after the conversion at 200 °C for 1 h with 7.0 nm A-ZnO and 3.1 nm T-ZnO as the original films. The fractions of converted film in this case for T-ZnO and A-ZnO were 92 % and 93 %, respectively. In both cases, the ZIF-8 on Al_2O_3 appears smoother and more uniform. The initial 3.1 nm T-ZnO film (Figure 63d) appears to be too thin for complete ZIF-8 coverage of the substrate after the conversion. Even so, the ZIF-8 film on Al_2O_3 displays a uniform morphology.

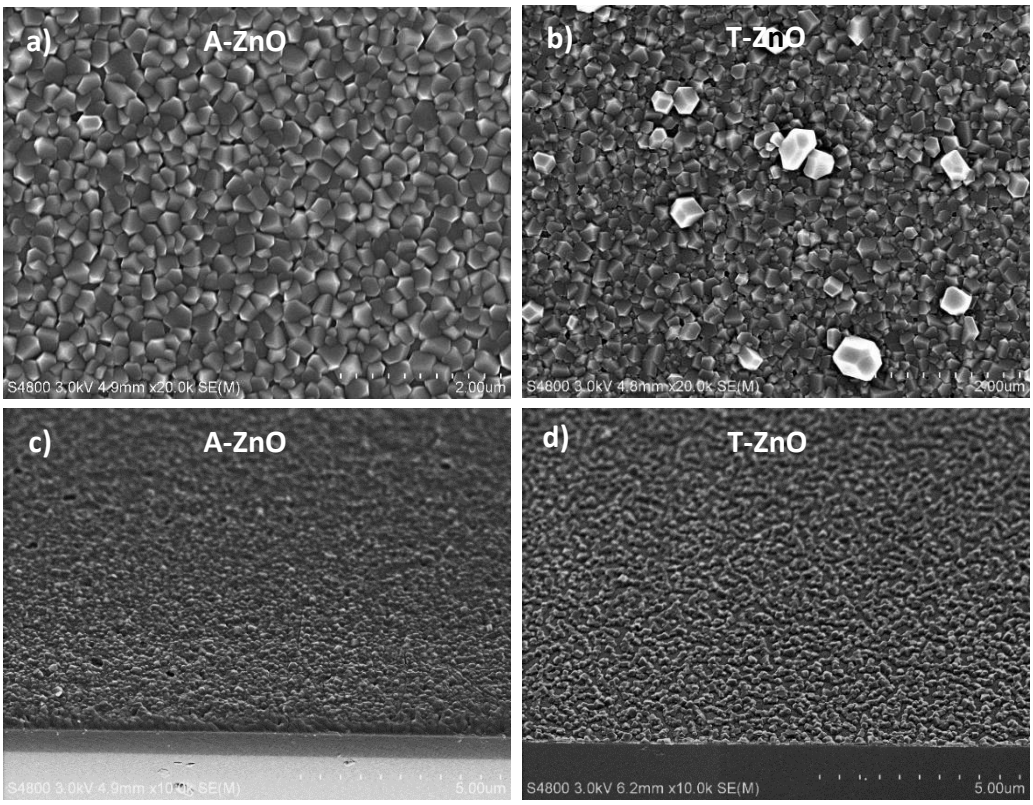

Figure 63. Plan-view SEM images of a 7.0 nm A-ZnO (a) and a 5.4 nm T-ZnO (b) converted to ZIF-8 at 200 °C for 30 min. SEM images taken at 45° of a 7.0 nm A-ZnO (c) and 3.1 nm T-ZnO (d) converted to ZIF-8 at 200 °C for 1 h.

Adhesion properties of the ZIF-8 films on Al_2O_3 with the initial ZnO thicknesses of 33 and 65 nm were briefly assessed with the Scotch tape adhesion test (Figure 64). Both films had undergone conversion at 200 °C for 30 min. Although it first seems that the ZIF-8 film with the higher initial ZnO thickness of 65 nm (Figure 64a) had delaminated completely, the SEM image (Figure 64c) shows that a major part of it remained on the substrate. Only some of the larger crystals appear to have delaminated. The ZIF-8 film with the lower initial ZnO thickness of 33 nm (Figure 64d,e,f) experienced more severe delamination. This film has larger ZIF-8 crystals, but some of the larger crystals as well as most of the whole film endured the test. No visible film was left on the tape pieces used in either of the adhesion tests.

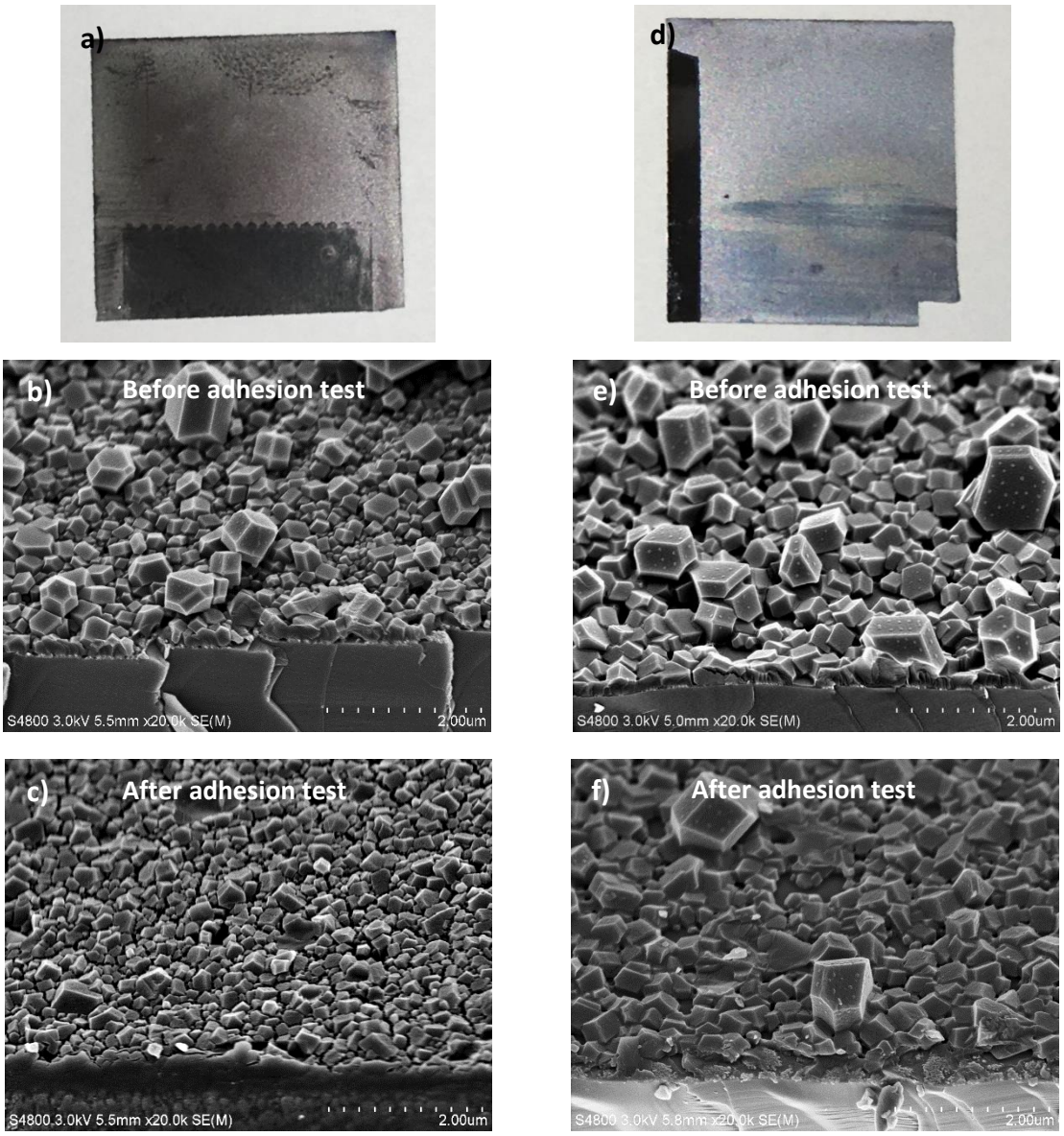

Figure 64. Photograph (a) and SEM images taken at 45° of a 65 nm A-ZnO converted to ZIF-8 before (b) and after (c) a Scotch tape adhesion test. Corresponding photograph (d) and SEM images of a 33 nm A-ZnO film converted to ZIF-8 before (e) and after (f) the test.

Various ZIF-8 films were stored under ambient conditions for one year to examine their stability. ZIF-8 films with initial A-ZnO and T-ZnO thicknesses of 7.0 and 3.0 nm, respectively, converted at 200 °C for 1 h are taken as examples of the changes occurred during this time. Significant changes in the crystal structure of both films can be observed in SEM images (Figure 65) taken directly after the conversion and one year later. Diffractograms of these films (Figure 66) concur with the SEM images: the films have not endured the storage and have turned amorphous. The same had also happened with the films converted in 200 °C for 2 h and 30 min.

The films have possibly reacted with air moisture and CO_2. There has been some debate about whether ZIF-8 is stable in water, but for example Leus et al.[216] found that although ZIF-8 survived hydrothermal stability tests without structural degradation, new diffraction peaks appeared in powder XRD when ZIF-8 was stored in air at room temperature for two months. These peaks were assigned to hydrolytic degradation products of ZIF-8 which are formed due to chemical reactions of the framework with CO_2 in the presence of water.

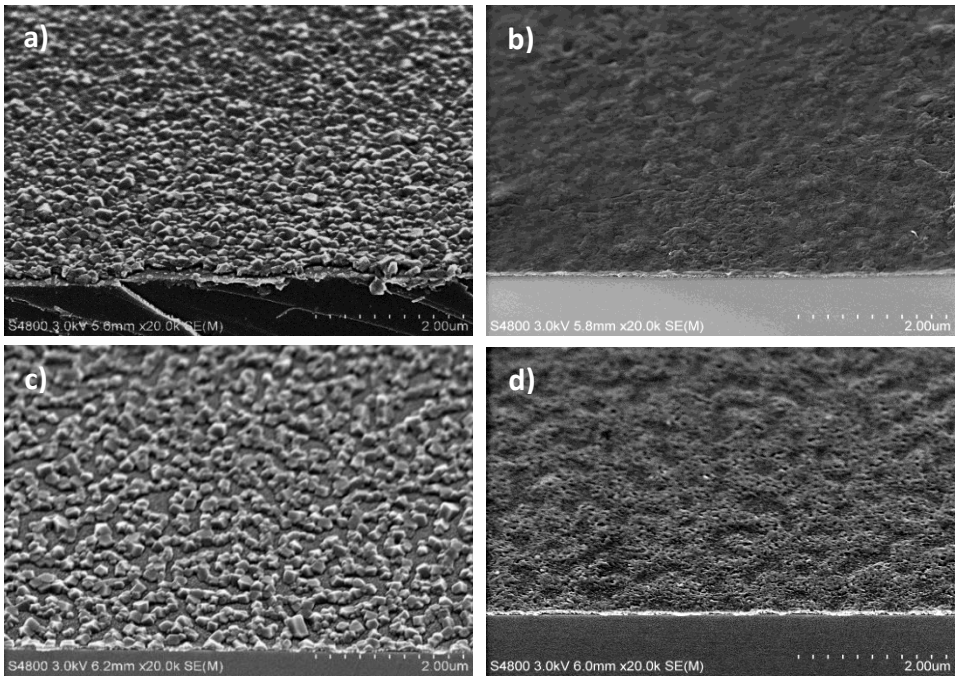

Figure 65. SEM images taken at 45° of ZIF-8 films converted at 200 °C for 1 h. Images a and b correspond to films with an initial A-ZnO thickness of 7.0 nm imaged directly after the conversion (a) and one year after the conversion (b). Images c and d correspond to the initial T-ZnO thickness of 3.0 nm imaged directly after the conversion (c) and one year after the conversion (d).

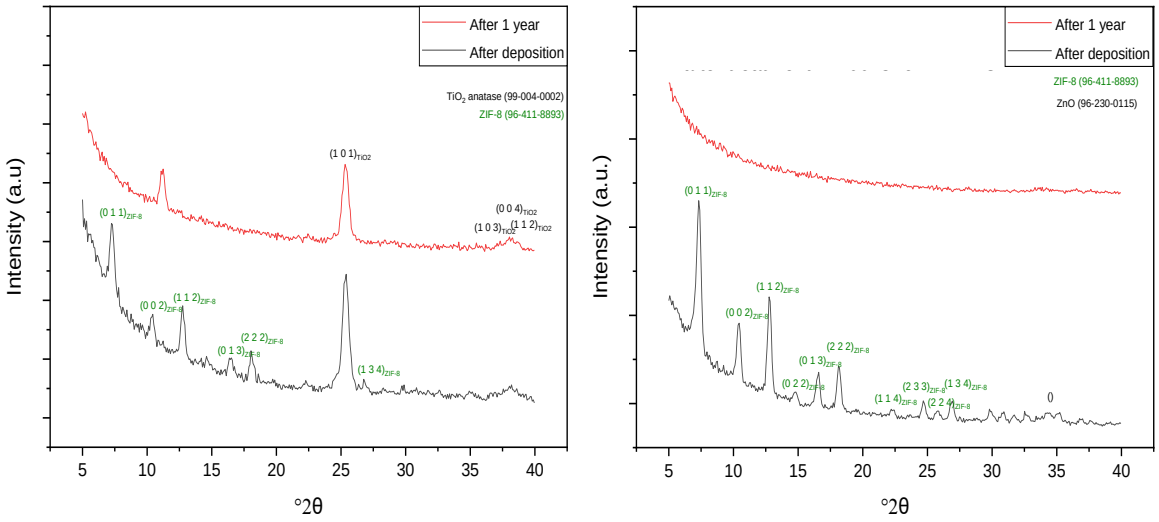

Figure 66. Diffractograms of ZIF-8 films converted at 200 °C for 1 h. The initial A-ZnO thickness 7.0 nm (right) and T-ZnO thickness of 3.0 nm (left). The unidentified peaks at 30-35° in the right diffractogram are believed to belong to ZIF-8.

7.5 Aluminum Oxide

The conversion of smooth Al_2O_3 thin films to a grass-like Al_2O_3 morphology is described in this section. The aim of these experiments was to explore some of the causes and applications of this conversion.

To confirm that the conversion reaction from smooth alumina to grass-like alumina previously observed by Isakov[137] (described in section 4.2.1) occurs only when Al_2O_3 thin films are contacted with liquid water, an Al_2O_3 thin film with a thickness of 92 nm, deposited with TMA and H_2O as precursors at 250 °C, was placed in Conversion Reactor Z. All the water-treated films in this section were blown dry with a nitrogen gun after the experiments. Deionised water (4 ml) was used as the reactant and reaction temperatures were 90, 95 and 109 °C. The film was exposed to water vapor from 18 to 26 h. No changes were visible in the film after these experiments in vacuum (<0.5 mbar) or air pressure. The film was also placed in Conversion Reactor Y at 300 °C and 0.15 mbar for 4 h. No changes were observed on the film.

The Al_2O_3 film was placed inside the autoclave together with deionised water at both 90 and 95 °C for 24-72 h. The results were inconsistent; small, silvery spots were formed on the film after 43 h of treatment at 90 and 95 °C (Figure 67), but no changes were visually observed in separate treatments at 95 °C for 24 or 72 h. There was a significant thickness change from 92 to 162 nm for the film treated for 43 h at 90 °C. The thicknesses of the other films remained constant.

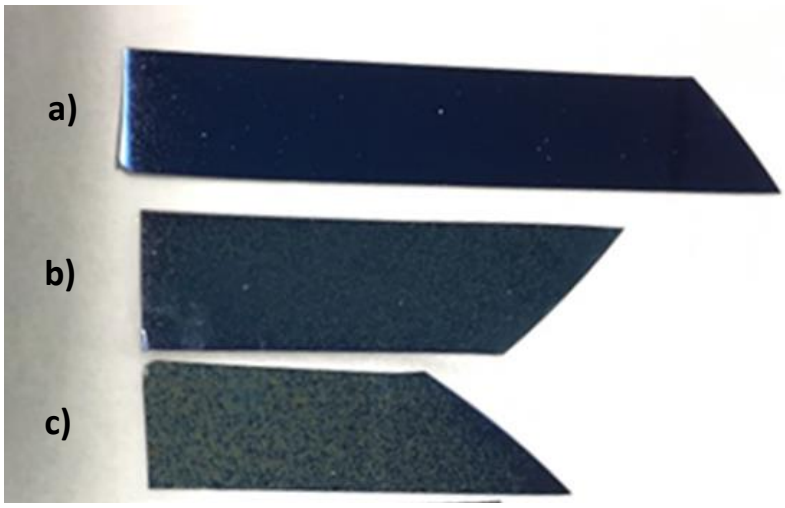

Figure 67. Photograph of an Al_2O_3 thin film with a thickness of 92 nm before (a), and after a 43 h treatment in deionised H_2O vapor in an autoclave at 95 (b) and 90 °C (c).

SEM (Figures 68a-f) revealed the silvery spots to look like droplets with a grass-like morphology at the edges. Centers of the droplets appeared to have dissolved, leaving cavities in the film. The spots are a result of small water droplets condensing on the film in the autoclave. This was confirmed by pipetting water droplets onto the film at 95 °C. The droplets were left on the film for 90 h in a 95 °C oven. A morphology similar to the small, silvery spots formed in the autoclave experiments were revealed in SEM images taken from the center of the droplets.

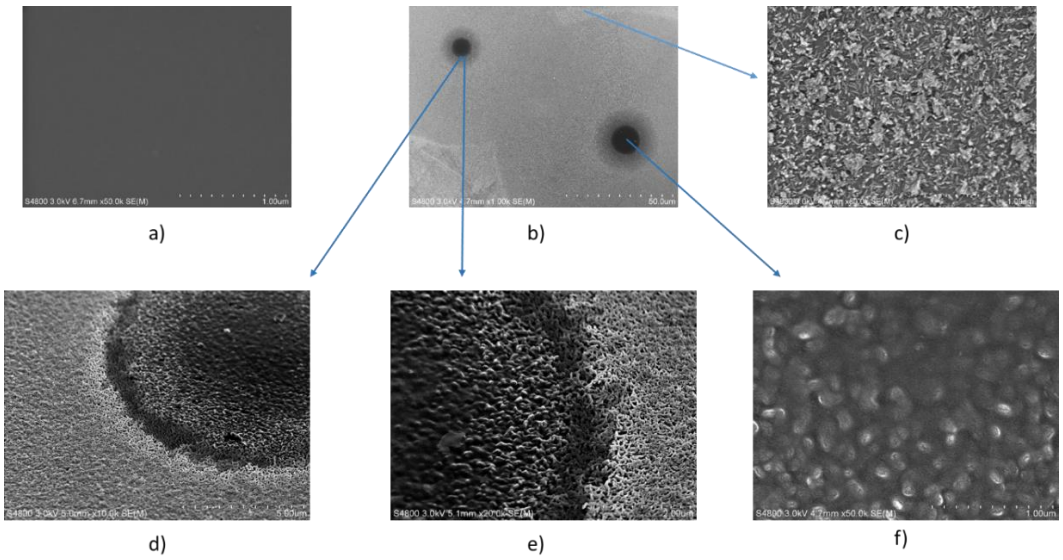

Figure 68. SEM images of an Al_2O_3 thin film with a thickness of 92 nm before (a), and after (b-f) a 43 h treatment with H_2O vapor in an autoclave at 90 °C. Figures c-f are magnified images of the different areas of the film in (b), as indicated by the arrows.

The 92 nm Al_2O_3 film was then submerged in 20 ml distilled water at 10 °C intervals from 40 to 90 °C for 30 min to observe the effect of the temperature of the water on the behaviour of the film. At 40 and 50 °C, no changes were visually observed on the film. From 60 to 90 °C, the films changed from mirror-like blue to a lighter, matte milky color. Figure 69 shows an image of a 200 nm Al_2O_3 film after immersion in water at 70 °C for 30 min. All the lines on the film have come from it facing down on a cleanroom paper while in storage. All the converted films had clear marks on them on areas that they have been handled from. This is caused by the grass-like featured collapsing under the pressure of mechanical stress. At 95 °C, the film had dissolved in 3 days.

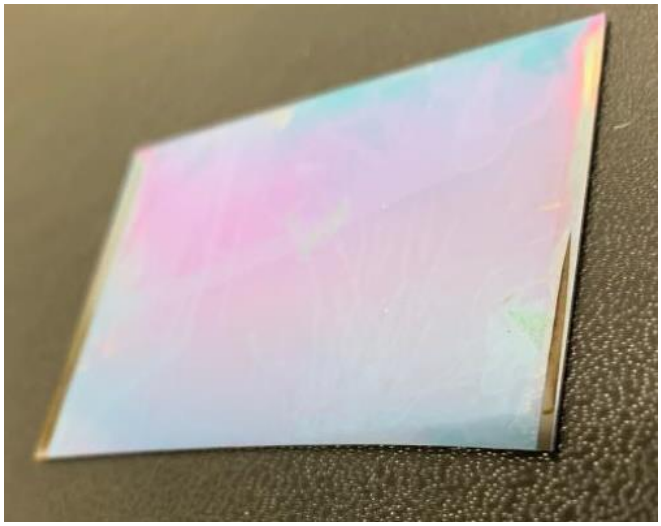

Figure 69. A photograph of a 200 nm Al_2O_3 film grown with TMA and H_2O as precursors at 250 °C after treatment in water at 70 °C for 30 min.

To compare if the precursors used for the Al_2O_3 deposition influenced the formation of the grass-like morphology, an Al_2O_3 film with a thickness of approximately 100 nm, grown with $AlCl_3$ and H_2O as precursors at 300 °C, was also immersed in 60 °C deionised water for 30 min. To explore the speculations of Isakov[137] regarding the grass-like film to form due to the combination of the high surface tension of water and blow-drying the film (section 4.2.1), Al_2O_3 films deposited with both precursor variations ($AlCl_3$ and TMA) were immersed in 60 °C deionised water for 30 min, drenched in ethanol immediately after coming out of the water bath, and then blow-dried. The surface tension of ethanol is significantly lower than that of deionised water.[217]

The film morphology transformations were equal, as can be seen from Figure 70. Both films converted to grass-like films, so the surface tension of water most likely does not affect the formation of the Al_2O_3 grass. Figures 70c and d display the significant thickness changes that took place on the films: the film grown with $AlCl_3$ thickened from approximately 100 nm to 500 nm and the one grown with TMA from approximately 92 nm to 700 nm. Figure 70d shows that the transformation extends throughout the whole film, since the view is from underneath the film due to a piece of the grass-like film delaminating from its substrate. XRD revealed the amorphous Al_2O_3 to have at least partially crystallized (Figure 71), and the broadness of the peaks suggests a nanocrystalline structure. The peaks could not be certainly designated to any phases or compounds but were closest to a variety of aluminum hydroxides. The presence of hydroxides could be verified with FTIR, for example.

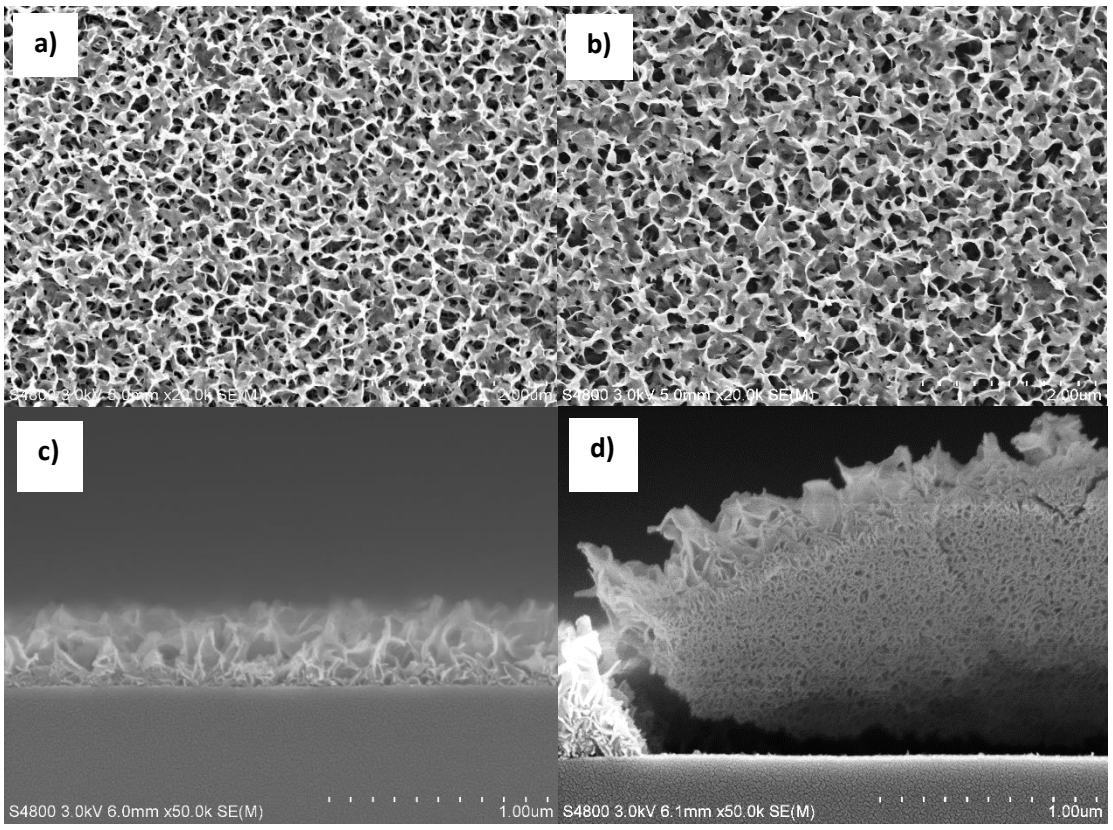

Figure 70. SEM images of Al_2O_3 films after immersion in water at 60 °C for 30 min taken at plan-view (a,b) and from a fractured cross-section angle (c,d). Precursors for Al_2O_3 thin films were $AlCl_3$ and H_2O (a,c) and TMA and H_2O (b,d).

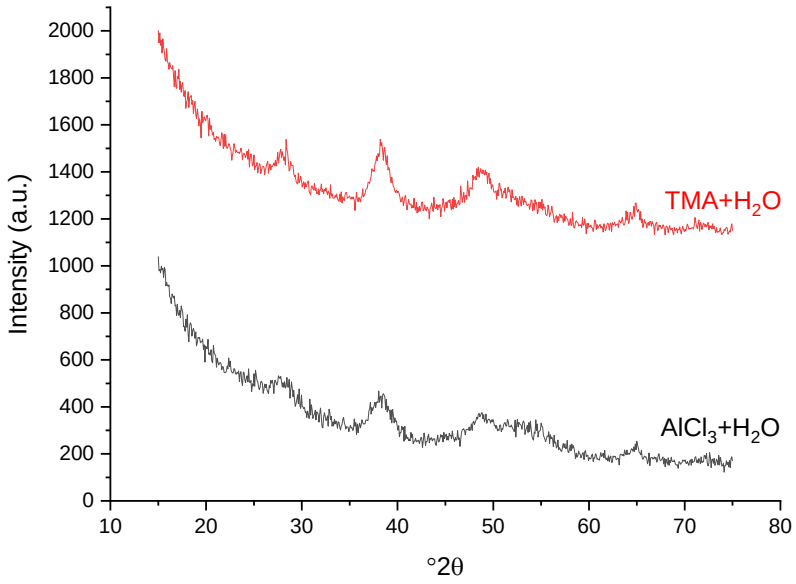

Figure 71. XRD of Al_2O_3 films after immersion in water at 60 °C for 30 min. Precursors for Al_2O_3 thin films: TMA and H_2O (top), $AlCl_3$ and H_2O (bottom).

An Al_2O_3 film grown with TMA and H_2O at 250 °C with a thickness of approximately 20 nm was submerged in 70 °C DIW for 30 min. The resulting grass-like film was subsequently heated up to 1200 °C in air. HTXRD measurements (Figure 72) display no significant changes in the nanocrystalline structure of the film until it is cooled from 1200 °C back to 25 °C. The diffractogram surprisingly shows that the film has crystallized into corundum. SEM images (Figure 73) show that the structure of the grass-like film has, however, not changed significantly. The only apparent change is a slight porosity on the grass structure. However, due to the crystallization occuring only during cool-down and no observed apparent changes in the grass-like structure itself, it cannot be ruled out that some Al_2O_3 from the HTXRD equipment might have fallen on the sample.

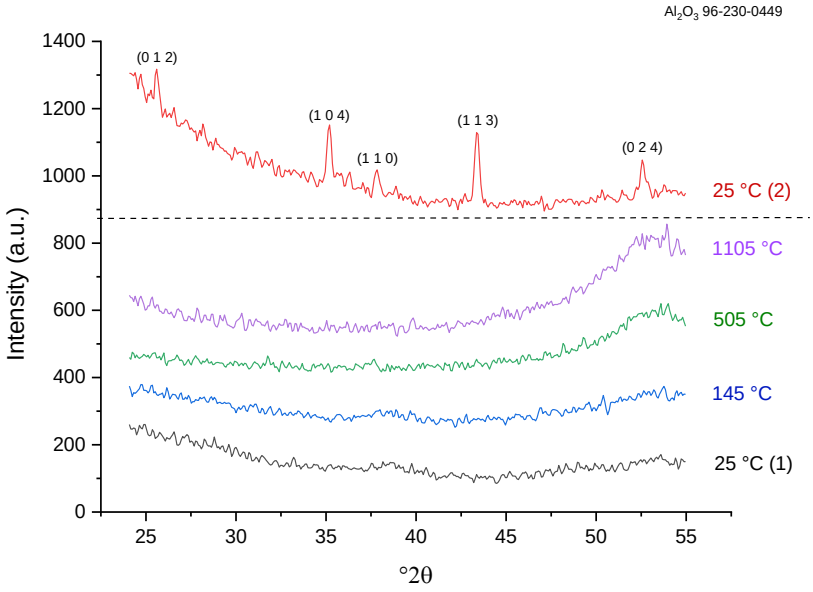

Figure 72. HTXRD measurements of a grass-like Al_2O_3 film heated up to 1200 °C in air. The curve 25 °C (1) represents the diffractogram taken at the start of the measurement and 25 °C (2) immediately after cooling down the film from 1200 °C to 25 °C.

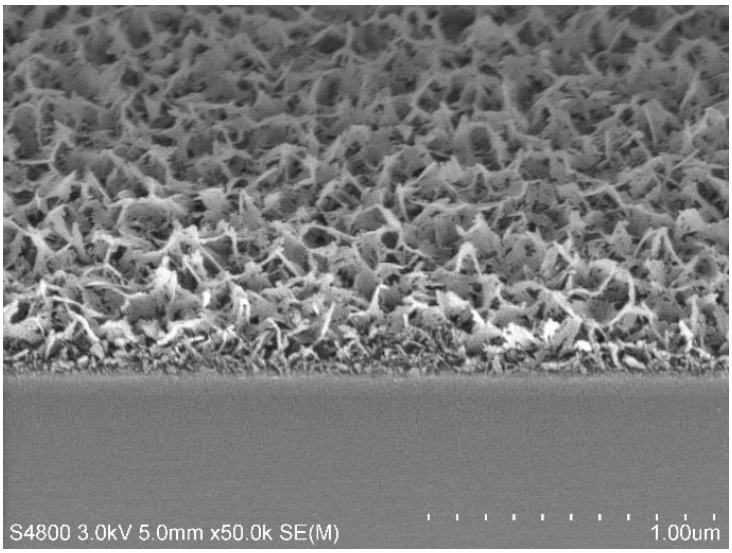

Figure 73. SEM image taken at 45° angle of a grass-like Al_2O_3 film after being heated to 1200 °C in air.

A 20 nm Al_2O_3 thin film was converted to grass-like Al_2O_3 by submerging it in 70 °C water for 30 min. This structure (Figure 74a) was then coated with TiO_2 to examine if the grass could serve as a 3D substrate for other ALD films, or if it would disintegrate under typical ALD process conditions. $TiCl_4$ and H_2O precursors and a deposition temperature of 250 °C

were used to coat the grass with an approximately 40 nm TiO_2 film (Figure 74b). The grass structure clearly has not collapsed during this process and might even be completely intact under the TiO_2 film. However, the TiO_2 film has not grown uniformly on this structure. Uniform deposition of the TiO_2 on the grass-like structure can be tricky since some of the pores in the structure may be inaccessible. Additionally, the pulse and purge times were not optimized at all and the thickness of the TiO_2 coating was quite high compared to the substrate dimensions, which also affect the uniformity of the film significantly.

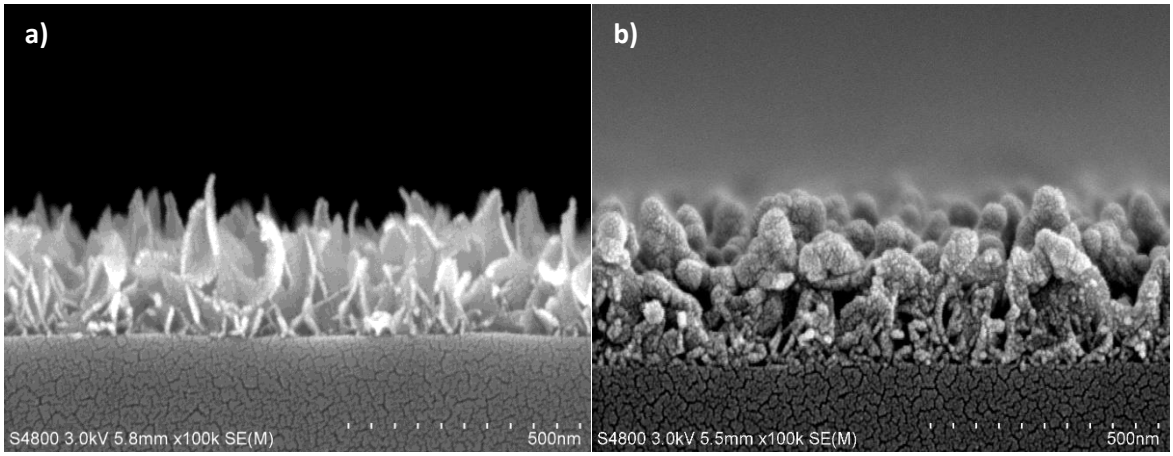

Figure 74. SEM images taken at a 90° angle of a 20 nm Al_2O_3 thin film converted to grass-like Al_2O_3 by submerging it in 70 °C water for 30 min (a) and the same film coated with 40 nm TiO_2 (b).

Conversion of ZnO thin films to ZIF-8 was also attempted on this 3D substrate. First, a 20 nm Al_2O_3 film was converted to a grass-like structure by submerging it in 70 °C water for 30 min. This film was then coated with about 10 nm of ALD ZnO. The ZnO-coated Al_2O_3 grass was placed in Conversion Reactor Z under HmIM vapor at 200 °C for 2 h. SEM images reveal that the film has indeed converted to ZIF-8 (Figure 75). Unfortunately, the Al_2O_3 grass has been crushed at least partly underneath the large ZIF-8 crystals. This could possibly be avoided by depositing an extremely thin (<2 nm) ZnO film on the grass before the conversion to ZIF-8. This way the final crystal size would not be so unequal in size to the underlying structure and might preserve the grass-like structure.

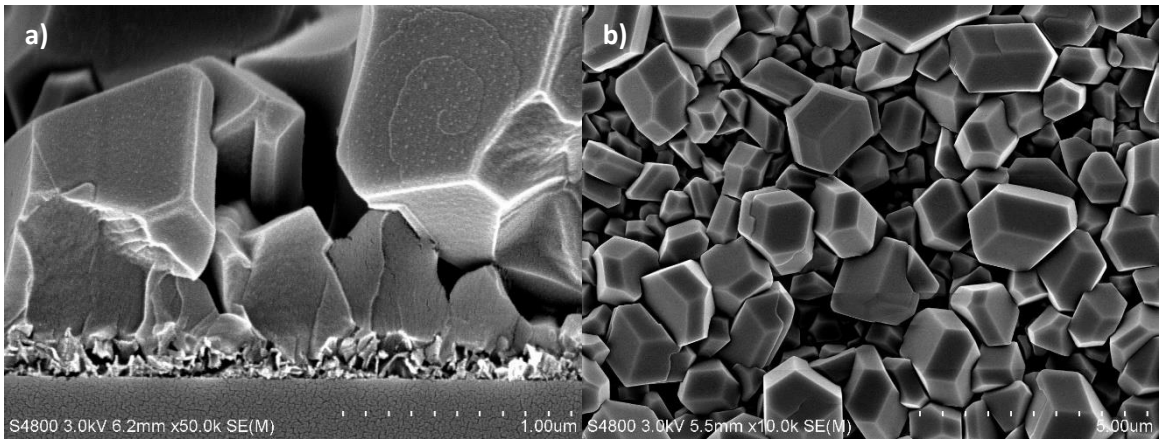

Figure 75. SEM images taken from (a) a 90° angle and (b) plan-view of a ZIF-8 film made by converting a 10 nm ZnO film on grass-like alumina under HmIM vapor at 200 °C for 2 h.

8 Conclusions

Conversions of ALD Ru to RuO_2, Re to ReO_3, ZrO_2 to UiO-66, ZnO to ZIF-8, and Al_2O_3 to a grass-like structure by simple reactions were explored. The conversion experiments were done in an autoclave, two in-house built conversion reactors, and a simple beaker with water.

Ru thin films of various thicknesses were successfully converted to RuO_2 through a one-step conversion process under ambient air and O_2 atmospheres. The roughness and continuity of the RuO_2 films must be assessed by heating them only until the conversion has fully occurred and analysing them. Suitable methods for the analysis include SEM, AFM, and XRR, for example. Although the conversion temperatures appear to be quite high (400-600°C), O_2 atmosphere should be used and starting Ru film thicknesses reduced to match the applications mentioned in section 4.1.1, consequently bringing down the required temperatures. If the morphology of the converted films does not meet the expectations, different heating rates and oxidizing atmospheres should be explored.

Re and ReN_x films start converting to ReO_3 already at room temperature under ozone and high humidity. The oxide seems to form large crystals that crack out of both films. This is problematic since film continuity is damaged. In the 100 °C ozone treatment the film visibly cracked more than in the room temperature treatments. The next step should be exploring even milder reaction conditions, such as room temperature and an O_2 environment or elevated temperatures and a H_2O environment, and longer conversion durations, such as 24-48 h, to see if this would result in betterfilm morphology.

The conversion of zirconium oxide compound ALD thin films to UiO-66 through a single-step reaction with terephthalic acid and acetic acid was unsuccessful. Thin films of zirconium oxides were placed under the acid vapors at 250 and 300 °C for 1-18 h without any observable changes. The conversion of various zirconium compound thin films with different crystallinities (amorphous, weakly crystalline, crystalline) and thicknesses were placed under terephthalic acid and acetic acid the 300 °C for 4-68 h. The amorphous films exhibited some changes in their visual appearance after 7 h, and SEM images revealed

bubbles in the films. The films had, however, not crystallized, and crystallization attempts with additional acetic acid were unsuccessful.

The ALD-deposited ZnO thin films on Al_2O_3 and TiO_2 were successfully completely converted to ZIF-8 upon a treatment under HmIM vapor at 200 °C for 2 h. This is a one-step conversion for ZIF-8 films with accurate initial ZnO film thickness control. Conversions at 200 °C with both A-ZnO and T-ZnO films yielded >90 % ZIF-8 for ZnO films below 10 nm in thickness for all conversion times. At first, nucleation of ZIF-8 crystals takes place at random sites on the substrate. Nucleation density seems to be smaller at lower conversion temperatures (150 °C). After the initial crystal growth, the crystals coalesce and start to grow larger at arbitrary sites when available sites on the substrate run out. At later stages, the conversion seems to progress in a linear manner through the ZnO film. The conversion reaction seems to progress with a higher rate at higher (200 °C) temperatures. The largest crystals delaminated in a tape test. Compared with TiO_2, Al_2O_3 seems to be a better underlayer for ZIF-8 growth.

To gain a better understanding of the ZIF-8 conversion reaction, more experiments must be conducted. ZnO films could be deposited at lower temperatures (150-200 °C) on both adhesion layers to improve growth rates. Conversion of thicker ZnO films (>50 nm) should be attempted and an optimal conversion temperature looked for. As mentioned in section 4.4.1, water plays an important role in this conversion. Small amounts of water could be implemented to this conversion to see if this influences the reaction rate. Adhesion tests should also be conducted on TiO_2-based ZIF-8 films.

Grass-like alumina turned out to be a three-dimensional structure with outstanding heat resistance. It is formed through a reaction between liquid H_2O and Al_2O_3 thin films. Any reaction with water vapor was ruled out. Suitable Al_2O_3 films can be grown at least with $AlCl_3$ or TMA together with H_2O as precursors and have thicknesses of 20-200 nm. The optimum conversion conditions were 60 and 70 °C and 30 min. No reaction was observed at lower temperatures for this conversion time. The conversion reaction is simple and does not require any complicated setups or rare precursors. Therefore, the suitability of this method should be further studied for applications such as antireflective coatings. The structure can possibly also serve as a 3-dimensional substrate for applications requiring high surface areas. The grass-like Al_2O_3 structure was successfully coated with TiO_2 as well

as ZnO, and the conversion of the ZnO thin film to ZIF-8 was attempted on this 3D substrate. The alumina grass unfortunately collapsed under the large ZIF-8 crystals. An extremely thin (<2 nm) ZnO thin film should be deposited on the grass to see if the structure could support smaller ZIF-8 crystals.

This thesis demonstrated various possibilities of conversion reactions of ALD thin films. Several conversions were successful, yielding thin films of promising materials. Others, on the other hand, were not as successful. These are representative examples of how conversions can be extremely simple in principle but require effort while being studied and optimized. The road to utilizing conversion reactions to obtain certain thin film materials with ALD characteristics is in its early stages but shows great promise to become a widely used tool.

Acknowledgements

I would like to thank Prof. Ritala and Prof. Leskelä for giving me the opportunity to learn about ALD from the best in the field. Your lectures and guidance have inspired me and sparked a great interest in this topic. I would also like to thank Prof. Ritala and Prof. Putkonen for their valuable comments.

I would like to thank Dr. Jani Hämäläinen and Dr. Sanni Seppälä for providing me with high-quality samples for my experiments. My gratitude goes also to Mikko Heikkilä for teaching and helping me with the ins and outs of all my X-ray measurements, and Marianna Kemell for showing me the secrets of SEM imaging.

I am thankful for the brilliant insights on this whole process as well as the wise words of my friend Miika. He and Juulia are truly the two sunshines of research motivation. To my mentor, Jani, I owe my deepest gratitude. His never-quenching thirst for new ideas and tremendous positivity truly encouraged me. Thank you for your help while out on the town, at the office, coffee breaks, and any time my mind hit a total blank. Your wisdom and incredible kindness make me feel privileged to have been able to work with you.

9 References

1 D. Muñoz-Rojas, T. Maindron, A. Esteve, F. Piallat, J. C. S. Kools and J.-M. Decams, *Mater. Today Chem.*, 2019, **12**, 96–120.

2 T. Suntola, *Mater. Sci. Reports*, 1989, 4, 261–312.

3 M. Leskelä and M. Ritala, in *Thin Solid Films*, Elsevier, 2002, vol. 409, pp. 138–146.

4 M. Ritala and J. Niinistö, in *ECS Transactions*, ECS, 2009, vol. 25, pp. 641–652.

5 E. Langereis, M. Creatore, S. B. S. Heil, M. C. M. van de Sanden and W. M. M. Kessels, *Appl. Phys. Lett.*, 2006, **89**, 081915.

6 B. Díaz, E. Härkönen, J. Światowska, V. Maurice, A. Seyeux, P. Marcus and M. Ritala, *Corros. Sci.*, 2011, **53**, 2168–2175.

7 Z. Chai, Y. Liu, J. Li, X. Lu and D. He, *RSC Adv.*, 2014, **4**, 50503–50509.

8 M. Leskelä and M. Ritala, *Thin Solid Films*, 2002, **409**, 138–146.

9 S. M. George, *Chem. Rev.*, 2010, **110**, 111–131.

10 *T. Suntola J. Antson, US Pat. 4058430*.

11 G. N. Parsons, J. W. Elam, S. M. George, S. Haukka, H. Jeon, W. M. M. (Erwin) Kessels, M. Leskelä, P. Poodt, M. Ritala and S. M. Rossnagel, *J. Vac. Sci. Technol. A*, 2013, **31**, 050818.

12 M. Leskelä and M. Ritala, *Angew. Chemie Int. Ed.*, 2003, **42**, 5548–5554.

13 J. A. Kittl, K. Opsomer, M. Popovici, N. Menou, B. Kaczer, X. P. Wang, C. Adelmann, M. A. Pawlak, K. Tomida, A. Rothschild, B. Govoreanu, R. Degraeve, M. Schaekers, M. Zahid, A. Delabie, J. Meersschaut, W. Polspoel, S. Clima, G. Pourtois, W. Knaepen, C. Detavernier, V. V. Afanas'ev, T. Blomberg, D. Pierreux, J. Swerts, P. Fischer, J. W. Maes, D. Manger, W. Vandervorst, T. Conard, A. Franquet, P. Favia, H. Bender, B. Brijs, S. Van Elshocht, M. Jurczak, J. Van Houdt and D. J. Wouters, *Microelectron. Eng.*, 2009, **86**, 1789–1795.

14 J. Niinistö, K. Kukli, M. Heikkilä, M. Ritala and M. Leskelä, *Adv. Eng. Mater.*, 2009, **11**, 223–234.

15 Y. Xuan, T. Shen, M. Xu, Y. Q. Wu and P. D. Ye, in *2008 IEEE International Electron Devices Meeting*, IEEE, 2008, pp. 1–4.

16 H. Kim, C. Detavenier, O. van der Straten, S. M. Rossnagel, A. J. Kellock and D.-G. Park, *J. Appl. Phys.*, 2005, **98**, 014308.

17 A. Kohn and M. Eizenberg, in *Advanced Nanoscale ULSI Interconnects: Fundamentals and Applications*, Springer New York, New York, NY, 2009, pp. 93–120.

18 H. Schmidt, K. Zilberberg, S. Schmale, H. Flügge, T. Riedl and W. Kowalsky, *Appl. Phys. Lett.*, 2010, **96**, 243305.

19 J. Benick, B. Hoex, M. C. M. van de Sanden, W. M. M. Kessels, O. Schultz and S. W. Glunz, *Appl. Phys. Lett.*, 2008, **92**, 253504.

20 L. Liu, S. K. Karuturi, L. T. Su and A. I. Y. Tok, *Energy Environ. Sci.*, 2011, **4**, 209–215.

21 P. Chen, T. Mitsui, D. B. Farmer, J. Golovchenko, A. Roy G. Gordon and Daniel Branton, , DOI:10.1021/NL0494001.

22 H. Kim, E. Pippel, U. Gösele and M. Knez, *Langmuir*, 2009, **25**, 13284–13289.

23 Y. W. Chen, M. Liu, T. Kaneko and P. C. McIntyre, *Electrochem. Solid-State Lett.*, 2010, **13**, G29.

24 E. Marin, A. Lanzutti, L. Guzman and L. Fedrizzi, *J. Coatings Technol. Res.*, 2011, **8**, 655–659.

25 H. Klumbies, P. Schmidt, M. Hähnel, A. Singh, U. Schroeder, C. Richter, T. Mikolajick, C. Hoßbach, M. Albert, J. W. Bartha, K. Leo and L. Müller-Meskamp, *Org. Electron.*, 2015, **17**, 138–143.

26 Y. Zhao, L. V. Goncharova, Q. Zhang, P. Kaghazchi, Q. Sun, A. Lushington, B. Wang, R. Li and X. Sun, *Nano Lett.*, 2017, **17**, 5653–5659.

27 P. Heikkilä, T. Hirvikorpi, H. Hilden, J. Sievänen, L. Hyvärinen, A. Harlin and M. Vähä-

Nissi, *J. Mater. Sci.*, 2012, **47**, 3607–3612.

28 H. B. Profijt, S. E. Potts, M. C. M. van de Sanden and W. M. M. Kessels, *J. Vac. Sci. Technol. A Vacuum, Surfaces, Film.*, 2011, **29**, 050801.

29 N. J. Tro, *Chemistry: A Molecular Approach*, Pearson Education Limited, 4th edn., 2017.

30 E. Atosuo, M. Mäntymäki, K. Mizohata, M. J. Heikkilä, J. Räisänen, M. Ritala and M. Leskelä, *Chem. Mater.*, 2017, **29**, 998–1005.

31 S. M. Ali, M. S. Algarawi, T. S. ALKhuraiji, S. S. Alghamdi, M. H. Aziz and M. Isa, *Nucl. Sci. Tech.*, 2018, **29**, 104.

32 Y. P. Wang, Z. J. Ding, Q. X. Liu, W. J. Liu, S. J. Ding and D. W. Zhang, *J. Mater. Chem. C*, 2016, **4**, 11059–11066.

33 I. Stassen, M. Styles, G. Grenci, H. V. Gorp, W. Vanderlinden, S. D. Feyter, P. Falcaro, D. De Vos, P. Vereecken and R. Ameloot, *Nat. Mater.*, 2016, **15**, 304–310.

34 C. T. Chen, J. Pedrini, E. A. Gaulding, C. Kastl, G. Calafiore, S. Dhuey, T. R. Kuykendall, S. Cabrini, F. M. Toma, S. Aloni and A. M. Schwartzberg, *Sci. Rep.*, 2019, **9**, 2768.

35 C. Kauppinen, K. Isakov and M. Sopanen, 2017, **9**, 15038−15043.

36 D. Alburquenque, V. Bracamonte, M. Del Canto, A. Pereira and J. Escrig, *MRS Commun.*, 2017, **7**, 848–853.

37 J. Chae, H. S. Park and S. W. Kang, *Electrochem. Solid-State Lett.*, 2002, **5**, C64.

38 T. Waechtler, S. Oswald, N. Roth, A. Jakob, H. Lang, R. Ecke, S. E. Schulz, T. Gessner, A. Moskvinova, S. Schulze and M. Hietschold, *J. Electrochem. Soc.*, 2009, **156**, H453.

39 J. M. Park, K. Jin, B. Han, M. J. Kim, J. Jung, J. J. Kim and W. J. Lee, *Thin Solid Films*, 2014, **556**, 434–439.

40 Z. Li and R. G. Gordon, *Chem. Vap. Depos.*, 2006, **12**, 435–441.

41 K. Väyrynen, University of Helsinki, 2019.

42 I. Stassen, D. De Vos and R. Ameloot, *Chem. - A Eur. J.*, 2016, **22**, 14452–14460.

43 K. B. Lausund and O. Nilsen, *Nat. Commun.*, 2016, **7**, 13578.

44 M. Mattinen, T. Hatanpää, P. J. King, K. Meinander, K. Mizohata, P. Jalkanen, J. Räisänen, M. Ritala and M. Leskelä, *J. Vac. Sci. Technol. A*, 2019, **37**, 020921.

45 M. Mattinen, P. J. King, L. Khriachtchev, K. Meinander, J. T. Gibbon, V. R. Dhanak, J. Räisänen, M. Ritala and M. Leskelä, *Small*, 2018, **14**, e1800547.

46 S. M. George and Y. Lee, *ACS Nano*, 2016, **10**, 4889–4894.

47 K. J. Kanarik, T. Lill, E. A. Hudson, S. Sriraman, S. Tan, J. Marks, V. Vahedi and R. A. Gottscho, *J. Vac. Sci. Technol. A Vacuum, Surfaces, Film.*, 2015, **33**, 020802.

48 N. R. Johnson and S. M. George, *ACS Appl. Mater. Interfaces*, 2017, **9**, 34435–34447.

49 J. W. DuMont, A. E. Marquardt, A. M. Cano and S. M. George, *ACS Appl. Mater. Interfaces*, 2017, **9**, 10296–10307.

50 D. R. Zywotko and S. M. George, *Chem. Mater.*, 2017, **29**, 1183–1191.

51 H. Lan, L. D. Salmi, T. Rönkkö, J. Parshintsev, M. Jussila, K. Hartonen, M. Kemell and M.-L. Riekkola, *Anal. Chim. Acta*, 2018, **1024**, 93–100.

52 J. Holopainen, M. J. Heikkilä, L. D. Salmi, K. Ainassaari and M. Ritala, *Microporous Mesoporous Mater.*, 2018, **267**, 212–220.

53 Noble metal | chemistry | Britannica.com, https://www.britannica.com/science/noble-metal, (accessed 31 May 2019).

54 J. Hämäläinen, M. Ritala and M. Leskelä, *Chem. Mater.*, 2014, **26**, 786–801.

55 A. Ferretti, D. B. Rogers and J. B. Goodenough, *J. Phys. Chem. Solids*, 1965, **26**, 2007–2011.

56 J. Hämäläinen, University of Helsinki, 2013.

57 M. Popovici, B. Groven, K. Marcoen, Q. Manh Phung, S. Dutta, J. Swerts, J. Meersschaut, J. A. van den Berg, A. Franquet, A. Moussa, K. Vanstreels, P. Lagrain,

H. Bender, M. Jurczak, S. Van Elshocht, A. Delabie and C. Adelmann, *Chem. Mater*, 2017, **29**, 4666.

58 Ruthenium Prices and Ruthenium Price Charts - InvestmentMine, http://www.infomine.com/investment/metal-prices/ruthenium/, (accessed 31 May 2019).

59 S. Rangan, E. Bersch, R. A. Bartynski, E. Garfunkel and E. Vescovo, *Phys. Rev. B*, 2009, **79**, 075106.

60 Y.-S. Suh, H. Lazar, B. Chen, J.-H. Lee and V. Misra, *J. Electrochem. Soc.*, 2005, **152**, F138.

61 C. Zhao, M. Pawlak, M. I. Popovici, M. Schaekers, E. Sleeckx, E. Vancoille, D. Wouters, Z. Tokei and J. Kittl, in *ECS Transactions*, ECS, 2009, vol. 25, pp. 377–387.

62 J. A. Kittl, K. Opsomer, M. Popovici, N. Menou, B. Kaczer, X. P. Wang, C. Adelmann, M. A. Pawlak, K. Tomida, A. Rothschild, B. Govoreanu, R. Degraeve, M. Schaekers, M. Zahid, A. Delabie, J. Meersschaut, W. Polspoel, S. Clima, G. Pourtois, W. Knaepen, C. Detavernier, V. V. Afanas'ev, T. Blomberg, D. Pierreux, J. Swerts, P. Fischer, J. W. Maes, D. Manger, W. Vandervorst, T. Conard, A. Franquet, P. Favia, H. Bender, B. Brijs, S. Van Elshocht, M. Jurczak, J. Van Houdt and D. J. Wouters, *Microelectron. Eng.*, 2009, **86**, 1789–1795.

63 S.-H. Choi, T. Cheon, S.-H. Kim, D.-H. Kang, G.-S. Park and S. Kim, *J. Electrochem. Soc.*, 2011, **158**, D351.

64 W. M. Haynes, *CRC handbook of chemistry and physics : a ready-reference book of chemical and physical data*, CRC Press, 92nd edn., 2011.

65 D. Z. Austin, M. A. Jenkins, D. Allman, S. Hose, D. Price, C. L. Dezelah and J. F. Conley, *Chem. Mater.*, 2017, **29**, 1107–1115.

66 T. Sawada, T. Nabatame, T. D. Dao, I. Yamamoto, K. Kurishima, T. Onaya, A. Ohi, K. Ito, M. Takahashi, K. Kohama, T. Ohishi, A. Ogura and T. Nagao, *J. Vac. Sci. Technol. A Vacuum, Surfaces, Film.*, 2017, **35**, 061503.

67 C. Gómez-Solís, J. C. Ballesteros, L. M. Torres-Martínez and I. Juárez-Ramírez, *Fuel*,

2016, **166**, 36–41.

68 K. P. J. Gustafson, A. Shatskiy, O. Verho, M. D. Kärkäs, B. Schluschass, C.-W. Tai, B. Åkermark, J.-E. Bäckvall and E. V. Johnston, *Catal. Sci. Technol.*, 2017, **7**, 293–299.

69 S.-J. Park, W.-H. Kim, H.-B.-R. Lee, W. J. Maeng and H. Kim, *Microelectron. Eng.*, 2008, **85**, 39–44.

70 H. Hyo Jun Jung, Jeong Hwan Han, E. A. Jung, B. K. Park, J.-H. Hwang, S. U. Son, C. G. Kim, T.-M. Chung and K.-S. An, *Chem. Mater*, 2014, **26**, 7090.

71 S. Yeo, J.-Y. Park, S.-J. Lee, D.-J. Lee, J. H. Seo and S.-H. Kim, *Microelectron. Eng.*, 2015, **137**, 16–22.

72 T. E. Hong, S.-H. Choi, S. Yeo, J.-Y. Park, S.-H. Kim, T. Cheon, H. Kim, M.-K. Kim and H. Kim, *ECS J. Solid State Sci. Technol.*, 2013, **2**, P47–P53.

73 N. Leick, S. Agarwal, A. J. M. Mackus and W. M. M. Kessels, *Chem. Mater.*, 2012, **24**, 3696–3700.

74 T. Aaltonen, M. Ritala, K. Arstila, J. Keinonen and M. Leskelä, *Chem. Vap. Depos.*, 2004, **10**, 215–219.

75 K. Kukli, M. Kemell, E. Puukilainen, J. Aarik, A. Aidla, T. Sajavaara, M. Laitinen, M. Tallarida, J. Sundqvist, M. Ritala and M. Leskelä, *J. Electrochem. Soc.*, 2011, **158**, D158.

76 K. Kukli, J. Aarik, A. Aidla, I. Jõgi, T. Arroval, J. Lu, T. Sajavaara, M. Laitinen, A.-A. Kiisler, M. Ritala, M. Leskelä, J. Peck, J. Natwora, J. Geary, R. Spohn, S. Meiere and D. M. Thompson, *Thin Solid Films*, 2012, **520**, 2756–2763.

77 K. Gregorczyk, L. Henn-Lecordier, J. Gatineau, C. Dussarrat and G. Rubloff, *Chem. Mater.*, 2011, **23**, 2650–2656.

78 T. Aaltonen, P. Alén, M. Ritala and M. Leskelä, *Chem. Vap. Depos.*, 2003, **9**, 45–49.

79 J.-Y. Park, S. Yeo, T. Cheon, S.-H. Kim, M.-K. Kim, H. Kim, T. E. Hong and D.-J. Lee, *J. Alloys Compd.*, 2014, **610**, 529–539.

80 A. Salaün, S. B. Newcomb, I. M. Povey, M. Salaün, L. Keeney, A. O'Mahony and M.

E. Pemble, *Chem. Vap. Depos.*, 2011, **17**, 114–122.

81 I. Brytavskyi, K. Hušeková, V. Myndrul, M. Pavlenko, E. Coy, K. Zaleski, D. Gregušová, L. Yate, V. Smyntyna and I. Iatsunskyi, *Appl. Surf. Sci.*, 2019, **471**, 686–693.

82 O.-K. Kwon, J.-H. Kim, H.-S. Park and S.-W. Kang, *J. Electrochem. Soc.*, 2004, **151**, G109.

83 S.-H. Kwon, O.-K. Kwon, J.-H. Kim, S.-J. Jeong, S.-W. Kim and S.-W. Kang, *J. Electrochem. Soc.*, 2007, **154**, H773.

84 J.-H. Kim, D.-S. Kil, S.-J. Yeom, J.-S. Roh, N.-J. Kwak and J.-W. Kim, *Appl. Phys. Lett.*, 2007, **91**, 052908.

85 S.-J. Park, W.-H. Kim, W. J. Maeng, Y. S. Yang, C. G. Park, H. Kim, K.-N. Lee, S.-W. Jung and W. K. Seong, *Thin Solid Films*, 2008, **516**, 7345–7349.

86 W.-H. Kim, S.-J. Park, D. Kim and H. Kim, *J. Korean Phys. Soc.*, 2009, **55**, 32–37.

87 J. H. Han, S. W. Lee, S. K. Kim, S. Han, C. S. Hwang, C. Dussarrat and J. Gatineau, *Chem. Mater.*, 2010, **22**, 5700–5706.

88 K. Gregorczyk, L. Henn-Lecordier, J. Gatineau, C. Dussarrat and G. Rubloff, *Chem. Mater.*, 2011, **23**, 2650–2656.

89 R. Methaapanon, S. M. Geyer, H.-B.-R. Lee and S. F. Bent, *J. Mater. Chem.*, 2012, **22**, 25154.

90 J.-H. Kim, D.-S. Kil, S.-J. Yeom, J.-S. Roh, N.-J. Kwak and J.-W. Kim, *Appl. Phys. Lett.*, 2007, **91**, 052908.

91 W.-D. Kim, B. Kim, J. Chang, Y. Suk Tak, H. Yang, S. Moon, O. Kwon, K. Cho, C.-Y. Yoo and H.-G. Kang, 2012.

92 W. Pan and S. B. Desu, *Phys. status solidi*, 1997, **161**, 201–215.

93 J. Hämäläinen, K. Mizohata, K. Meinander, M. Mattinen, M. Vehkamäki, J. Räisänen, M. Ritala and M. Leskelä, *Angew. Chemie Int. Ed.*, 2018, **57**, 14538–14542.

94 E. Scerri, *Nat. Chem.*, 2010, **2**, 598.

95 R. Kojima, H. Enomoto, M. Muhler and K. Aika, *Appl. Catal. A Gen.*, 2003, **246**, 311–322.

96 S. Vada, A. Hoff, E. Ådnanes, D. Schanke and A. Holmen, *Top. Catal.*, 1995, **2**, 155–162.

97 E. Dumur, B. Delsol, T. Weissl, B. Kung, W. Guichard, C. Hoarau, C. Naud, K. Hasselbach, O. Buisson, K. Ratter and B. Gilles, *IEEE Trans. Appl. Supercond.*, 2016, **26**, 1–4.

98 W. Garrett, A. J. Sherman and J. Stiglich, *Mater. Manuf. Process.*, 2006, **21**, 618–620.

99 R. P. Pezzi, M. Copel, M. Gordon, E. Cartier and I. J. R. Baumvol, *Appl. Phys. Lett.*, 2006, **88**, 243509.

100 A. G. Bagmut, *Funct. Mater.*, 2013, **20**, 180–185.

101 E. Muñoz, R. Schrebler, R. Henríquez, C. Heyser, P. A. Verdugo and R. Marotti, *Thin Solid Films*, 2009, **518**, 138–146.

102 K.-H. Cho, U. Patel, J. Podkaminer, Y. Gao, C. M. Folkman, C. W. Bark, S. Lee, Y. Zhang, X. Q. Pan, R. McDermott and C. B. Eom, *APL Mater.*, 2013, **1**, 042115.

103 P. A. Shcheglov and D. V. Drobot, *Russ. J. Phys. Chem.*, 2006, **80**, 1819–1825.

104 M. Ohkubo, K. Fukai, M. Kohji, N. Iwata and H. Yamamoto, *Supercond. Sci. Technol.*, 2002, **15**, 1778–1780.

105 M. Ghanashyam Krishna and A. K. Bhattacharya, *Solid State Commun.*, 2000, **116**, 637–641.

106 J. O. Zerbino, A. M. Castro Luna, C. F. Zinola, E. Méndez and M. E. Martins, *J. Electroanal. Chem.*, 2002, **521**, 168–174.

107 R. Schrebler, P. Cury, C. Suárez, E. Muñoz, F. Vera, R. Córdova, H. Gómez, J. R. Ramos-Barrado, D. Leinen and E. A. Dalchiele, *Thin Solid Films*, 2005, **483**, 50–59.

108 B. P. Hahn, R. A. May and K. J. Stevenson, *Langmuir*, 2007, **23**, 10837–10845.

109 N. R. Murphy, R. C. Gallagher, L. Sun, J. G. Jones and J. T. Grant, *Opt. Mater. (Amst).*, 2015, **45**, 191–196.

110 K. L. Jiao, L. H. Chang, R. Wallace and W. A. Anderson, *Appl. Supercond.*, 1995, **3**, 55–60.

111 Z. Tan, L. Li, F. Wang, Q. Xu, S. Li, G. Sun, X. Tu, X. Hou, J. Hou and Y. Li, *Adv. Energy Mater.*, 2014, **4**, 1300884.

112 V. Miikkulainen, M. Leskelä, M. Ritala and R. L. Puurunen, *J. Appl. Phys.*, 2013, **113**, 021301.

113 Z. Zhu, P. Sippola, H. Lipsanen, H. Savin and S. Merdes, *Jpn. J. Appl. Phys.*, 2018, **57**, 125502.

114 F. Buja, G. Fiorentino, J. Kokorian and W. M. Van Spengen, *Artic. Nanotechnol.*, 2015, **26**, 255701.

115 T. M. Mayer, J. W. Elam, S. M. George, P. G. Kotula and R. S. Goeke, *Appl. Phys. Lett.*, 2003, **82**, 2883–2885.

116 H. Savin, P. Repo, G. von Gastrow, P. Ortega, E. Calle, M. Garín and R. Alcubilla, *Nat. Nanotechnol.*, 2015, **10**, 624–628.

117 S. Shestaeva, A. Bingel, P. Munzert, L. Ghazaryan, C. Patzig, A. Tünnermann and A. Szeghalmi, *Appl. Opt.*, 2017, **56**, C47.

118 Z. Ren, G. Yuan, J. Zhang, L. Xu, J. Zhang, W. Chen and Y. Hao, *AIP Adv.*, 2018, **8**, 065026.

119 R. Clark, *Materials (Basel).*, 2014, **7**, 2913–2944.

120 H. R. Shea, in *SPIE*, 2009, vol. 7208, p. 72080M.

121 T. K. Minton, B. Wu, J. Zhang, N. F. Lindholm, A. I. Abdulagatov, J. O'Patchen, S. M. George and M. D. Groner, *ACS Appl. Mater. Interfaces*, 2010, **2**, 2515–2520.

122 R. Osiander, M. A. Garrison, D. John and L. Champion, *MEMS and Microstructures in Aerospace Applications Edited by*, 2006.

123 M. Berdova, O. M. E. Ylivaara, V. Rontu, P. T. Törmä, R. L. Puurunen and S.

Franssila, *J. Vac. Sci. Technol. A Vacuum, Surfaces, Film.*, 2015, **33**, 01A106.

124 R. Cooper, H. P. Upadhyaya, T. K. Minton, M. R. Berman, X. Du and S. M. George, *Thin Solid Films*, 2008, **516**, 4036–4039.

125 P. F. Carcia, R. S. McLean, M. D. Groner, A. A. Dameron and S. M. George, *J. Appl. Phys.*, 2009, **106**, 023533.

126 A. A. Dameron, S. D. Davidson, B. B. Burton, P. F. Carcia, R. Scott McLean and S. M. George, *J. Phys. Chem. C*, 2008, **112**, 4573–4580.

127 M. Vähä-Nissi, P. Sundberg, E. Kauppi, T. Hirvikorpi, J. Sievänen, A. Sood, M. Karppinen and A. Harlin, *Thin Solid Films*, 2012, **520**, 6780–6785.

128 A. I. Abdulagatov, Y. Yan, J. R. Cooper, Y. Zhang, Z. M. Gibbs, A. S. Cavanagh, R. G. Yang, Y. C. Lee and S. M. George, *ACS Appl. Mater. Interfaces*, 2011, **3**, 4593–4601.

129 Q. Sun, H. Yu, Y. Liu, J. Li, Y. Lu and J. F. Hunt, *Holzforschung*, 2010, **64**, 757–761.

130 L. H. Kim, K. Kim, S. Park, Y. J. Jeong, H. Kim, D. S. Chung, S. H. Kim and C. E. Park, *ACS Appl. Mater. Interfaces*, 2014, **6**, 6731–6738.

131 S. Pasieczna-Patkowska and J. Ryczkowski, *Ann. UMCS, Chem.*, 2010, **65**, 121–131.

132 G. C. Correa, B. Bao and N. C. Strandwitz, *ACS Appl. Mater. Interfaces*, 2015, **7**, 14816–14821.

133 M. Broas, O. Kanninen, V. Vuorinen, M. Tilli and M. Paulasto-Kröckel, *ACS Omega*, 2017, **2**, 3390–3398.

134 J. Chen, B. Wang, Y. Yang, Y. Shi, G. Xu and P. Cui, *Appl. Opt.*, 2012, **51**, 6839.

135 N. Yamaguchi, K. Tadanaga, A. Matsuda, T. Minami and M. Tatsumisago, *Thin Solid Films*, 2007, **515**, 3914–3917.

136 K. Tadanaga, N. Yamaguchi, Y. Uraoka, A. Matsuda, T. Minami and M. Tatsumisago, *Thin Solid Films*, 2008, **516**, 4526–4529.

137 K. Isakov, Aalto University, 2016.

138 H. Furukawa, K. E. Cordova, M. O'Keeffe and O. M. Yaghi, *Science (80-.).*, 2013,

341, 1230444–1230444.

139 A. Aumüller, P. Erk, G. Klebe, S. Hünig, J. U. von Schütz and H.-P. Werner, *Angew. Chemie Int. Ed. English*, 1986, **25**, 740–741.

140 S. S.-Y. Chui, S. M.-F. Lo, J. P. H. Charmant, A. G. Orpen and I. D. Williams, *Science*, 1999, **283**, 1148–50.

141 M. Kondo, T. Yoshitomi, H. Matsuzaka, S. Kitagawa and K. Seki, *Angew. Chemie Int. Ed. English*, 1997, **36**, 1725–1727.

142 N. Rangnekar, N. Mittal, B. Elyassi, J. Caro and M. Tsapatsis, *Chem. Soc. Rev.*, 2015, **44**, 7128–7154.

143 P. Falcaro, R. Ricco, C. M. Doherty, K. Liang, A. J. Hill and M. J. Styles, *Chem. Soc. Rev.*, 2014, **43**, 5513–5560.

144 F. Vermoortele, R. Ameloot, L. Alaerts, R. Matthessen, B. Carlier, E. V. R. Fernandez, J. Gascon, F. Kapteijn and D. E. De Vos, *J. Mater. Chem.*, 2012, **22**, 10313.

145 Y. Fu, D. Sun, Y. Chen, R. Huang, Z. Ding, X. Fu and Z. Li, *Angew. Chemie Int. Ed.*, 2012, **51**, 3364–3367.

146 N. Kornienko, Y. Zhao, C. S. Kley, C. Zhu, D. Kim, S. Lin, C. J. Chang, O. M. Yaghi and P. Yang, *J. Am. Chem. Soc.*, 2015, **137**, 14129–14135.

147 M. Zhao, K. Yuan, Y. Wang, G. Li, J. Guo, L. Gu, W. Hu, H. Zhao and Z. Tang, *Nature*, 2016, **539**, 76–80.

148 J. Canivet, A. Fateeva, Y. Guo, B. Coasne and D. Farrusseng, *Chem. Soc. Rev.*, 2014, **43**, 5594–5617.

149 D. Feng, K. Wang, Z. Wei, Y.-P. Chen, C. M. Simon, R. K. Arvapally, R. L. Martin, M. Bosch, T.-F. Liu, S. Fordham, D. Yuan, M. A. Omary, M. Haranczyk, B. Smit and H.-C. Zhou, *Nat. Commun.*, 2014, **5**, 5723.

150 H. Jasuja, G. W. Peterson, J. B. Decoste, M. A. Browe and K. S. Walton, *Chem. Eng. Sci.*, 2015, **124**, 118–124.

151 H.-L. Jiang, D. Feng, K. Wang, Z.-Y. Gu, Z. Wei, Y.-P. Chen and H.-C. Zhou, *J. Am.*

Chem. Soc., 2013, **135**, 13934–13938.

152 B. Wang, X.-L. Lv, D. Feng, L.-H. Xie, J. Zhang, M. Li, Y. Xie, J.-R. Li and H.-C. Zhou, *J. Am. Chem. Soc.*, 2016, **138**, 6204–6216.

153 P. Horcajada, C. Serre, G. Maurin, N. A. Ramsahye, F. Balas, M. Vallet-Regí, M. Sebban, F. Taulelle and G. Férey, *J. Am. Chem. Soc.*, 2008, **130**, 6774–6780.

154 S. Roy, V. M. Suresh and T. K. Maji, *Chem. Sci.*, 2016, **7**, 2251–2256.

155 O. M. Yaghi, M. O'Keeffe, N. W. Ockwig, H. K. Chae, M. Eddaoudi and J. Kim, *Nature*, 2003, **423**, 705–714.

156 D. Feng, Z.-Y. Gu, J.-R. Li, H.-L. Jiang, Z. Wei and H.-C. Zhou, *Angew. Chemie Int. Ed.*, 2012, **51**, 10307–10310.

157 I. J. Kang, N. A. Khan, E. Haque and S. H. Jhung, *Chem. - A Eur. J.*, 2011, **17**, 6437–6442.

158 M. W. Logan, J. D. Adamson, D. Le and F. J. Uribe-Romo, *ACS Appl. Mater. Interfaces*, 2017, **9**, 44529–44533.

159 H. Li, M. Eddaoudi, M. O'Keeffe and O. M. Yaghi, *Nature*, 1999, **402**, 276–279.

160 B. Trzaskowski, D. Latek, S. Yuan, U. Ghoshdastider, A. Debinski and S. Filipek, *Curr. Med. Chem.*, 2012, **19**, 1090–109.

161 S. Yuan, L. Feng, K. Wang, J. Pang, M. Bosch, C. Lollar, Y. Sun, J. Qin, X. Yang, P. Zhang, Q. Wang, L. Zou, Y. Zhang, L. Zhang, Y. Fang, J. Li and H.-C. Zhou, *Adv. Mater.*, 2018, **30**, 1704303.

162 R.-B. Lin, S. Xiang, B. Li, Y. Cui, G. Qian, W. Zhou and B. Chen, *Coord. Chem. Rev.*, 2019, **384**, 21–36.

163 A. Bétard and R. A. Fischer, *Chem. Rev.*, 2012, **112**, 1055–1083.

164 T. Haraguchi, K. Otsubo, O. Sakata, A. Fujiwara and H. Kitagawa, *Inorg. Chem.*, 2015, **54**, 11593–11595.

165 B. Gilbert, F. Huang, H. Zhang, G. A. Waychunas and J. F. Banfield, *Science (80-.).*, 2004, **305**, 651–654.

166 S. Sakaida, K. Otsubo, O. Sakata, C. Song, A. Fujiwara, M. Takata and H. Kitagawa, *Nat. Chem.*, 2016, **8**, 377–383.

167 M. Meilikhov, S. Furukawa, K. Hirai, R. A. Fischer and S. Kitagawa, *Angew. Chemie Int. Ed.*, 2013, **52**, 341–345.

168 O. Shekhah, H. Wang, M. Paradinas, C. Ocal, B. Schüpbach, A. Terfort, D. Zacher, R. A. Fischer and C. Wöll, *Nat. Mater.*, 2009, **8**, 481–484.

169 T. Haraguchi, K. Otsubo and H. Kitagawa, *Eur. J. Inorg. Chem.*, 2018, **2018**, 1697–1706.

170 H. Bux, F. Liang, Y. Li, J. Cravillon, M. Wiebcke and J. Caro, *J. Am. Chem. Soc.*, 2009, **131**, 16000–16001.

171 S. R. Venna and M. A. Carreon, *J. Am. Chem. Soc.*, 2010, **132**, 76–78.

172 G. Lu and J. T. Hupp, *J. Am. Chem. Soc.*, 2010, **132**, 7832–7833.

173 A. Demessence, C. Boissière, D. Grosso, P. Horcajada, C. Serre, G. Férey, G. J. A. A. Soler-Illia and C. Sanchez, *J. Mater. Chem.*, 2010, **20**, 7676.

174 M. Usman, S. Mendiratta and K.-L. Lu, *ChemElectroChem*, 2015, **2**, 786–788.

175 S. S. Y. Chui, S. M. F. Lo, J. P. H. Charmant, A. G. Orpen, I. D. Williams, P. Haney, R. A. Kinney, V. Szalai, F. El Gabaly, H. P. Yoon, F. Léonard and M. D. Allendorf, *Science*, 1999, **283**, 1148–50.

176 S. Hermes, F. Schröder, R. Chelmowski, C. Wöll and R. A. Fischer, *J. Am. Chem. Soc.*, 2005, **127**, 13744–13745.

177 I. Stassen, N. Campagnol, J. Fransaer, P. Vereecken, D. De Vos and R. Ameloot, *CrystEngComm*, 2013, **15**, 9308.

178 K. Khaletskaya, S. Turner, M. Tu, S. Wannapaiboon, A. Schneemann, R. Meyer, A. Ludwig, G. Van Tendeloo and R. A. Fischer, *Adv. Funct. Mater.*, 2014, **24**, 4804–4811.

179 P. C. Lemaire, J. Zhao, P. S. Williams, H. J. Walls, S. D. Shepherd, M. D. Losego, G. W. Peterson and G. N. Parsons, *ACS Appl. Mater. Interfaces*, 2016, **8**, 9514–9522.

180 J. Zhao, W. T. Nunn, P. C. Lemaire, Y. Lin, M. D. Dickey, C. J. Oldham, H. J. Walls, G. W. Peterson, M. D. Losego and G. N. Parsons, *J. Am. Chem. Soc*, 2015, **137**, 13756−13759.

181 R. Ameloot, L. Pandey, M. Van der Auweraer, L. Alaerts, B. F. Sels and D. E. De Vos, *Chem. Commun.*, 2010, **46**, 3735.

182 K. Yusenko, M. Meilikhov, D. Zacher, F. Wieland, C. Sternemann, X. Stammer, T. Ladnorg, C. Wöll and R. A. Fischer, *CrystEngComm*, 2010, **12**, 2086.

183 V. Varela-Guerrero, Y. Yoo, M. C. McCarthy and H.-K. Jeong, *J. Mater. Chem.*, 2010, **20**, 3938.

184 X. Zou, G. Zhu, F. Zhang, M. Guo and S. Qiu, *CrystEngComm*, 2010, **12**, 352–354.

185 A. Ghorbanpour, L. D. Huelsenbeck, D.-M. Smilgies and G. Giri, *CrystEngComm*, 2018, **20**, 294–300.

186 O. M. Yaghi, G. Li and H. Li, *Chem. Mater.*, 1997, **9**, 1074–1076.

187 S. Hausdorf, J. Wagler, R. Moβig and F. O. R. L. Mertens, *J. Phys. Chem. A*, 2008, **112**, 7567–7576.

188 A. Pichon, A. Lazuen-Garay and S. L. James, *CrystEngComm*, 2006, **8**, 211.

189 T. Friščić and L. Fábián, *CrystEngComm*, 2009, **11**, 743.

190 T. Friščić, *J. Mater. Chem.*, 2010, **20**, 7599.

191 K. S. Park, Z. Ni, A. P. Côté, J. Y. Choi, R. Huang, F. J. Uribe-Romo, H. K. Chae, M. O'Keeffe and O. M. Yaghi, *Proc. Natl. Acad. Sci. U. S. A.*, 2006, **103**, 10186–10191.

192 F. Monforte, G. Mannino, A. Alberti, E. Smecca, M. Italia, A. Motta, C. Tudisco and G. G. Condorelli, *Appl. Surf. Sci.*, 2019, **473**, 182–189.

193 H. Bux, A. Feldhoff, J. Cravillon, M. Wiebcke, Y.-S. Li and J. Caro, *Chem. Mater.*, 2011, **23**, 2262–2269.

194 M. C. McCarthy, V. Varela-Guerrero, G. V. Barnett and H.-K. Jeong, *Langmuir*, 2010, **26**, 14636–14641.

195 H. Bux, C. Chmelik, R. Krishna and J. Caro, *J. Memb. Sci.*, 2011, **369**, 284–289.

196 J. Yao, D. Dong, D. Li, L. He, G. Xu and H. Wang, *Chem. Commun.*, 2011, **47**, 2559.

197 M. Drobek, M. Bechelany, C. Vallicari, A. Abou Chaaya, C. Charmette, C. Salvador-Levehang, P. Miele and A. Julbe, *J. Memb. Sci.*, 2015, **475**, 39–46.

198 Q. Wu, X. Meng, X. Gao and F.-S. Xiao, *Acc. Chem. Res.*, 2018, **51**, 1396–1403.

199 A. Dhakshinamoorthy, A. Santiago-Portillo, A. M. Asiri and H. Garcia, *ChemCatChem*, 2019, **11**, 899–923.

200 C. L. Hobday, R. J. Marshall, C. F. Murphie, J. Sotelo, T. Richards, D. R. Allan, T. Düren, F.-X. Coudert, R. S. Forgan, C. A. Morrison, S. A. Moggach and T. D. Bennett, *Angew. Chemie Int. Ed.*, 2016, **55**, 2401–2405.

201 J. B. DeCoste, G. W. Peterson, H. Jasuja, T. G. Glover, Y. Huang and K. S. Walton, *J. Mater. Chem. A*, 2013, **1**, 5642.

202 K. M. L. Taylor-Pashow, J. Della Rocca, Z. Xie, S. Tran and W. Lin, *J. Am. Chem. Soc.*, 2009, **131**, 14261–14263.

203 F. Vermoortele, B. Bueken, G. Le Bars, B. Van de Voorde, M. Vandichel, K. Houthoofd, A. Vimont, M. Daturi, M. Waroquier, V. Van Speybroeck, C. Kirschhock and D. E. De Vos, *J. Am. Chem. Soc.*, 2013, **135**, 11465–11468.

204 H. Wu, Y. Shen Chua, V. Krungleviciute, M. Tyagi, P. Chen, T. Yildirim and W. Zhou, *J. Am. Chem. Soc.*, 2013, **135**, 10525−10532.

205 S. J. D. Smith, B. P. Ladewig, A. J. Hill, C. H. Lau and M. R. Hill, *Sci. Rep.*, 2015, **5**, 7823.

206 I. Hod, W. Bury, D. M. Karlin, P. Deria, C.-W. Kung, M. J. Katz, M. So, B. Klahr, D. Jin, Y.-W. Chung, T. W. Odom, O. K. Farha and J. T. Hupp, *Adv. Mater.*, 2014, **26**, 6295–6300.

207 H. Fei, S. Pullen, A. Wagner, S. Ott and S. M. Cohen, *Chem. Commun.*, 2015, **51**, 66–69.

208 I. Stassen, M. Styles, T. Van Assche, N. Campagnol, J. Fransaer, J. Denayer, J.-C. Tan,

P. Falcaro, D. De Vos and R. Ameloot, *Chem. Mater.*, 2015, **27**, 1801–1807.

209 C. Zhang, Y. Zhao, Y. Li, X. Zhang, L. Chi and G. Lu, *Chem. - An Asian J.*, 2016, **11**, 207–210.

210 M. Nazari, M. Rubio-Martinez, R. Babarao, A. A. Younis, S. F. Collins, M. R. Hill and M. C. Duke, *J. Phys. D. Appl. Phys.*, 2018, **51**, 025601.

211 E. Virmani, J. M. Rotter, A. Mähringer, T. von Zons, A. Godt, T. Bein, S. Wuttke and D. D. Medina, *J. Am. Chem. Soc.*, 2018, **140**, 4812–4819.

212 Y. Huang, C. Tao, R. Chen, L. Sheng, J. Wang, Y. Huang, C. Tao, R. Chen, L. Sheng and J. Wang, *Nanomaterials*, 2018, **8**, 676.

213 A. L. Semrau, S. Wannapaiboon, S. P. Pujari, P. Vervoorts, B. Albada, H. Zuilhof and R. A. Fischer, *Cite This Cryst. Growth Des*, 2019, **19**, 1738–1747.

214 L. Lutterotti, D. Chateigner, S. Ferrari and J. Ricote, in *Thin Solid Films*, Elsevier, 2004, vol. 450, pp. 34–41.

215 S. Seppälä, University of Helsinki, 2019.

216 K. Leus, T. Bogaerts, J. De Decker, H. Depauw, K. Hendrickx, H. Vrielinck, V. Van Speybroeck and P. Van Der Voort, *Microporous Mesoporous Mater.*, 2016, **226**, 110–116.

217 G. Vazquez, E. Alvarez and J. M. Navaza, *J. Chem. Eng. Data*, 1995, **40**, 611–614.